



SAPIENZA
UNIVERSITÀ DI ROMA

DOCTORATE COURSE IN
Mathematical Models for Engineering, Electromagnetics and Nanosciences

INNOVATIVE ELECTROCATALYSTS AND NANOCOMPOSITE MEMBRANES
FOR LOW TEMPERATURE PROTON EXCHANGE MEMBRANE FUEL CELLS

Cycle XXXII: Curriculum Materials Science

PhD Candidate: Lucia Mazzapioda

Tutor: Prof. Maria Assunta Navarra

CONTENTS

PURPOSE AND AIM OF THE THESIS	4
1. INTRODUCTION	
1.1 Introduction to Fuel Cells	5
1.2 Basic Principles and Characteristics of Fuel Cells (PEMFCs)	6
1.3 Nafion as Proton Conducting Membranes	9
1.4 Electrocatalyst and Electrode	12
1.4.1 Oxygen Reduction Reaction (ORR)	14
Reference	16
2. NON-STOICHIOMETRIC CALCIUM TITANATE PEROVSKITES SYNTHESIS AND CHARACTERIZATIONS	
2.1 Introduction	18
2.2 Synthesis of Non-stoichiometric Calcium Titanate Perovskites: $\text{CaTiO}_{3-\delta}$ and $\text{CaTi}_{0.8}\text{Fe}_{0.2}\text{O}_{3-\delta}$	21
2.2.1 Physical-Chemical Characterizations	22
2.3 Results and Discussion: Calcium Titanate Perovskite $\text{CaTiO}_{3-\delta}$	23
2.4 Results and Discussion: Iron-doped Calcium Titanate Perovskite $\text{CaTi}_{0.8}\text{Fe}_{0.2}\text{O}_{3-\delta}$	28
2.5 Conclusions	30
Reference	32
3. CALCIUM TITANATE PEROVSKITES USED AS ADDITIVE OF Pt/C CATALYST FOR OXYGEN REDUCTION REACTION IN ACIDIC MEDIA	
3.1 Introduction to Rotating Disk Electrode (RDE)	33
3.2 Catalytic Layer Preparation	35
3.2.1 Electrochemical Investigations	35
3.3 Results and Discussion: Calcium Titanate Perovskite $\text{CaTiO}_{3-\delta}$	36
3.5 Results and Discussion: Iron-doped Calcium Titanate Perovskite $\text{CaTi}_{0.8}\text{Fe}_{0.2}\text{O}_{3-\delta}$	43
3.4 Direct Methanol Fuel Cell Performances	45
3.4.1 Results and Discussion	46
3.6 Conclusions	48
Reference	49
4. CALCIUM TITANATE $\text{CaTiO}_{3-\delta}$ PEROVSKITE USED AS ADDITIVE FOR NAFION MEMBRANES	
4.1 Introduction	50
4.2 Membrane Synthesis	51
4.2.1 Physical-Chemical Characterizations	51
4.3 Results and Discussion	55
4.4 Direct Methanol Fuel Cell Tests	70
4.4.1 Methanol Crossover Measurements	70
4.4.2 Direct Methanol Fuel Cell Performances	73
4.5 Conclusions	75
Reference	76
General Conclusions	78

PURPOSE AND AIM OF THE THESIS

For sustainable economic growth and environment protection, energies generated from renewable sources result indispensable. In this field, fuel cell technologies are considered as a key element in the future clean energy becoming a promising solution.

Low Temperature Polymer Exchange Membrane Fuel Cells (PEMFCs), including Direct Methanol Fuel Cells (DMFCs), offer several advantages as compared to others systems in term of low emission of pollutants, high energy conversion and efficiency. However, these devices present two major drawbacks, high cost and low durability that must to be solved for a their large scale application and commercialization.

Indeed, the Nafion membranes and Pt/C catalysts adopted respectively as electrolyte and electrode component in these devices, are two areas where the technology have issues of cost, durability and efficiency. This means that new materials are necessary.

The aim of this PhD work has been the development of advanced materials to be used as both electrocatalysts and electrolyte additives in order to reduce cost, improve the performance and durability of low temperature fuel cells.

In particular our interest was focused on non-stoichiometric Calcium Titanate Perovskites, i.e. $\text{CaTiO}_{3-\delta}$ (CTO) and $\text{CaTi}_{0.8}\text{Fe}_{0.2}\text{O}_{3-\delta}$ (CTFO), both used as co-catalyst for the oxygen reduction reaction (ORR) which is the main rate-decreasing step in low-temperature fuel cell devices. The aim was to improve the stability and durability of Pt catalysts and support Pt catalytic activity in order to reduce its loading.

The $\text{CaTiO}_{3-\delta}$ perovskite was also used as additive in Nafion membrane in order to enhance the water retention, the mechanical properties of the membrane and reduce the gas/methanol crossover.

Synthesis routes, electrochemical and powerful physical-chemical analysis of these materials were carried out, here reported and discussed.

CHAPTER I

INTRODUCTION

1.1 INTRODUCTION TO FUEL CELLS

Fuel cells are electrochemical devices that convert the chemical energy of a reaction directly into electrical energy. The physical basic of a fuel cell is akin to a battery; both produce electrical energy combining a negative electrode (anode) with a positive electrode (cathode) in contact with an electrolyte. However, a battery is a closed system that work exhausting its active electrode components demanding a charge process to reactivate the initial materials. A fuel cell system uses a flow of reagents supplied from an external storage tank guaranting a continuos process.

In a typical fuel cell, gaseous fuels are fed to the anode compartment and an oxidant (i.e., oxygen from air) is fed to the cathode compartment; the electrochemical reactions take place at the electrodes to produce the electric current.

A variety of fuel cells are in different stages of development. They can be classified by the combination of type of fuel and oxidant, the type of electrolyte, the temperature of operation, etc.

The most common classification of fuel cells is by the type of electrolyte used in the cells and includes:

- 1) proton exchange membrane (polymer) electrolyte fuel cell (PEMFC)
- 2) alkaline fuel cell (AFC)
- 3) phosphoric acid fuel cell (PAFC)
- 4) molten carbonate fuel cell (MCFC), and 5) solid oxide fuel cell (SOFC)

These fuel cells are listed in the order of approximate operating temperature, ranging from ~80°C for PEMFC, ~100°C for AFC, ~200°C for PAFC, ~650°C for MCFC, and 800°C to 1000°C for SOFC^[1,2].

Among all these fuel cells above mentioned, low temperature fuel cells (PEMFCs) offer several advantages such as high power density delivered, low weight and volume, high energy conversion and efficiency and a convenient range of operating temperatures.

It is interesting to know that this type of fuel cells were first deployed in the Gemini space program in the 1960, using liquid oxygen and liquid hydrogen to generate electricity, with water as a byproduct. The Gemini innovative program carried the use of fuel cells in space, and this technology was subsequently used in the Apollo missions when USA landed on the moon in 1969^[3].

Today, the PEMFCs are the best candidates for cars, for buildings and smaller applications. Several automotive company, as General Motors, Toyota, Honda and Hyundai have started to commercialize fuel cell vehicles from 2015.

However, all of these applications require unique operating conditions and specific materials to improve.

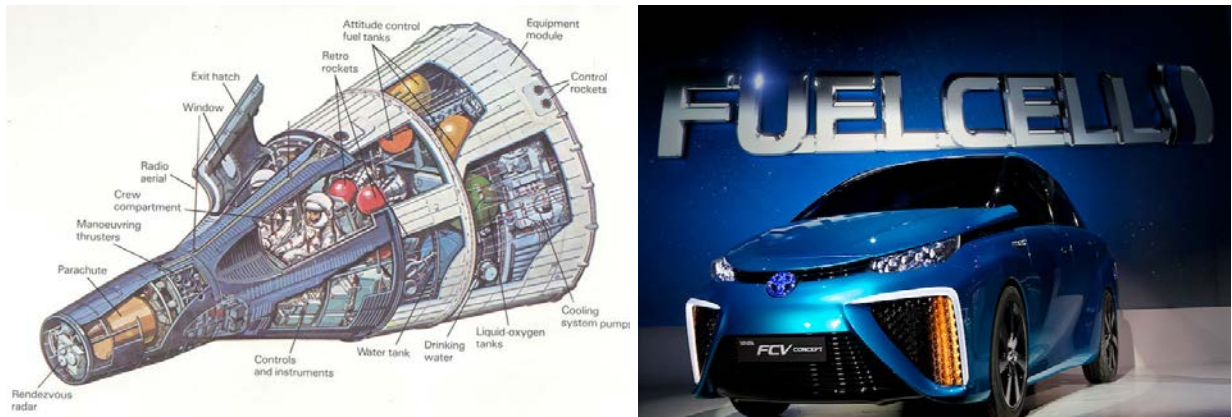


Figure 1: Gemini 5 fuel cell (on the left) and a Fuel Cell Miray Toyota (on the right)

1.2 BASIC PRINCIPLES AND CHARACTERISTICS OF FUEL CELLS (PEMFCs)

A schematic representation of a H₂/O₂ PEM fuel cell with the reactant gases, products and the ion conduction flow directions through the cell, is shown in Figure 2.

The core of a fuel cell is a proton exchange membrane, the electrode, anode and cathode, are in intimate contact with the membrane faces.

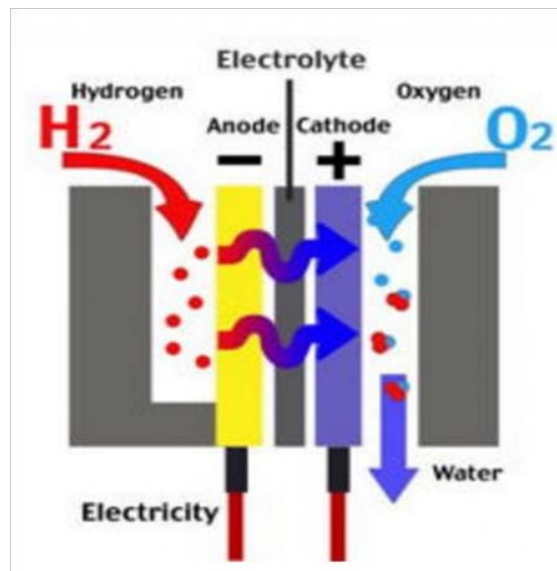
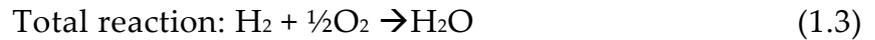
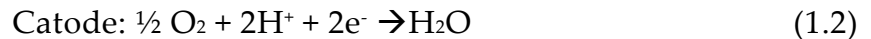


Figure 2: Representation of a Fuel Cell H₂/O₂^[4]

The cell reactions are:



The overall process of a fuel cell corresponds to a theoretical cell potential of 1,23 V at standard conditions ($T=25^\circ\text{C}$ and $P=1\text{bar}$)^[5].

The reactants, hydrogen and oxygen (or air), flow through the flowfield channels and they diffuse through the gas diffusion layer into the catalytic layers, where electrochemical reactions take place. Hydrogen is oxidized at the anode producing protons and electrons. Protons pass through the membrane while the electrons, coming toward the external circuit, produce electrical current. At the cathode, oxygen is reduced and recombined with protons and electrons to form water, which is the only product of the reaction thus, corrosion problems are minimal.

Additionally, the membrane provides also as a physical barrier to prevent a direct mix of the fuel and oxidant gas.

One of the attraction of this device is the high chemical energy conversion efficiency into electrical energy^[6].

Contrary to a common combustion engine which is limited by the thermodynamic of Carnot cycle obtaining efficiency values ranging from 40-48%, the theoretical electrical efficiency of a fuel cell, ξ , is given by the ratio of the change Gibbs free energy to the change enthalpy

$$\xi_{\text{teofuelcell}} = \Delta G / \Delta H = 1 - T\Delta S / \Delta H \quad (1.4)$$

For a fuel cell at low temperature the efficiency is approximately 83%.

However, this efficiency value for all fuel cells is not obtained because of irreversible voltage losses associated with the flow of current. Consequently, the practical electrochemical efficiency ξ , can be defined as the real electrical energy achieved, divided by the Gibbs free energy

$$\xi = -2FE / \Delta G \quad (1.5)$$

where E is the real voltage of the fuel cell which can be written as follow

$$E = E_{eq} - \eta_{tc} - \eta_{ohm} - \eta_{diff} \quad (1.6)$$

with E_{eq} is the reversible voltage, η_{tc} is the loss in voltage due to kinetic activation resistance, η_{ohm} is the loss in voltage due to ohmic resistance and η_{diff} is the loss in voltage due to transport resistance.

Deviations from the theoretical potential give a measure of fuel cell efficiency.

In particular, sluggish reaction kinetics give rise to activation overpotential at both electrodes that can be expressed by the following equation

$$\eta_{act} \sim (RT/\alpha nF) \ln (I/I_0) \quad (1.7)$$

where F/RT are respectively the Faraday (F) and gas (R) constants, T is temperature (K), α is the transfer coefficient that describes the fraction of overpotential abating the reaction, I is the current density, and I_0 , is the reaction exchange current density or rather is the anodic or cathodic current of the cell under equilibrium conditions.

This equation (1.7) derive from the more general Butler-Volmer equation^[7]

$$I=I_0\{ \exp [\alpha nF\eta / RT] - \exp [(1-\alpha)nF\eta / RT]\} \quad (1.8)$$

which account for reaction rate in both directions.

The activation losses can also be expressed simply as the Tafel equation:

$$\eta_{act} = b \log(I/I_0) \quad (1.9)$$

with b defined as Tafel slope for which the slow reaction kinetics of low temperature FCs cause an offset in the open circuit potential, E_0 , by an amount

$$E_0-E \sim b \log i_0 \quad (1.10)$$

Considering both electrode reactions, the cathode reaction (oxygen reduction reaction) is the main rate-decreasing step of the all low temperature fuel cells, becoming the major contributor to activation polarization.

The ohmic overpotential of a cell is given by

$$\eta_{ohm}=i^*R \quad (1.11)$$

where i is the current flowing through the cell and R is the total cell resistance, which includes the resistance to the flow of ions in the electrolyte and resistance to flow of electrons through the electrode materials.

A way to reduce the ohmic losses is by enhancing the ionic conductivity of the electrolyte and by reducing the electrode separation.

The last overpotential term is related to the mass diffusion η_{diff} of reactants at the electrode

$$\eta_{diff} = RT/nF \ln(1- i/i_l) \quad (1.12)$$

where i_l , the limiting current is a measure of the maximum rate at which a reactant can be supplied to an electrode.

When reagents are consumed by electrochemical reactions, a concentration gradient is formed causing a loss of potential. Several processes may contribute to concentration polarization such as slow diffusion of reagents in the gas phase in the electrode pores, solution/dissolution of reactants/products into/out of the electrolyte,

or diffusion of reactants/products through the electrolyte to/from the electrochemical reaction site.

In figure 3, all sources of a voltage loss are reported in a typical polarization curve for a H₂/O₂ PEM^[8].

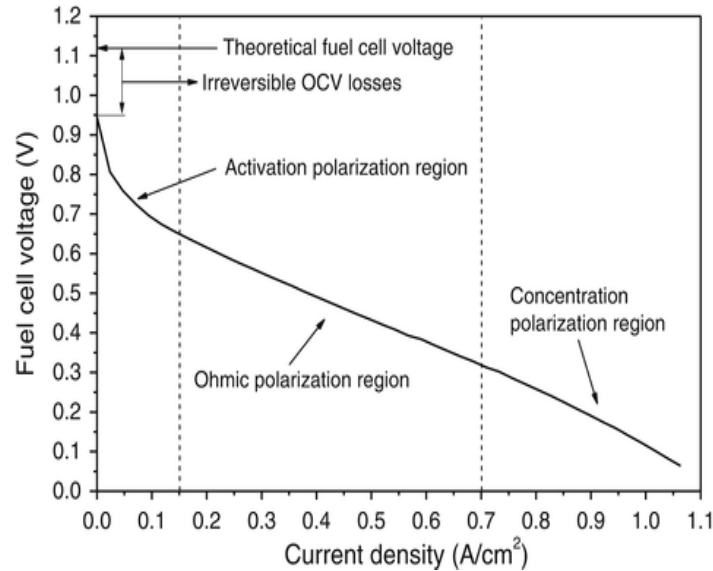


Figure 3: Example of a fuel cell polarization curve

As shown in figure 2 it is evident that high efficiencies of a fuel cell are obtained if all these following aspects are respected. The gases diffusion and electrons transport through the electrolyte is slow, the conductivity of each component, in particular the electrolyte, is high and the kinetic of reaction at the electrodes is fast. Nevertheless a facile mass diffusion of reagents through both porous electrode is required.

1.3 NAFION AS PROTON CONDUCTING MEMBRANE

Perfluorosulfonic acid polymers are the state-of-the-art of solid electrolytes used in low temperature proton exchange membrane fuel cells (PEMFCs)^[9].

The most used is the Nafion, manufactured by DuPont, thank to its main features such as high proton conductivity under fully hydrated conditions, suitable mechanical properties, high chemical and electrochemical stability, low fuel permeability and electronic insulation^[10].

The chemical structure of Nafion is shown in Figure 4; it can be divided into two phase: hydrophobic and hydrophilic regions. The hydrophobic region is a continuous semi-crystalline region Teflon®-like, being made up of main chain TFE segments.

The hydrophilic regions consist of sulfonate groups responsible for the Nafion ionic conductivity.

In general the proton conductivity of these membranes with H₂O:SO₃ ~15:1, is approximately ~10⁻¹ Ω⁻¹cm⁻¹ at room temperature and under fully hydrated conditions.

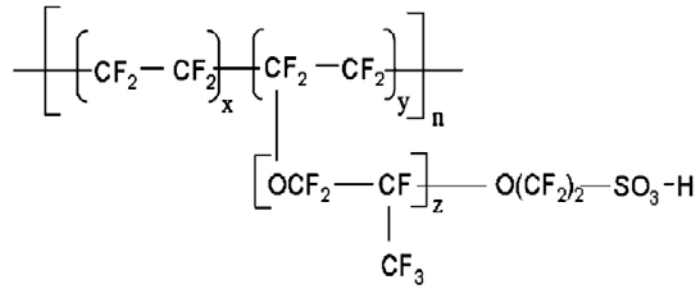


Figure 4: Chemical structure of Nafion membrane

The first model, the Geirke model, well-known as the cluster-network model, is used to explain the Nafion behavior under hydrated state. It assumes that the ion exchange sites, sulfonate groups, give rise to spherical clusters similar looking to micelles, arranged on a regular lattice and interconnected with narrow channels^[11,12].

A schematic representation of this model is shown in Figure 5.

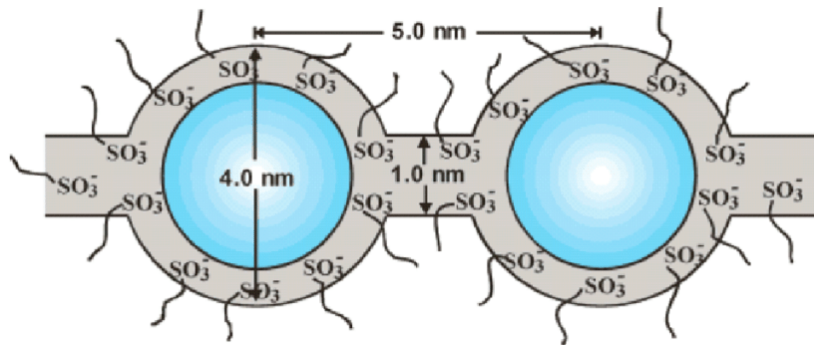


Figure 5: Cluster-network model for the morphology of hydrated Nafion^[11]

This ionic clustering doesn't only affect the mechanical properties of the polymer but also have a direct effect on the transport properties across the membrane. Indeed, the increase of ionic cluster size with hydration level allows the ionic conductivity of Nafion membranes through a "hop-turn" mechanism, first suggested by Grothuss, and often referred to as the Grothuss mechanism.

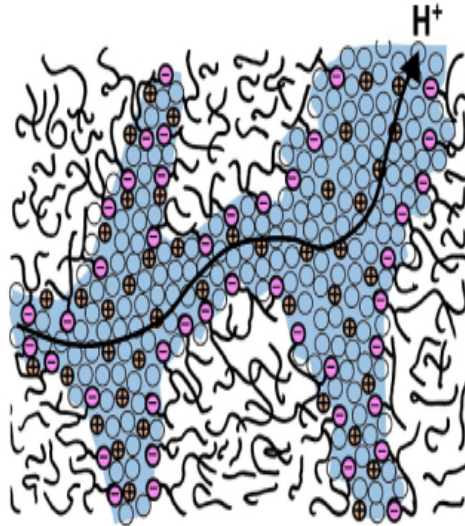


Figure 6: Proton translocation through a chain of water molecules by the Grotthus mechanism adapted from Kreuer^[16]

This means that an adequately humidification of the Nafion membrane is necessary to obtain a good ionic conductivity of the electrolyte.

However, in an operation fuel cell, the presence of an excess of water can prevent reactant diffusion to the catalyst sites at electrode sides increasing the total cell resistance.

The electrodes, in this case, are considered to be "flooded" and the performance of the cell drops drastically. Furthermore, increasing water content leads to increase the swelling of the polymer making it water soluble.

Because of problems with water management imposed by the polymer, a PEM fuel cell is forced to operate at temperature less than 120°C.

Several approaches have been considered for reducing the problems associated with water management based on the synthesis of alternative membranes that are stable and high proton-conductive at higher temperatures.

Many promising polymers based on aromatic thermoplastics such as poly(aryl ether ketone)s (PAEKs) (e.g. PEEK), poly(ether sulfone) (PES), polybenzimidazole (PBI) and related materials, are studied as replacement of Nafion membranes thanks to their features such as high chemical and thermo-oxidative stability, good mechanical properties and low cost^[13].

The conductivity of sulfonated hydrocarbons was improved, by sulfonation of polymers which can be carried out by either directly introducing the sulfonic acid group on the polymer back-bone or by polymerizing sulfonated monomers^[14].

Among all these polymers, the sulfonated SPEEK membranes have shown a good performance as an electrolyte for medium temperature fuel cells.^[15] Furthermore, as reported by Kreuer^[16], the absorptive amount of methanol in these membranes is lower with respect to Nafion membranes, suggesting that they could reduce the problems associated with water and methanol crossover in direct methanol fuel cells (DMFCs).

In addition to this strategy another approach has been to develop composite polymer electrolyte membranes by the incorporation of functional additives able to improve the low RH and high temperature performances of PEMFCs^[17,18].

These additives may be metal oxide nanoparticles, such as SiO₂, TiO₂, ZrO₂ or functionalized inorganic materials, such as sulfated metal oxides. The family of sulfated metal oxide (S-MO₂) is very attractive, thanks to the intrinsic super-acidity properties. It has been widely investigated by us to form nano-composite membranes with good performances at the targeted conditions described above^[19-23].

The presence of acidic hygroscopic additives ensures better hydration and proton conductivity of the membranes also decrease the cross-over of the gases during fuel cell operations demonstrating the applicability in PEMFCs.

1.4 ELECTROCATALYST AND ELECTRODE

PEMFCs electrodes consist of gas-diffusion electrodes (GDE) made up of a multi-layers structure, containing carbon materials which are the conductive support onto the catalytic layer is deposited. Gas diffusion layer (GDL), a GDE component, consists of a thin layer of carbon black mixed with an organic binder, frequently polytetrafluoroethylene (PTFE) used to maintain the structural integrity to the layer and to support the gas transport. GDL allows the diffusion of fuel and oxidant to the anode and the cathode catalyst surfaces, respectively.

In order to encourage the improvement of fuel cells performance, porous electrodes with high surface area are required. Indeed an ideal electrode have to allow the access of reactant gases (or liquid) to the active zones where the noble metal catalysts are in contact with the ionic and electronic conductors. Consequently three different components, gas/ electrolyte/ electrode surface, must to meet at the same point, the so-called tri-phase boundaries, where the redox reactions take place.

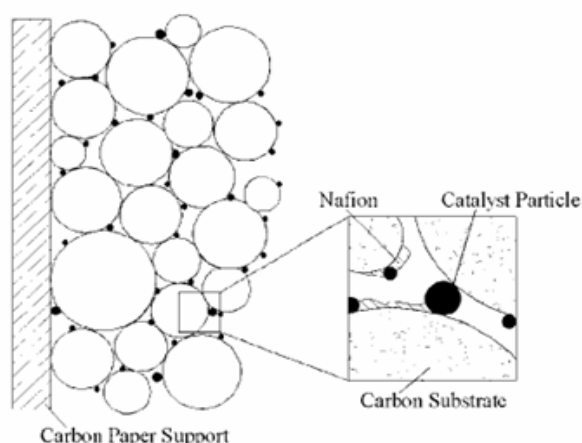


Figure 7: A scheme of the three-phase boundary in a GDE consisting of the ionomer (ionic conductivity), the pores in the catalyst (gas diffusion), and the catalyst particles (support for electronic conductivity)^[24]

The nature of this interface plays a crucial role in the electrochemical performance of fuel cell devices in term of higher current densities supplied, which are obtained when a stable three-phase interface is established and the electrolyte layer, on the electrode surface, is sufficiently thin to guarantee transport of reactants to the electroactive sites.

A typical Membrane Electrode Assembly (MEA) is an assembled stack of a polymer electrolyte, two catalyst layers, and two GDL used in fuel cells. A schematic diagram of a polymeric MEA is shown in figure 8^[25].

Additional components in a complete fuel cell system are the bipolar plates. They conduct electrical current from cell to cell, remove heat from the active area and uniformly distribute fuel and air keeping them separate from one another. These materials must to have high electronic conductivity, impermeability and chemical stability.

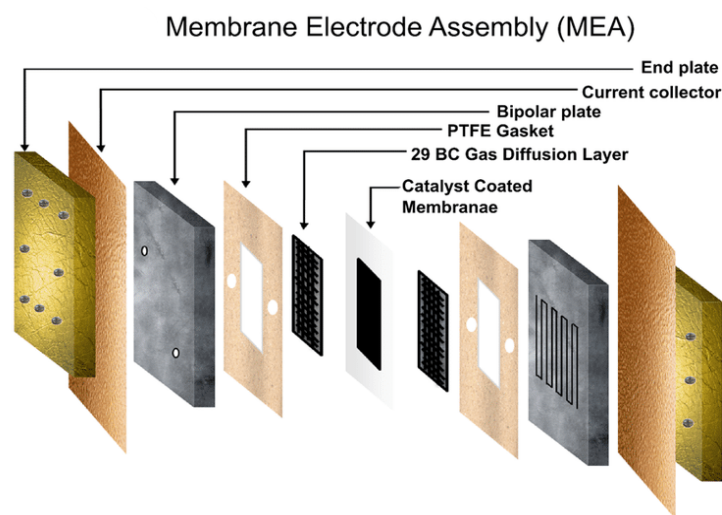


Figure 8: A scheme of a Membrane Electrode Assembly (MEA)^[25]

In a low-temperature fuel cell, Platinum (Pt) is one of the most commonly catalysts used for both electrochemical reactions (oxidation/reduction).

Up to now, higher catalysts loading is required to reach a good efficiency^[26] even though the Pt content in hydrogen/air fuel cell has been reduced from 4 mgcm⁻² per electrode to less than 0.5 mgcm⁻².

In the last several decades, great progress has been made in the research and development of new alternative catalysts in order to reduce or replace expensive Pt.

In this effort two principle strategies have been explored^[27,28]:

- 1) increase Pt catalytic activity and durability reducing Pt content
- 2) improve Pt utilization by dispersing Pt nanoparticles on a high-surface carbon support.

The first approach can be obtained through alloying Pt particles with other transition metals such as Ni, Fe, Co, etc. These catalysts show a strong activity towards the oxygen reduction reaction (ORR). However, there are many issues about the long-term stability of these Pt-alloy catalysts due to the leaching of the non-noble metals in the fuel cell operating environment. This effect can cause catalytic activity loss, degradation of electrolyte by metal ionic contamination and increase of catalyst layer resistance at the cathode side.

The second approach obtained by increasing the surface area and dispersion of Pt nanoparticles using high carbon support, can effectively reduce Pt loading. However, reduce Pt particle size under 2-3 nm and further increasing the surface area seems to be impossible. Furthermore, the agglomeration of Pt nanoparticles became the major problem during fuel cell test^[29,30].

Other precious metals such as Pd, Ir, and Ru, can be used as fuel cell catalysts because of their catalytic activity towards the ORR. Unfortunately, their price rises dramatically in the last several years becoming not suitable solutions either.

Recently, non-noble catalyst are very attractive because of their high natural abundance and low cost as alternative electrocatalysts to platinum.

For example, perovskite-type and spinel-type oxides have been explored and studied because of their promising catalytic activities towards the oxygen reduction and hydrogen oxidation reactions. However, most of these catalysts have demonstrated activity and stability in alkaline solutions. In a PEM fuel cell, where strong acidic electrolytes are used, these catalysts are not favorable.

Currently, transition metal macrocycles seem to be one of most promising non-noble electrocatalysts in acid electrolytes showing an activity close to Pt-based catalysts for the ORR. The major their drawback is the poor stability when they are employed as PEM fuel cell catalysts^[31].

However, non-noble catalysts should be the future catalysts for sustainable fuel cell commercialization.

1.4.1 OXYGEN REDUCTION REACTIONS (ORR)

In proton exchange membrane (PEM) fuel cells, including direct methanol fuel cells (DMFCs), oxygen reduction reaction (ORR) is the reaction occurring at the cathode side.

One of the challenges to overcome, for a large-scale mass production of these type of fuel cells, concerns the development of highly stable reversible electrodes capable to catalyze efficiently the oxygen reduction reaction. Unfortunately, this reaction is kinetically sluggish toward electrons transfer reaction because it is thermodynamically unfavorable, resulting in high overpotentials at the fuel cell cathode.

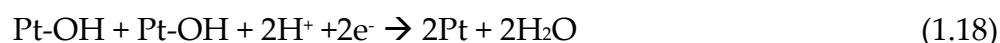
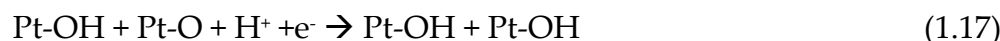
Consequently, high loading of the costly noble metal electrocatalyst is required. Up to now, Pt-based catalysts are widely recognized as the benchmark electrocatalysts for the ORR in low temperature fuel cells, due to their intrinsic activity and stability in acidic solutions, owing to its lowest onset potentials for driving the reactions.

The oxygen reduction reaction in acidic solutions requires the transfer of four electrons to complete the reaction:



The simultaneous transfer of these electrons, the so-called the direct 4-electron reduction pathway, is highly inhibited. In fact, a partial electron transfer takes place leading to the 2-electron reduction pathway where H_2O_2 is further reduced to H_2O or can be decomposed chemically. The use of a Pt electrocatalyst causes a formation of intermediates reaction, with consequent reduction of the reaction rate.

The 4-electron theorized mechanism is the following:



due to (i) shortening of Pt–Pt interatomic distance which is favorable for the dissociative adsorption of O_2 , (ii) increased d-band vacancies that produce a strong metal– O_2 interaction then weakening the O–O bond and (iii) surface roughening^[32].

As visible above, ORR is a complex reaction that includes a number of electrochemical and/or chemical steps with various intermediates. The main limitations of all process is due to slow kinetics owing to the formation of $\text{OH}_{(\text{ads})}$ species.

To obtain the 4-electron pathway ORR on Pt catalysts at low overpotentials, a small ratio of OH to H_2O adsorption bond strengths and/or a higher activation energy for $\text{OH}_{(\text{ads})}$ compared to O_2 chemisorption is required^[33].

For practical applications of a fuel cell, the direct path is desirable because the formation of peroxides reduces the cell performances by limiting the cell potential and lead to internal corrosion phenomena.

REFERENCES

- [1] Kirubakaran A, Shailendra J, Nema R. K, *Renew. Sust. Energ. Rev.* 13, 2430, **2009**
- [2] Huang X, Zhang Z, Jiang J, *Fuel Cell Technology for Distributed Generation: An Overview*, IEEE ISIE, Montreal, Canada, **2006**
- [3] Gou B, Ki Na W, Diong B, *Fuel Cells: Modeling, Control, and Applications*, CRC Press Boca Raton, FL, **2010**
- [4] <http://m.sum-battery.com/news/the-new-ev-charging-scheme-combines-fuel-cells.com>
- [5] Scrosati B, *Celle a Combustibile*, La Grande Scienza, Enciclopedia Italiana Treccani, **2003**
- [6] Chen E, *Thermodynamics and Electrochemical Kinetics Fuel Cell Technology Handbook*, Hoogers G, CRC Press Inc., Boca Raton FL, Eds. **2002**
- [7] Dickinson E. J. F, Hinds G, *J. Electrochem. Soc.*, 166, 4, F221, **2019**
- [8] Pinar F.J, Rastedt M., Pilinski N., Wagner P. *Characterization of HT-PEM Membrane-Electrode-Assemblies* In: Li Q., Aili D., Hjuler H., Jensen J. (eds) *High Temperature Polymer Electrolyte Membrane Fuel Cells*. Springer, Cham **2016**
- [9] Kundu S, Simon L.C, Fowler M, Grot S, *Polymer*, 46, 11707, **2005**
- [10] Ahmad M.I, Zaidi S.M. J, Rahman S.U, *Desalination*, 193, 387, **2006**
- [11] Peighambardoust S.J, Rowshanzamir S, Amjadi M, *Int. J. Hydrogen. Energy*, 35, 9349, **2010**
- [12] Maurtiz K. A, Moore R. B, *Chem. Rev.*, 104, 4535, **2004**
- [13] Li L, Zhang J, Wang Y, *J. Membr. Sci.* 226, 159, **2003**
- [14] Xing P, Robertson G.P, Guiver M.D, Mikhailenko S.D, Wang K, Kaliaguine S, *J. Membr. Sci.* 229, 95, **2004**
- [15] Bauer B, Jones D.J, Rozière J, Tchicaya L, Alberti G, Casciola M, Massinelli L, Peraio A, Besse S, Ramunni E, *J. New Mater. Electrochem. Syst.*, 3, 93, **2000**
- [16] Kreuer K.D, *J. Membr. Sci.*, 185, 29, **2001**
- [17] Adjemian K.T, Dominey R, Krishnan L, Ota H, Majsztrik P, Zhang T, Mann J, Kirby B, Gatto L, Velo-Simpson M et al, *Chem. Mat.*, 18, 2238, **2006**
- [18] Branchi M, Sgambetterra M, Pettiti I, Panero S, Navarra M.A, *Int. J. Hydrogen. Energy*, 40, 14757, **2015**
- [19] Lufrano F, Baglio V, Di Blasi O, Staiti P, Antonucci V, Aricò A.S, *Solid State Ion.*, 216, 90, **2012**
- [20] Navarra M.A, Croce F, Scrosati B, New, high temperature superacid zirconia-doped Nafion™ composite membranes. *J. Mater. Chem.*, 17, 3210, **2007**
- [21] Nikhil H.J, Dunn K, Datta R, *Electrochim. Acta*, 51, 553, **2005**
- [22] Arico A.S, Baglio, V, Di Blasi A, Creti P, Antonucci P.L, Antonucci V, *Solid State Ion.*, 152, 251, **2003**

- [23] Carette L, Friedirch A, Stimming U, *Chemphyschem.*, 1, 161, **2000**
- [24] Kabir S, Serov A, Artyushkova K, Atanassov P, *ACS Catal.* 7,10, **2017**
- [25] Morozan A, Josselme B, Palacin S, *Energy Environ. Sci.*, 4, 1238, **2011**
- [26] Nie Y, Li L, Wei, Z. *Chem. Soc. Rev.* 44, 2168, **2015**
- [27] Zhou Y et al, *Energy Environ. Sci.* 3, 1437, **2010**
- [28] Peuckert M, Yoneda T, Betta R. A. D, Boudart M, *J. Electrochem. Soc.* 133, 944, **1986**
- [29] Kinoshita K. J, *Electrochem. Soc.* 137, 845, **1990**
- [30] Zhao Z, Li M, Zhang L, Dai L, Xia Z, *Adv. Mater.* 27, 6834, **2015**
- [31] Liang C. C, Juliard A. L, *J. Electroanal. Chem.*, 9, 390, **1965**
- [32] Toda T, Igarashi H, Uchida H, Watanabe M, *J. Electrochem. Soc.*, 146, 3750, **1999**
- [33] Chen S.L, Kucernak A, *J. Phys. Chem. B* , 108, 3262, **2004**

CHAPTER II

NON-STOICHIOMETRIC CALCIUM TITANATE PEROVSKITES SYNTHESIS AND CHARACTERIZATIONS

2.1 INTRODUCTION

Inorganic perovskite-type oxides are fascinating nanomaterials for wide applications in catalysis, fuel cells, and other electrochemical devices thank to their tunable properties and their intrinsic ionic and electrical conductivity and due to their catalytic activity^[1,2].

The Calcium Titanate, with a chemical formula of CaTiO_3 , was the first perovskite mineral discovered by mineralogist Gustav Rose in 1839 and was named in honor of the mineralogist Lev Perovski (1792–1856).

Generally, materials which have the same crystal structure of CaTiO_3 (ABO_3) are referred to as perovskite materials.

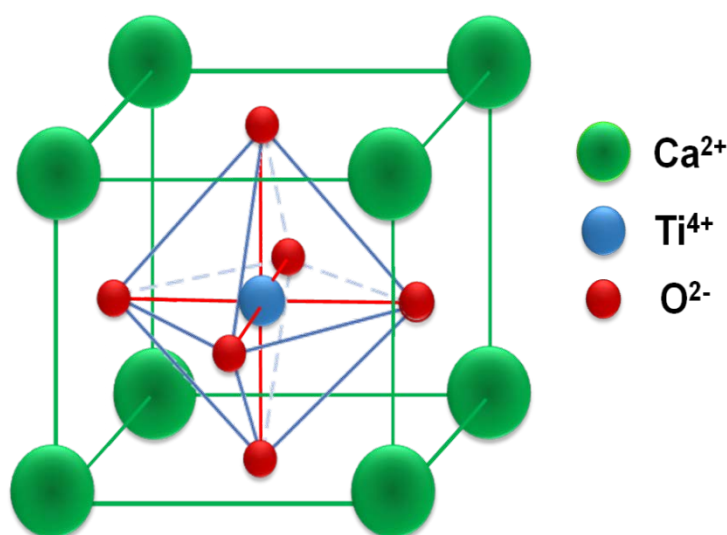


Figure 1: *Ideal cubic calcium titanate perovskite (CaTiO_3) structure*

The structure of an ideal cubic perovskite is shown in Figure 1, where the A cations are shown at the corners of the cube, and the B cation in the centre with oxygen ions in the face-centred positions. The ideal cubic perovskite structure is not very common, generally the perovskite oxides have structure slightly distorted^[3].

Compared with other types of metal oxides, a major superiority of perovskite oxides is their compositional and structural flexibility. This could be explained considering the perovskite design ABO_3 , that allows to accommodate several doping agents such as metal transition elements of both the A-site and/or B-site providing oxygen vacancies in the lattice of the perovskite^[4].

It is expected that the main features of perovskites are controlled by the size and nature of both A and B cations in the ABO_3 structure and that the occupation of the B-site by several ions with different acid/base properties affect the stability of perovskites.

Recently, the perovskite oxides role as oxygen electrocatalysts in alkaline solutions has obtained a great attention, owing to their favorable catalytic activity toward both oxygen reduction (ORR) and evolution reactions (OER). Based on the Sabatier principle, the optimal ORR/OER catalyst should possess moderate surface-oxygen interaction energy allowing the right balance between the adsorption and desorption of the reactants and the intermediate^[5,6,7].

However, the measurement of the adsorbate binding energy on surfaces it is not so easy. Considerable efforts in the past have been addressed to identify electronic structure parameters associated with the adsorbate binding energy in order to correlate the ORR/OER activity with new catalysts design^[8,9].

Nowadays, it is generally believed that the ORR and the OER catalytic activity of perovskites is dependent on the B-site transition metal element while the role of lattice oxygen or oxygen vacancies in perovskites was often overlooked.

In fact, taking as esample the oxygen evolution reaction, the most widely accepted mechanism for the OER on perovskites, is the proposed Adsorbate Evolution Mechanism (AEM) derived from the work by Bockris and Otagawa^[10]. In general, the overall AEM for perovskites in alkaline media is based on four single-electron charge-transfer steps on the surface active site of B-site metal.

As reported in figure 2a, a series of reaction intermediates, HO*, O*, and HOO* take place accompanied with the redox of the B-site metal cations (Figure 2a)^[11].

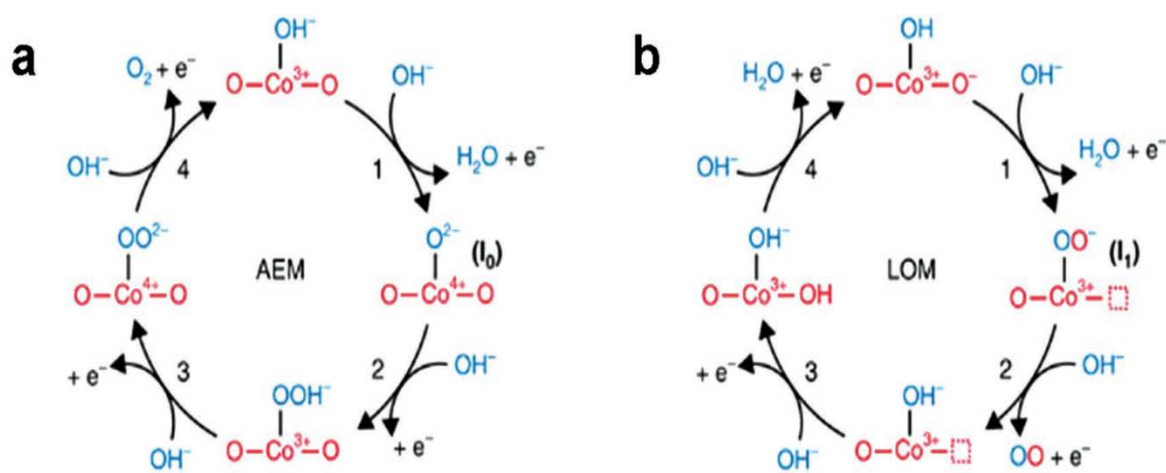


Figure 2: Proposed a) AEM and b) LOM for OER on perovskite ^[12]

Recently, a new Lattice Oxygen-participated Mechanism (LOM) for perovskites based on the exchange of lattice oxygen species (Figure 2b) was reported, demonstrating the key role of surface oxygen vacancies for perovskite-type catalysts. Indeed, the oxygen vacancies can govern the physical-chemical parameters of the ionic diffusion rates and influence the electronic structure of the perovskite oxide^[12].

The beneficial effect of an oxygen vacancy was demonstrated by several studies regarding enhancing the both ORR/ OER activity.

One example is that of Du et al., who prepared several of nonstoichiometric $\text{CaMnO}_{3-\delta}$ ($0 < \delta \leq 0.5$) oxides by a low-temperature thermal reduction method. Electrochemical investigations revealed an improvement of the ORR specific activity for oxygen-deficient $\text{CaMnO}_{3-\delta}$ in comparison with the stoichiometric CaMnO_3 . Remarkably, the nonstoichiometric $\text{CaMnO}_{3-\delta}$ with δ near 0.25 exhibited the highest ORR activity, which is comparable to that of the benchmark Pt/C^[13].

The importance of oxygen vacancies on oxygen reaction activities has also been demonstrated in other types of oxides such as $\text{Ti}_{0.7}\text{Sn}_{0.3}\text{O}_2$, $\text{Ti}_{0.7}\text{Mo}_{0.3}\text{O}_2$ ^[14,15]. These oxides have shown the ability to establish a synergistic co-catalytic effect between the metal oxide and the Pt catalyst resulting in modifying the electronic nature of the metal and in an enhancement of the catalytic activity and durability for the ORR.

Nevertheless, the nonstoichiometry of transition metal oxides become more active towards the ORR thank to the introduction of oxygen vacancies at their surface. These, can modify the oxidation state of metal species to form active catalytic sites able to adsorb O_2 and to introduce new electronic levels in the energy gap. These properties exerts a prominent effect on the performance of several electrochemical systems such as lithium-ion batteries and fuel cells^[16,17].

Furthermore, the presence of the oxygen vacancies in the structure can play a key role as active sites for the dissociative absorption of water for which the protons conductivity is favored. The last aspect could be used to improve the hydrophilicity of the oxide by the protonation of the lattice oxygen ions. This phenomenon seems to be predominant in perovskite-type oxides due to the low formation enthalpies of oxygen ions as a consequence of low bond strengths and strong relaxation effects. The last aspect could be used to improve the hydrophilicity of the oxide by the protonation of the lattice oxygen ions^[18,19].

In proton-conducting fuel cells, perovskite-type transition-metal oxides have shown a high mobility of protonic defects and can be used as proton-conducting electrolytes. Li et al, have studied by a periodic DFT + U calculations the hydrogen transport behaviors on the defect free and defective LaMO_3 surfaces ($M = \text{Cr}, \text{Mn}, \text{and Fe}$). In the presence of oxygen vacancies, the vehicle mechanism in which hydrogen hops together with the underlying oxygen would dominate on LaMnO_3 and LaFeO_3 , whereas on the defective LaCrO_3 the Grotthuss mechanism prevails^[20].

With the aim to combine all the features of the materials above-mentioned, we have focused our study on nonstoichiometric perovskites titanium oxide, Calcium Titanate ($\text{CaTiO}_{3-\delta}$, CTO figure 3) and Iron-doped Calcium Titanate perovskite ($\text{CaTi}_{1-x}\text{Fe}_x\text{O}_{3-\delta}$, CTFO), both used as Pt/C promoter for the ORR.

Furthermore the CTO perovskite was also used as water retention and reinforcing additive in low humidity proton exchange membranes.

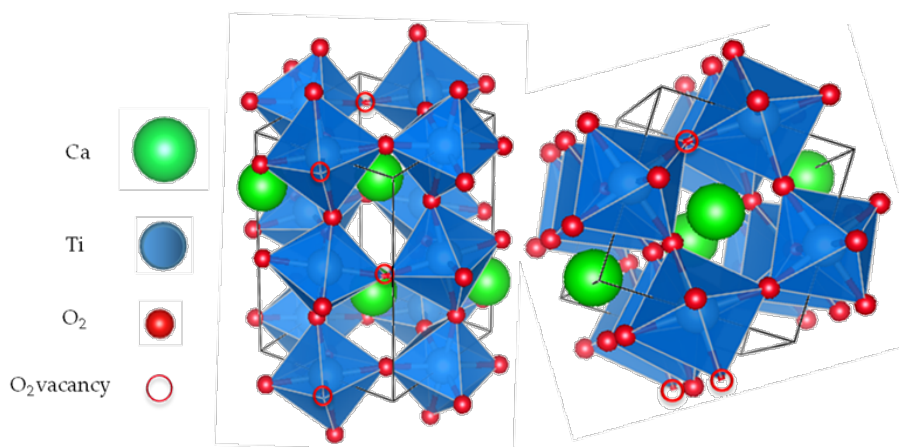


Figure 3: A nonstoichiometric Orthorhombic Calcium Titanate perovskite ($\text{CaTiO}_{3-\delta}$) structure

2.2 SYNTHESIS OF NON-STOICHIOMETRIC CALCIUM TITANATE PEROVSKITE $\text{CaTiO}_{3-\delta}$ AND $\text{CaTi}_{1-x}\text{Fe}_x\text{O}_{3-\delta}$

A hydrothermal synthesis followed by a calcination treatment was used to obtain $\text{CaTiO}_{3-\delta}$ perovskite. Pristine CaTiO_3 is synthesized during a solvothermal process as report in ^[21] using titanium isopropoxide and calcium dichloride dihydrated as precursors. Pluronic F127 was used both as structure-directing agent and as a reducing agent in order to promote the formation of oxygen defects. All reagents are Sigma Aldrich products.

Therefore, the $\text{CaTiO}_{3-\delta}$ was prepared according to the following procedure: Pluronic F127 was added to ethanol (molar ratio 1:4) in vigorous stirring for 20 minutes at 60°C. Subsequently, titanium isopropoxide was dripped into the above solution and the TiO_2 sol was obtained. Meanwhile, calcium dichloride was dissolved in deionized water and after 15 minutes it was added into the mixture. A 3M NaOH solution was added to have an alkaline environment where the complete dissolution of TiO_2 and its conversion to CaTiO_3 occurred. The solution was transferred in an autoclave and treated at 180°C for 24 h followed by natural cooling to room temperature. Afterwards the solid product was centrifuged and washed several times with bi-distilled water.

Finally, the perovskite was calcined for 3 h at 550°C (heating rate 3°C/min) to remove the occluded template. This step, where the polymer is oxidized creates a reductive environmental near the oxide surface facilitating the formation of oxygen defects e/o vacancy as mentioned about zirconium oxide based catalyst^[22].

A High Energy Ball Milling (Fritsch Pulverisette P6 mill, Idar-Oberstein, Germany) was used to synthesize the iron-doped calcium titanate perovskite ($\text{CaTi}_{1-x}\text{Fe}_x\text{O}_{3-\delta}$, CTFO) using stoichiometric amounts of CaCO_3 , TiO_2 and $\text{FeO}(\text{OH})$. These compounds were mixed for 5 hours and calcined at 800°C for 3 hours under argon atmosphere (heating rate 3°C/min).

2.2.1 PHYSICAL-CHEMICAL CHARACTERIZATIONS

X-ray diffraction (XRD) analysis was carried out to study the crystalline phase of perovskites. The X-ray analysis was recorded using a Rigaku D-Max Ultima + diffractometer, equipped with a Cu K α radiation source and graphite monochromator, in the 2 θ range 20-70°. The crystallite size was calculated using the Maud code.

N₂-adsorption experiments were used for the determination of pores size distributions and for the evaluation of the specific surface area of the powder by the Brunauer-Emmett-Teller (BET) equation using a Micromeritics ASAP 2010. In order to remove physisorbed water, the sample was subjected to a thermal pre-treatment at 200 °C for 2 h.

Through a high resolution field emission scanning electron microscopy (HR-FESEM) analysis, performed by an Auriga Zeiss instrument at the CNIS research centre of Sapienza University of Rome, the morphology and size of the inorganic additive were evaluated.

Thermal analysis were conducted by thermal gravimetric (TG) analysis performed with a TGA/SDTA851 Mettler-Toledo instrument. It was carried out under air (80 ml/min) in a temperature range between 25 °C and 1000 °C.

Infrared spectroscopy (FTIR) are performed over the frequency range 400-4000 cm⁻¹. The FTIR measurements are carried out at room temperature using a Bruker FTIR

Raman spectra were collected with an InVia Reflex spectrometer from Renishaw. Depending on the sample, 5 or 10% of the nominal power (i.e., 300 mW) of a 785 nm diode laser was used. The spectrometer was calibrated using the 520.6 cm⁻¹ line of a silicon wafer. The analysis of the spectra was performed using the WIRE 5.0 software.

The composition of oxygen in the prepared CaTiO_{3- δ} was estimated by means of a home-made Sieverts^[23] apparatus usually used for the absorption of hydrogen. In this case it was employed to evaluate the oxygen non-stoichiometric (δ). Therefore, the apparatus was implemented with an inlet for oxygen gas.

The sample of calcium titanate with an initial mass of 161 mg was heated up to 480 °C and afterwards it was exposed to an O₂ atmosphere of about 1 bar. The pressure loss during the temperature process was considered as the content of oxygen.

X-ray photoelectron spectroscopy (XPS) measurements were carried out by a Physical Electronics (PHI) 5800-01 spectrometer. A monochromatic Al K α X-ray source was used at a power of 350 W. XPS data were interpreted by using the online library of oxidation states implemented in the PHI MULTIPAK 6.1 software and the PHI Handbook of X-ray photoelectron spectroscopy.

2.3 RESULTS AND DISCUSSION

CALCIUM TITANATE PEROVSKITE $\text{CaTiO}_{3-\delta}$

The XRD pattern (Figure 4) corresponds to an orthorhombic CaTiO_3 phase characterized by Pnma space group. The pattern in blue corresponds to the CaTiO_3 reference (ICSD - 165801). The average crystallite size, determined by the Maud code, is 145 ± 5 nm.

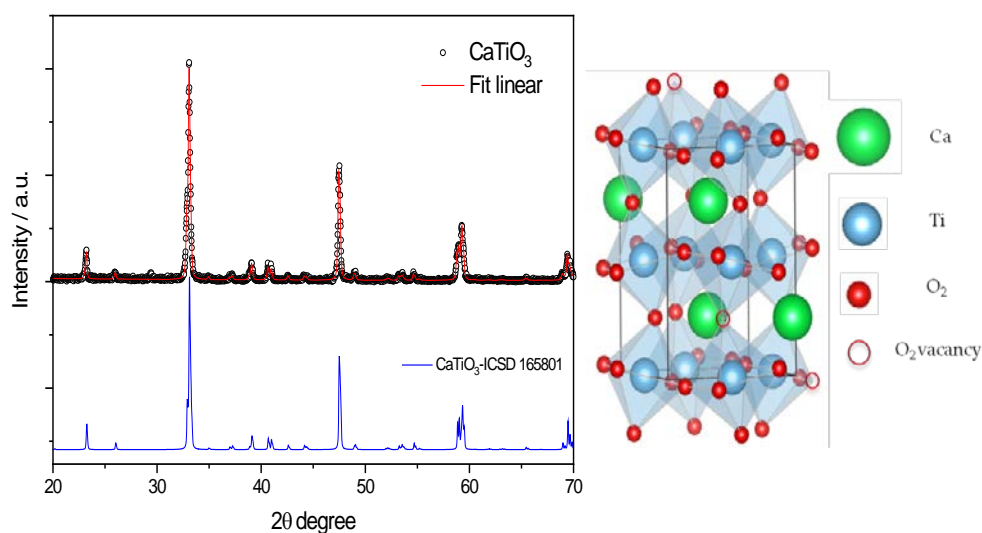


Figure 4: X-ray diffraction pattern of the synthesized $\text{CaTiO}_{3-\delta}$ powder

Based on Brunauer-Emmett-Teller (BET) analysis, analysis, the specific surface area measured by nitrogen adsorption was found to be $6.6 \pm 0.5 \text{ m}^2\text{g}^{-1}$. The sample shows meso- and macro-pores centered at two high distribution areas of the pore size, around 20 \AA and 150 \AA . The total volume of pores was $0.0320 \text{ cm}^3/\text{g}$. These results are in agreement with the literature expectations^[21], even though powders having smaller crystallite sizes and higher surface areas could be obtained by using different synthesis pathways.

SEM images of the $\text{CaTiO}_{3-\delta}$ powder are reported in Figure 5. Homogeneous prismatic, quasi-cubic particles of the perovskite as well as the presence of holes/surface imperfections can be observed at high magnification (Figure 5b).

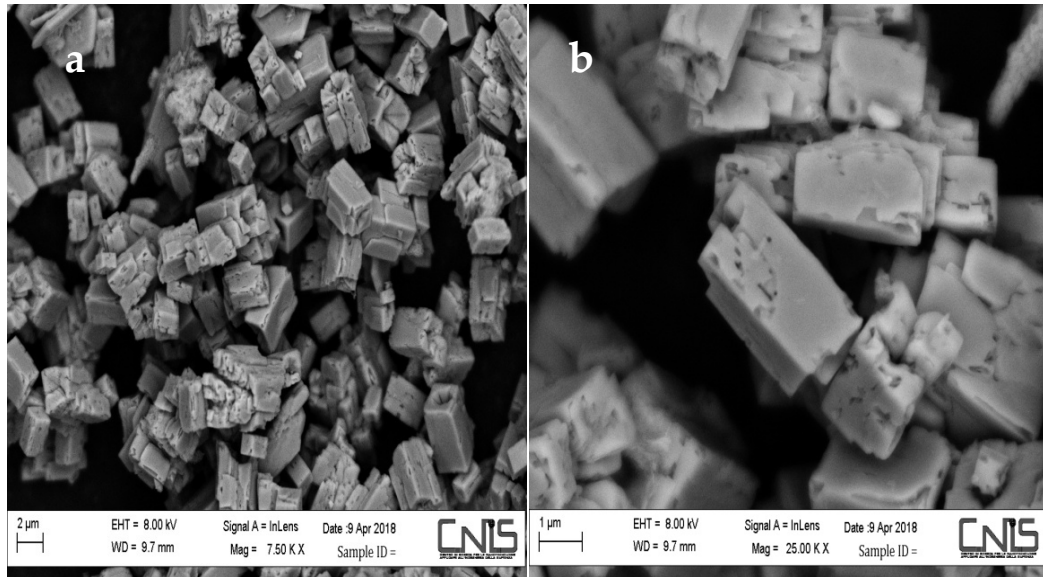


Figure 5: SEM images of CTO sample at (a) low and (b) high magnification

Figure 6 shows Infrared spectra analysis of the calcium titanate. The typical bands of CTO structure are observed at 434 cm^{-1} and 560 cm^{-1} related to the stretching vibration of Ti-O and bridging stretching modes of Ti-O-Ti respectively^[24].

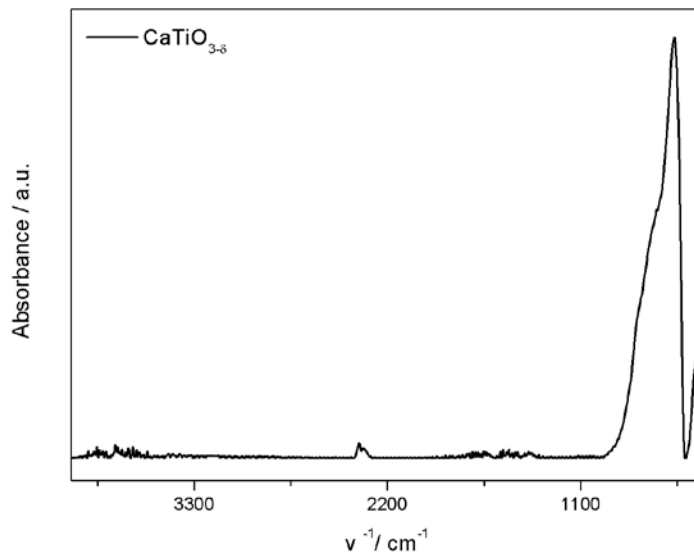


Figure 6: FTIR spectra of CTO sample

The unpolarized Raman spectrum of $\text{CaTiO}_{3-\delta}$ perovskite (Figure 7) shows a number of sharp peaks superimposed on a broad feature band between 150 and 600 cm^{-1} ; a second broad band between 650 and 850 cm^{-1} can be found.

All the bands are assigned to first order Raman scattering^[25] and they are interpreted in terms of internal TiO_6 stretching, bending vibrations and external modes confirming the IR results.

The bands assignment are reported in table 2.

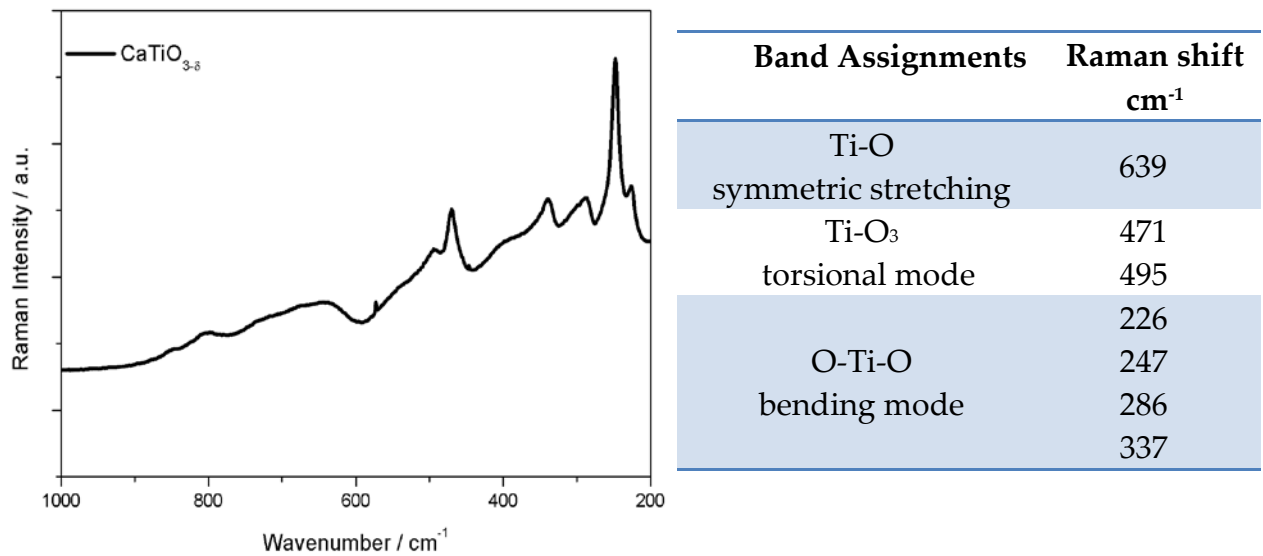


Figure 7: Raman spectra of CTO sample (on the left)

Table 2: Band assignments Raman spectra of CTO sample (on the right)

In order to evaluate the thermal stability of the powder a thermogravimetric analysis was carried out under air (80 ml/min) in a temperature range between 25°C and 1000°C. In Figure 8, TGA curve reveals a weight increase of the powder sample from room temperature up to ca. 400°C, this behavior could be related to CTO surface properties such as the presence of the oxygen vacancies in the lattice of the perovskite enabling the gas adsorption.

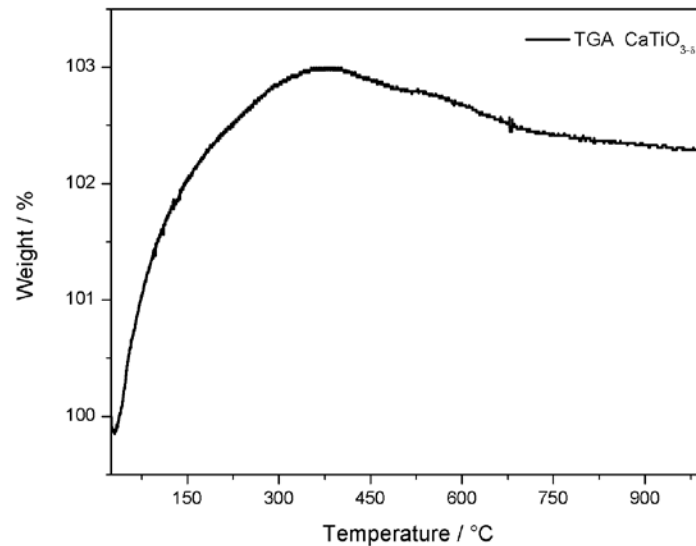


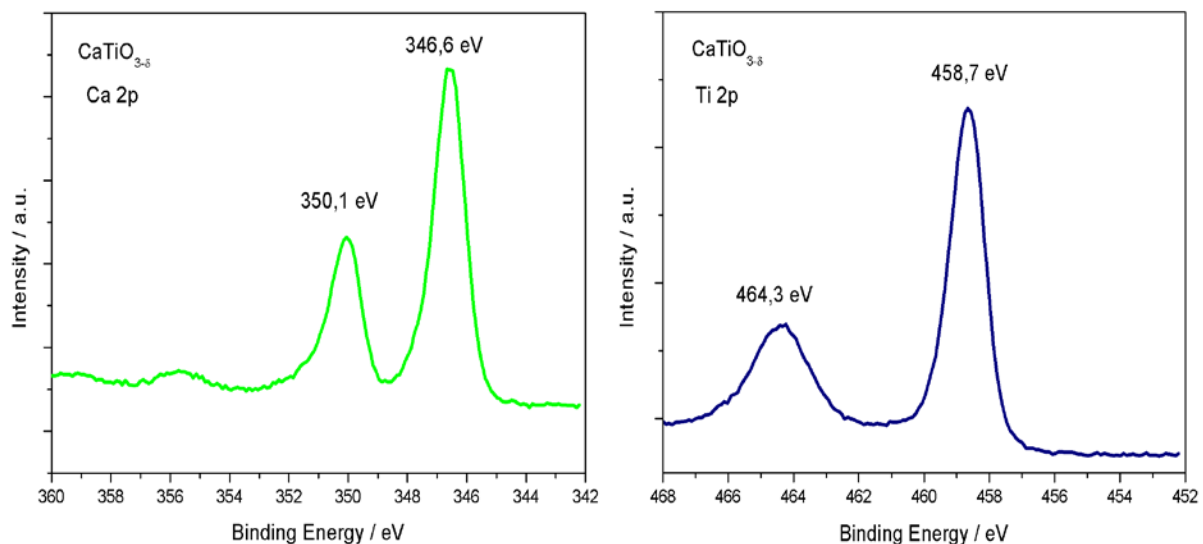
Figure 8: TGA in air of $\text{CaTiO}_{3-\delta}$ sample

To confirm the presence of oxygen defects present on the surface of the CTO, the sample was exposed to an O_2 atmosphere of $P \approx 1$ bar at 480°C . At these conditions, the sample is able to absorb $\approx 0.3\%$ of its initial mass, reaching a steady state. If one consider that all the absorbed oxygen fills the vacancies initially present in the sample, one would have an initial stoichiometry of the $\text{CaTiO}_{3-\delta}$, with $\delta \approx 0.025$.

Here, the surface properties and oxidation states of the elements in the CTO compound have been investigated by XPS measurements.

XPS spectra for the $\text{CaTiO}_{3-\delta}$ perovskite contained the peaks originating from calcium, titanium and oxygen. The binding energy values for each elements have been obtained by peak fitting analysis with Gaussian-Lorentz function and, as reported in table 1.

A XPS spectra for Ca 2p, Ti 2p, and O 1s regions are shown in Figure 9



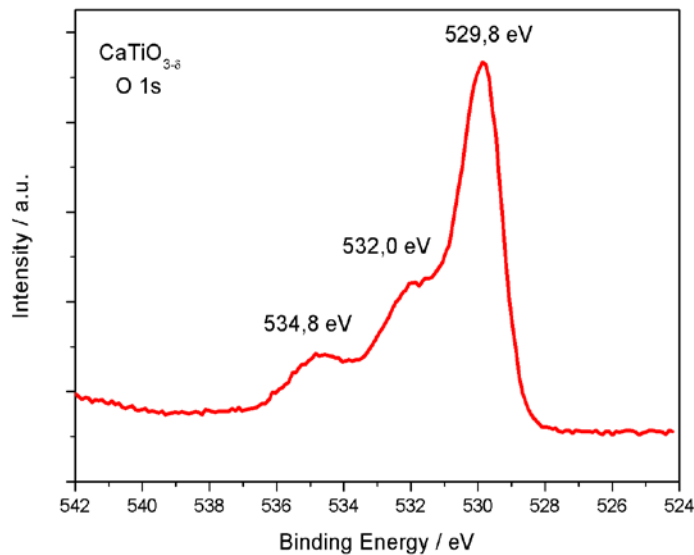


Figure 9: XPS spectra of Ti 2p, Ca 2p, and O 1s regions for the $\text{CaTiO}_{3-\delta}$

In particular, the observed peaks of the Ca, at 350.1 eV and 346.6 eV, are related to Ca $2p_{3/2}$ and Ca $2p_{1/2}$ respectively, confirming the presence of Ca^{2+} . The two main peaks observed for the transition metal (Ti) are attributed to Ti $2p_{3/2}$ at 464.3 eV and to Ti $2p_{1/2}$ at 458.7 eV of the Ti^{4+} cationic structure^[26]. The XPS spectrum for the O 1s region is deconvoluted into three peaks originating from anhydrous oxide (O^{2-}), the hydroxide group (OH^-), and adsorbed water (H_2O) at 529,8 eV, 532,0 eV and 534,8 eV respectively^[27].

The formation of extra features in the O 1s spectra can be related to the adsorption of oxygen-containing species on the surface of the CTO sample. This indicates that there is water adsorbs at defect sites in the perovskite lattice that lead to the presence of two different peaks due to OH^- or to an O^{2-} species.

However, oxygen vacancies in oxides may lead to small peak shifts in the O 1s spectra, in our case these differences in the energies are not visible because of the small amount of oxygen vacancies ($\delta \approx 0.025$) presents in the perovskite structure.

2.4 RESULTS AND DISCUSSION

IRON-DOPED CALCIUM TITANATE PEROVSKITE ($\text{CaTi}_{1-x}\text{Fe}_x\text{O}_{3-\delta}$)

Figure 10 displays the XRD pattern of the synthesized $\text{CaTi}_{1-x}\text{Fe}_x\text{O}_{3-\delta}$ (CTFO) sample. The phase correspond to an orthorhombic CTFO characterized by Pnma space group. The pattern in green corresponds to the $\text{CaTi}_{1-x}\text{Fe}_x\text{O}_{3-\delta}$ reference (ICSD - 5187801). The average crystallite size was determined by the Maud code and it corresponds to 68 ± 1 nm.

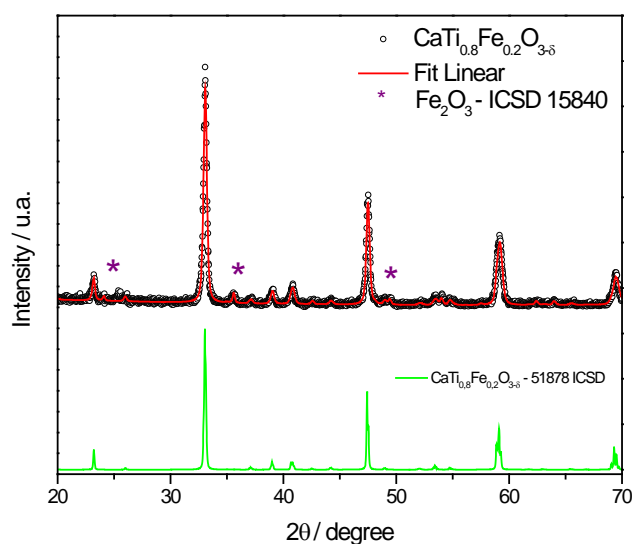


Figure 10: X-ray diffraction pattern of the synthesized $\text{CaTiO}_{3-\delta}$ powder

As a minor component, iron oxide Fe_2O_3 (ICSD- 15840) with crystallite size of about 100 nm and relative amount of 7%, was found.

SEM images of the synthesized perovskite were studied to evaluate the morphology of the powder sample and they are shown in Figure 11.

From the images, it is difficult to identify individual particles, nonetheless uniform irregular shaped pores can be observed.

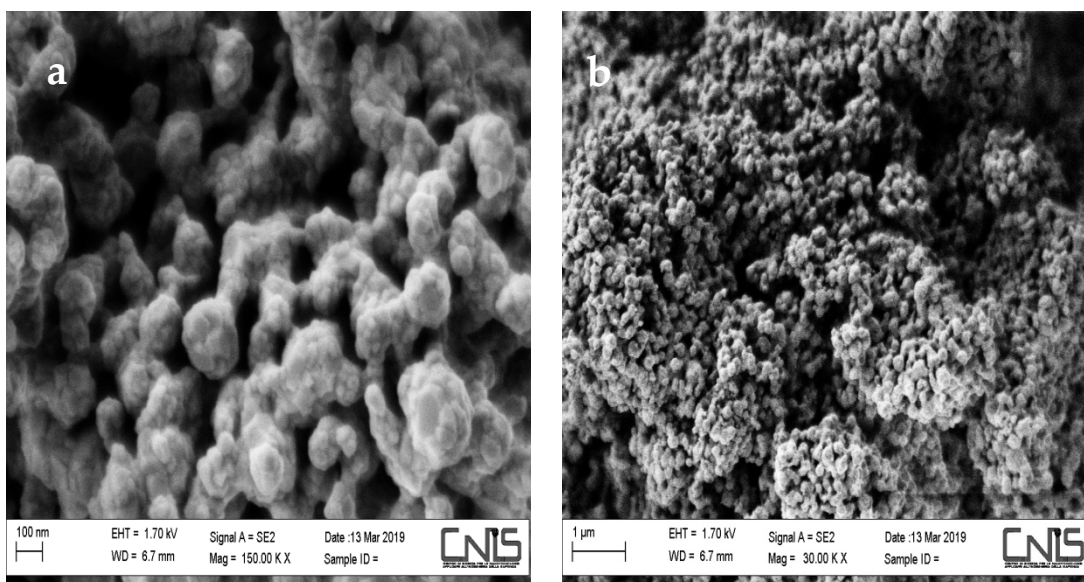


Figure 11: SEM images of CTFO sample at (a) low and (b) high magnification

A thermogravimetric analysis was carried out under air (80 ml/min) in a temperature range between 25°C and 1000°C.

Figure 12 shows the TGA curves for the $\text{CaTi}_{1-x}\text{Fe}_x\text{O}_{3-\delta}$ perovskite. It shows a weight gain observed from room temperature up to 400°C. This behavior was also previously observed in $\text{CaTiO}_{3-\delta}$ oxides and it has been related to a slight incorporation of oxygen atoms thank to the presence of the oxygen vacancies into the unit cell of the perovskite.

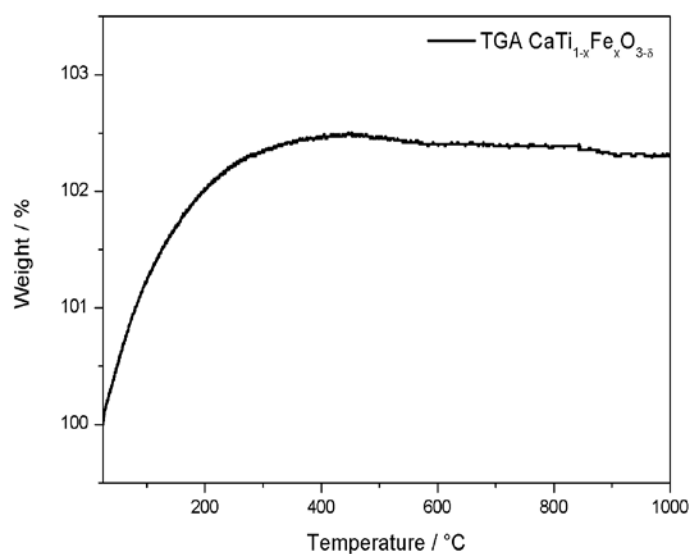


Figure 12: TGA in air of $\text{CaTi}_{1-x}\text{Fe}_x\text{O}_{3-\delta}$ sample

FTIR vibrational spectroscopy of the sample is shown in figure 13. It reveals the typical bands corresponding to CaTiO_3 , due to the stretching of Ti-O and bending vibration of O-Ti-O as discussed for the CTO sample in the previous paragraph.

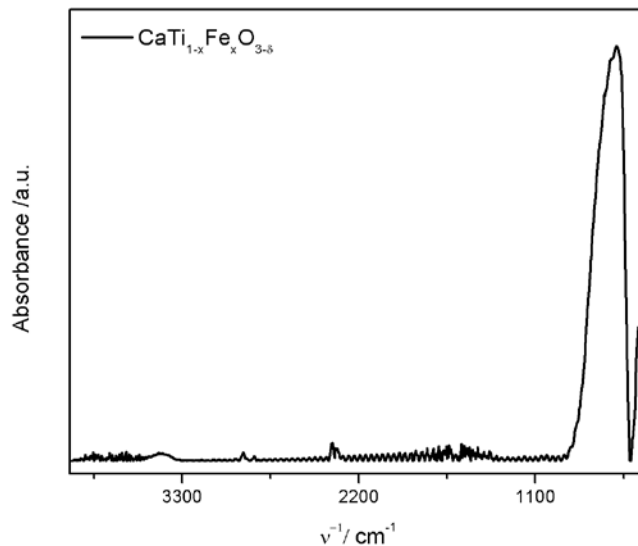


Figure 13: FTIR spectra of CTFO sample

However, new peaks related to the dopant transition element (Fe^{3+}) haven't been found. The only change appeared in the positions of stretching Ti-O band which is shifted at higher frequency $\sim 597 \text{ cm}^{-1}$ compared to the $\text{CaTiO}_{3-\delta}$ band which is placed at 560 cm^{-1} .

This behavior could be explained considering that, at frequency of 560 cm^{-1} and 462 cm^{-1} it is possible to find Fe_2O_3 peaks due to the stretching vibration of Fe-O^[28]. These peaks that are overlapped with perovskite peaks, confirm the formation of Fe_2O_3 phase.

Nevertheless, the Fe-O bands can confirm also the presence of the Fe ions substitute the Ti^{4+} ions in the B site of the perovskite structure because the presence of Fe^{3+} should increase the covalency of the Fe-O bonds^[29].

Both aspects are in agreement with the XRD measurement.

2.5 CONCLUSIONS

A nonstoichiometric Calcium Titanate ($\text{CaTiO}_{3-\delta}$, CTO) perovskite was synthesized via an original template hydrothermal method.

Functionality of this additive, the presence of oxygen vacancies in the lattice of the perovskite, has been obtained by the oxidation of the polymer Pluronic F127 during the calcination process. This step has created a reductive environment near the oxide surface facilitating the formation of oxygen vacancy.

On the basis of physical-chemical characterizations, we have demonstrated the features of this sample especially the presence of oxygen vacancies on the lattice of the perovskite enabling oxygen adsorption. This last aspect seems to be connect to the structure of the sample; the presence of holes or surface imperfections are clear visible from SEM images.

However, from oxygen vacancies analysis the amount of these oxygen active sites is not so high ($\delta \approx 0.025$), this could be explained considering the low amount of the template used for the Calcium Titanate synthesis with respect to the amount of both precursors.

Consequently, an optimization of the synthesis procedure will be considered in the future in order to obtain a major degree of defectivity of the perovskite.

However, in order to increase the amount of oxygen vacancies and enhance the electrical conductivity of the additive, an Iron-doped Calcium Titanate ($\text{CaTi}_{1-x}\text{Fe}_x\text{O}_{3-\delta}$ - CTFO) perovskite has been synthesized and characterized.

This perovskite was synthesized by a High Energy Ball Milling using stoichiometric amounts of CaCO_3 , TiO_2 and $\text{FeO}(\text{OH})$. By a preliminary chemical-physical characterizations we have obtained an orthorhombic $\text{CaTi}_{1-x}\text{Fe}_x\text{O}_{3-\delta}$ phase with iron oxide (Fe_2O_3) as minor component.

Despite the presence of Fe_2O_3 impurity, from TGA curve, the $\text{CaTi}_{1-x}\text{Fe}_x\text{O}_{3-\delta}$ perovskite has shown a weight gain from room temperature up to 400°C . This behavior, as explained for the $\text{CaTiO}_{3-\delta}$ sample, is due to the presence of oxygen vacancies in the lattice of the perovskite enabling the oxygen adsorption.

Other studies will be addressed both to improve the synthesis of CTFO in order to obtain a pure phase of the material and to understand better how the structure of CTFO could influence the performance of catalysts by new chemical-physical characterizations, such as X-ray photoelectron spectroscopy (XPS) and oxygen vacancies analysis.

REFERENCES

- [1] Pena M, Fierro J, *Chem. Rev.*, 101 , 1981, **2001**
- [2] Medarde M. L, *J. Phys. Condens. Matter*, 9 ,1679, **1997**
- [3] Goodenough J.B, *J. Phys. Chem. Solids*, 6 , 287, **1958**
- [4] Zhao Y, Hang Y, Zhang Y, Wang Z, Yao Y, He X, Zhang C, Zhang D, *Electrochim. Acta*, 232 , 296, **2017**
- [5] Hammer B, *Top. Catal.*, 37, 3, **2006**
- [6] Fabbri E, Mohamed R, Levecque P, Conrad O, Kötza R, Schmidt T.J, *ECS Transactions* , 64, 1081, **2014**
- [7] Sebastian D, Baglio V, Sun S, Tavares A.C, Aricò A.S, *ChemCatChem*, 7,911, **2015**
- [8] Matsumoto Y, Yoneyama H, Tamura H, *J. Electroanal. Chem.*, 79, 319, **1977**
- [9] Matsumoto Y, Yoneyama H, Tamura H, *J. Electroanal. Chem.*, 83, 237, **1977**
- [10] Bockris J.O, Otagawa T, *J. Electrochem. Soc.*, 131, 290, **1984**
- [11] Rong X, Parolin J, Kolpak A. M, *ACS Catal.*, 6, 1153, **2016**
- [12] Mefford J. T, Rong X, Abakumov A. M, Hardin W. G, Dai S, Kolpak A. M, Johnston K. P, Stevenson K. J, *Nat. Commun.*, 7, 11053, **2016**
- [13] Du J, Zhang T, Cheng F, Chu W, Wu Z, J. Chen, *Inorg. Chem.*, 53, 9106, **2014**
- [14] Gao Y, Hou M, Shao Z, Zhang C, Qin X, Yi B, *J. Energy Chem.*, 23 , 331, **2014**
- [15] Ho V.T, Pan C. J, Rick J, Su W. N, Hwang B. J, *J. Am. Chem. Soc.*, 133, 11716, **2011**
- [16] Ishihara A, Ohgi Y, Matsuzawa K, Mitsushima S, Ota K. I, *Electrochim. Acta*, 55, 8005, **2010**
- [17] Ota K. I, Ohgi Y, Nam K.D, Matsuzawa K, Mitsushima S, Ishihara A, *J. Power Sources* 196, 5256, **2011**
- [18] Li Q, Yin Q, Zheng Y.S, Sui Z.J, Zhou, X.G, Chen D, Zhu Y.A, 35, 9962, **2019**
- [19] Stølen S, Bakkenw E, Mohn C.E, *Phys. Chem. Chem. Phys.*, 8, 429, **2006**
- [20] Li Q, Yin Q, Zheng Y-S, Sui Z-J, Zhou X.G, Chen D, Zhu Y-A, *Langmuir*, 35, 9962, **2019**
- [21] Dong W, Song B, Meng W, Zhao G, Han G, *Appl. Surf. Sci.*, 349, 272, **2015**
- [22] Ohgi Y, Ishihara A, Matsuzawa K, Mitsushima S, Ota K, Matsumoto M, Imai H, *J. Electrochem. Soc.*, 160, F162, **2013**
- [23] Palumbo O, Brutti S, Trequattrini F, Sarker S, Dolan M, Chandra D, Paolone A, *Energies* 8, 3944, **2015**
- [24] Wang Y, Niu C, Wang L, Wang Y, Zhang X, Zeng G, *RSC Adv.*, 6, 47873, **2016**
- [25] McMillan P, Ross N, *Phys Chem Minerals* 16,21, **1988**
- [26] Yan Y, Yang H, Yi Z, Li R, X. Wang, *Micromachines*, 10, 254, **2019**
- [27] St Uhlenbrock et al, *J. Phys. Condens. Matter* 4, 7973, **1992**
- [28] Wu G., Tan X., Li G., Hu C., *J. Alloys Compd.*, 504, 371, **2010**
- [29] Abdel Aal A. et al, *Acta Physica Polonica A*, 126, 1318, **2014**

CHAPTER III

CALCIUM TITANATE PEROVSKITES USED AS ADDITIVE OF Pt/C CATALYST FOR OXYGEN REDUCTION REACTION IN ACIDIC MEDIA

3.1 INTRODUCTION TO ROTATING DISK ELECTRODE (RDE)

Rotating Disc Electrode (RDE) tests and the following results were performed when I visited the CNR-ITAE Institute of Messina.

Electrode preparation and cell apparatus are referred to a technology developed in the Institute and better described elsewhere^[1].

The majority of oxygen reduction reaction (ORR) fundamental research is conducted using the Rotating Disc Electrode. Particularly, in studying electrode reaction kinetics and mechanisms, RDE has shown advantages in measuring reaction electron transfer number, reaction kinetic constant, and reaction intermediates.

Furthermore, trends of activity and durability in RDE studies can be used to predict trends in Fuel Cells.

Figure 1 shows the typical rotating disk electrode which is mounted in the shaft of a controllable-speed motor and rotated with constant angular velocity (ω) respect to an axis perpendicular to the plain disk surface.

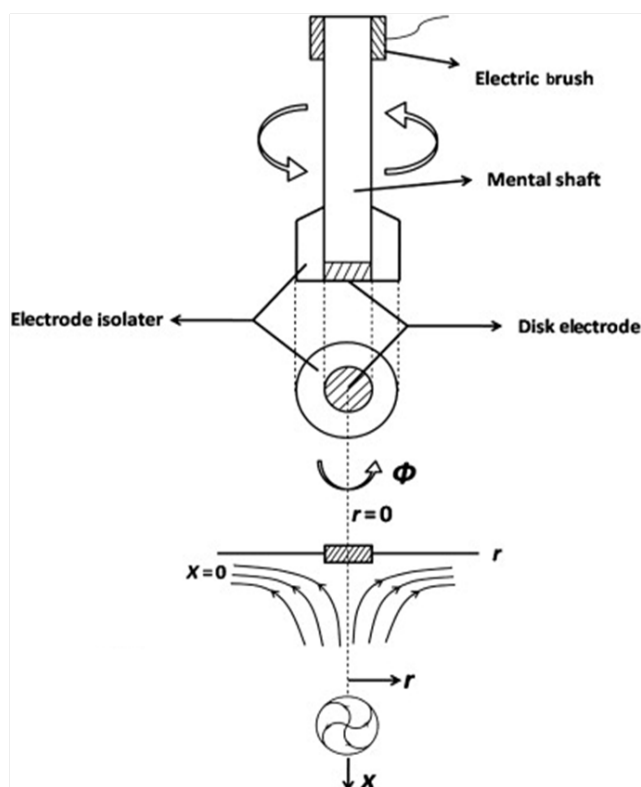


Figure 1: Rotating disk electrode representation^[2]

As a result of this rotation, the fluid develops a radial velocity that moves it away from the disk centre. This fluid is refilled by a flow normal to the surface^[2].

Cyclic voltammetry (CV) is the most useful technique in electrochemistry to obtain qualitative information about catalysts and electrochemical reactions, such as the electrochemical response of catalysts with respect to some electrochemical reactions.

In our case, this technique has been used to evaluate both the stability and the activity properties of both composite and no Pt catalysts, through the determination of the electrochemically active surface area (ECSA) which is fundamentals to understand the state of the catalysts and the electrode.

Measuring the ECSA before and after stability tests is useful to quantify the degradation properties. As stability test the most used is the Accelerated Degradation Test (ADTs), the electrode, in this case, is subjected at about 1000 CVs at high rate.

For carbon supported Pt, the ECSA is measured performing CV in acidic solution, under inert environmental and integrating the hydrogen desorption region. Thus, taking the area under the obtained curve, the ECSA was determinate by the following formula

$$ECSA = Q_H / Q_{dm} \quad (3.1)$$

where Q_H is the total charge obtained from the hydrogen desorption peak in the CV curve and Q_{dm} which is $0,21 \text{ mC cm}^{-2}$ is the density of electron charge in the hydrogen layer when a clean Pt surface is covered by a monolayer of hydrogen atoms with 100% surface coverage^[3].

Hydrodynamic linear sweep voltammogram (LSV) is a technique that we have used to acquire informations on ORR mechanism on a catalyst surface, studying and recording it at different rotations of the electrode. Subsequently current density obtained at different rotation speed was used to construct Koutecky–Levich (K–L) plot.

K–L plot is derived from the K–L equation as the following

$$1/J = 1/J_L + 1/J_K = 1/B\omega^{1/2} + 1/J_K \quad (3.2)$$

where, J , J_L , and J_K are the measured current density, the diffusion-limiting current density and the kinetic-limiting current density, respectively. ω is the rotation speed of the RDE and B is the Levich constant.

The slope obtained from the plot of $1/J$ versus $1/\omega^{1/2}$ is used to estimate the Levich constant. Consequently, the number of electrons transferred to each oxygen molecule was estimated from the Levich equation as the following

$$i_L = 0,62 nFC_0(D_0)^{2/3}\nu^{-1/6} \quad (3.3)$$

where, F is the Faraday constant ($96,485 \text{ C/mol}$), D_0 is the diffusion coefficient of oxygen in the electrolyte, ν is the kinematic viscosity of the electrolyte, and C_0 is the bulk oxygen concentration in the electrolyte^[4].

3.2 CATALYTIC LAYER PREPARATION

The catalytic inks were prepared by sonicating each catalyst in isopropyl alcohol and in the presence of 30 wt.% Nafion for 30 minutes^[5].

To test the first perovskite, $\text{CaTiO}_{3-\delta}$, four different catalytic compositions were prepared and compared, *i*) Pt/C (E-TEK with 20 wt.% Pt content with respect to C) used as reference, *ii*) Pt/C + perovskite, with Pt:CTO 1:1 weight ratio, *iii*) Pt/C + CTO, with Pt: CTO 1:2 weight ratio and *iv*) Pt/C + CTO, with Pt: CTO 1:2.5 weight ratio.

To study the second perovskite, $\text{CaTi}_{1-x}\text{Fe}_x\text{O}_{3-\delta}$, two different catalytic compositions were prepared and compared *i*) Pt/C (E-TEK with 20 wt.% Pt content with respect to C) used as reference, *ii*) Pt/C + CTFO, with Pt:CTFO 1:0,5 weight ratio and *iii*) Pt/C + CTFO, with Pt:CTFO 1:1 weight ratio.

Several droplets of the ink were deposited onto the GC disk electrode to obtain a constant Pt loading equal to $50 \mu\text{g cm}^{-2}$ for all the compositions above-mentioned. Before each measurement the GC was polished with alumina suspension using an OP-felt cloth.

3.2.1 ELECTROCHEMICAL INVESTIGATIONS

The electrochemical measurements of the catalysts were performed using a properly designed three-electrode cell configuration^[6,7]. An Hg/Hg₂SO₄ electrode was employed as reference electrode and it was connected to the electrolyte via a Luggin capillary tip placed close to the working electrode (WE). The WE were a glassy carbon (GC) of 5 mm diameter/ 4 mm diameter disk and a platinum wire was used as counter electrode. The electrochemical cell was filled with 0.1 M HClO₄ electrolyte.

The electrochemical measurements were carried out with a Metrohm Autolab potentiostat/galvanostat. Before each measurement, the resistance of the electrolyte was determined by electrochemical impedance spectroscopy (EIS) from 10 kHz to 1 Hz at open circuit potential (OCP). After that, a pre-treatment procedure was carried out, consisting of 50 voltammetric cycles (CV) under He/N₂ atmosphere, at a scan rate of 50 mV s^{-1} between 0.05 and 1.2 V vs. reversible hydrogen electrode (RHE); subsequently, five potential cycles, in the same potential range, were performed at a scan rate of 20 mV s^{-1} . By saturating the electrolyte with O₂, ORR activity was evaluated by means of linear sweep voltammetry (LSV) from 1.2 to 0.2 V vs. RHE, at a scan rate of 5 mV s^{-1} using a rotating disk electrode (RDE) at different rotations speeds (100, 200, 400, 1000, 1600, 2500 rpm).

Accelerated degradation tests (ADTs) were performed in He atmosphere cycling 1000 times the potential from 0.6 to 1.0 V vs. RHE at a scan rate of 50 mV s^{-1} . The loss of activity of catalysts for ORR was evaluated by LSVs before and after cycling, in an oxygen-saturated electrolyte.

In order to understand the reaction pathway of ORR, the electron transfer number per O₂ molecule was estimated by the above mentioned Koutecky–Levich (K-L) equation using as parameters $C(\text{O}_2)$, the saturated concentration of oxygen, $1.26 \cdot 10^{-3} \text{ M}$, $D(\text{O}_2)$, the diffusion coefficient of oxygen, $2.60 \cdot 10^{-5} \text{ cm}^2 \text{ s}^{-1}$ and ν , the kinematic viscosity of the

solution of $9 \cdot 10^{-3} \text{ cm}^2 \text{ s}^{-1}$. All these parameters are referred to the 0.1M HClO₄ solution, as reported in literature^[8].

3.3 RESULTS AND DISCUSSION

CALCIUM TITANATE PEROVSKITE CaTiO_{3-δ}

Figure 2 shows the voltammogram after 50 cycles (scan rate 20 mV sec⁻¹) for all the investigated catalysts. Because the specific activity depends on active sites, the electrochemically active surface area (ECSA) was evaluated and reported for each composite catalyst in Table 1. It was calculated by integrating the peak area of the H-adsorption process (from 0.4 to 0.05 V vs. RHE) in He-saturated environment. All CTO-added catalysts exhibit higher ECSA values than Pt/C, with the highest value (85 m² g⁻¹) for the Pt/C:CTO 1:2 composition.

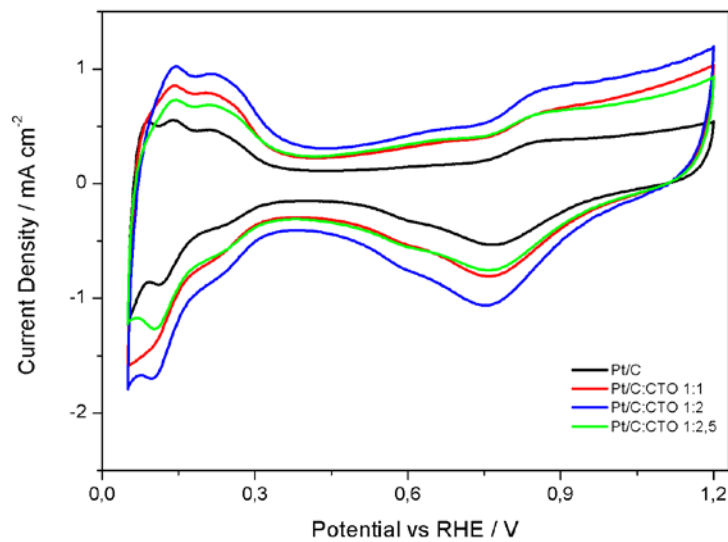


Figure 2: CVs profile of all catalysts under He

Samples	ECSA / m ² g ⁻¹
Pt/C	57
Pt/C:CTO 1:1	74
Pt/C:CTO 1:2	85
Pt/C:CTO 1:2,5	62

Table 1: ECSA values for each samples

Overall, the presence of the perovskite increases the active area of the catalyst, leading to a major availability of active sites. This could be due to a local coordination of CTO particles with platinum, enhancing its surface area.

It is demonstrated that the addition of transition metal oxides improves the electrocatalytic properties of the Pt-based catalysts towards different reactions, i.e. oxygen reduction, alcohol oxidation, etc., by increasing the interface and, thus, Pt utilization^[9,10]. Tian et al. also reported that titanium oxide played an important role in strengthening the interaction between metal particles and carbon support and inhibiting particles agglomeration during operation^[11].

It is noteworthy that also the presence of oxygen vacancies on the surface of CTO, play a key role as active catalyst sites leading to change the valence of metal cation and modifying the surface configuration. Indeed, as mentioned in^[12], to complete the oxygen coordination of the surface metal atoms, the metal cation participates to the redox reactions adsorbing on its surface oxygen species derived from aqueous electrolyte. Therefore, considering the follow equilibrium, where M is the metal cation site,



the presence of oxygen vacancies allows the interaction between the catalyst surface and water, providing additional protons and electrons with respect to platinum reaction products. Recently, previous reports have demonstrated how the oxygen vacancies render the electronic dense of states of surface oxide similar to that of platinum making the mechanism of O₂ adsorption comparable to that on Pt site^[13,14].

This could justify, even more, the highest ECSA obtained for composite electrodes.

However, the Pt/C:CTO 1:2.5 sample shows a lower ECSA value compared to the other composite electrodes, revealing that an excess of additive can hinder the Pt accessibility/utilization.

This aspect has been explained better by SEM images obtained for two composite ink, Pt/C:CTO 1:1 and Pt/C:CTO 1:2,5 where the presence of an excess of the perovskite seem to cause a leaching process of the materials leading to catalytic activity loss.

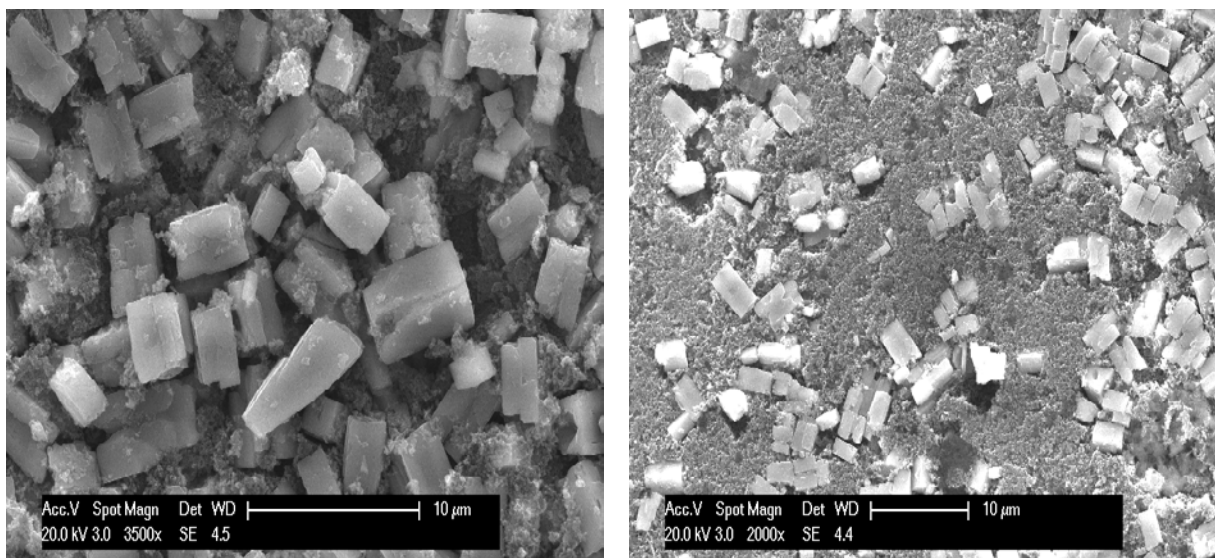


Figure 3: SEM images of Ink 20%Pt/C:CTO 1:1 (left) and Ink 20% Pt:CTO 1:2.5(right)

The Pt/C catalyst and two selected Pt:CTO composite formulations (Pt/C:CTO 1:1 and Pt/C:CTO 1:2) were electrochemically investigated for the evaluation of oxygen reduction reaction in O₂-saturated 0.1M HClO₄ by RDE experiments at different rotations per minute (rpm). In this thesis the comparison of the catalysis shown at 1600 rpm (Figure 4).

The current densities were normalized to the geometric surface area, 0.196 cm², of the GC electrode. The onset potential (E_{ons}) was calculated at -0.1 mA cm⁻² for each studied catalyst, whereas the half wave potential ($E_{1/2}$) corresponds to the potential value at one half of the diffusion/limiting current density. As reported in table 2, the Pt/C:CTO 1:2 catalyst shows the most positive E_{ons} (0.969 V) and $E_{1/2}$ (0.831 V), followed by Pt/C:CTO 1:1 with an E_{ons} of 0.960 V and an $E_{1/2}$ value of 0.815 V. On the other hand, the bare Pt/C exhibits the worst activity in terms of E_{ons} and $E_{1/2}$, respectively 20 mV and 30 mV more negative than the most active electro-catalyst.

Furthermore, Pt/C, without promoter, displays the lowest j_a , associated to mass transport constraints. Among the Pt/C:CTO 1:x composite formulations, a larger amount of promoter could be not beneficial in the diffusion region, where Pt/C:CTO 1:1 shows the largest j_a value (7 mA cm⁻²).

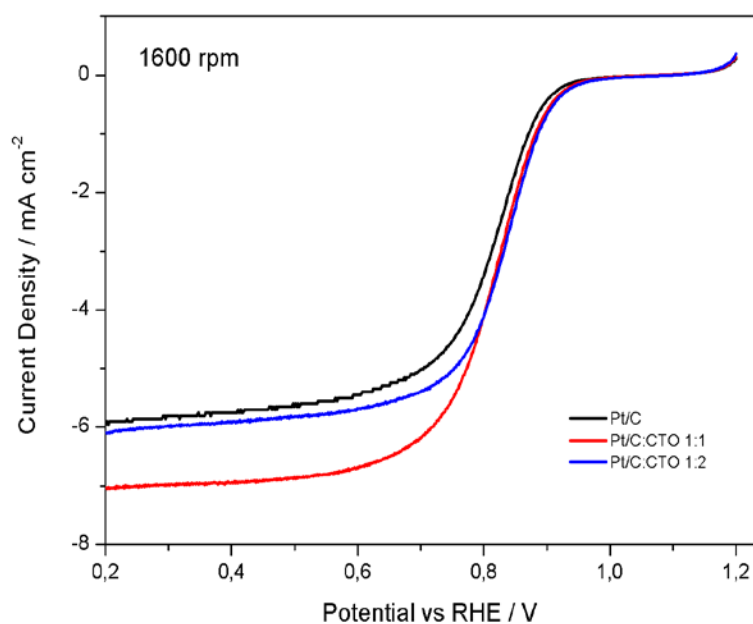


Figure 4: ORR polarization curves at 1600 rpm in O_2 -saturated 0.1 M $HClO_4$ at $5mVs^{-1}$

Samples	E_{onset} (V)	$E_{1/2}$ (V)
Pt/C	0,949	0,801
Pt/C:CTO 1:1	0,960	0,815
Pt/C:CTO 1:2	0,969	0,931

Table 2: The activity of different catalysts for ORR

As well known, the number of electrons transferred in the ORR process, corresponding to the direct formation of water, is 4, whereas a 2 electron pathway corresponds to the O_2/H_2O_2 redox couple. This number for Pt/C and for all the composite electrodes was calculated by the Koutecky–Levich equation (reported in the Section 2.3) in the diffusion-controlled region, at $E = 0.3$ V vs. RHE. At this potential, where a plateau region is reached, the hydrogen adsorption phenomenon is absent and the Pt catalyst exists in its pure form^[15]. Consequently, no kinetic limitations are expected and the ideal number of 4 electrons for bare Pt electrocatalyst should be obtained^[16].

As shown in Figure 5, the number of electrons exchanged during the oxygen reduction is 3.7 for Pt/C, 4.0 for Pt/C:CTO 1:1 and 3.4 for Pt/C:CTO 1:2. This highlights that the ORR predominantly proceeds via the four-electron pathway. A slightly lower electron transfer number may indicate that a small fraction of Pt active sites is less efficient towards the 4e- pathway. This occurs in the standalone Pt active sites and in the catalyst containing a high content of CTO (Pt/C:CTO 1:2).

Thus, a volcano-shaped relationship is envisaged with an optimum for the Pt/C:CTO 1:1 composition, emphasizing the important role of the right amount of perovskite as an additive and, most likely, as an active component in the oxygen reduction reaction.

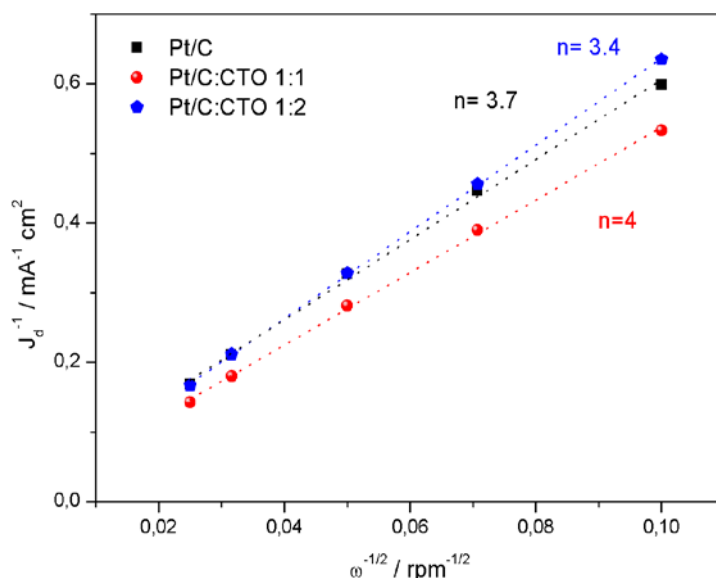


Figure 5: Koutecky-Levich plots of the ORR for Pt/C, Pt/C:CTO 1:1 and Pt/C:CTO 1:2

Accelerated degradation tests (ADTs)^[17] were carried out to study the behavior of the Pt/C:CTO 1:1 catalyst under stress and ageing conditions and to compare the electrochemical characteristics at the beginning of the test (BOT) and at the end of the test (EOT), in relation with the benchmark Pt/C. The two catalysts were subjected to 1000 cycles between 0.6 and 1.0 V vs RHE.

Table 3 shows the calculated ECSA for Pt/C and Pt/C:CTO 1:1, both samples show a negligible loss of activity in terms of ECSA, anyway less notice able for Pt/C:CTO 1:1 (5.4%) than for Pt/C (8.8%).

Samples	ECSA / m ² g ⁻¹	
	BOT	EOT
Pt/C	57	52
Pt/C:CTO 1:1	74	70

Table 3: The electrochemically active surface area (ECSA) of different pristine catalysts and at the end of accelerated degradation tests (EOT)

The effect of degradation test on Pt/C and Pt/C:CTO 1:1 was also investigated by the LSVs in O₂, reported in Figure 6. As expected, after the ADTs both materials show a shift towards more negative potential values and a decrease of the current density but such

losses appear less pronounced in the case of the composite Pt/C:CTO sample, with a final current density of -6.8 mA cm^{-2} .

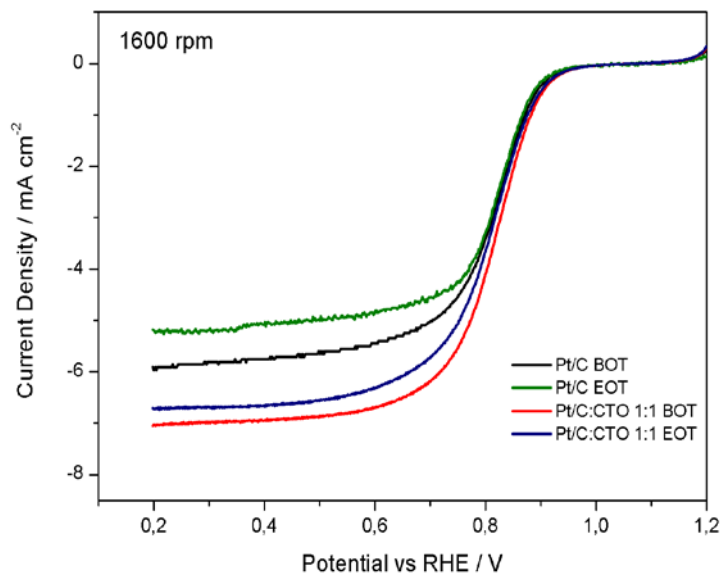
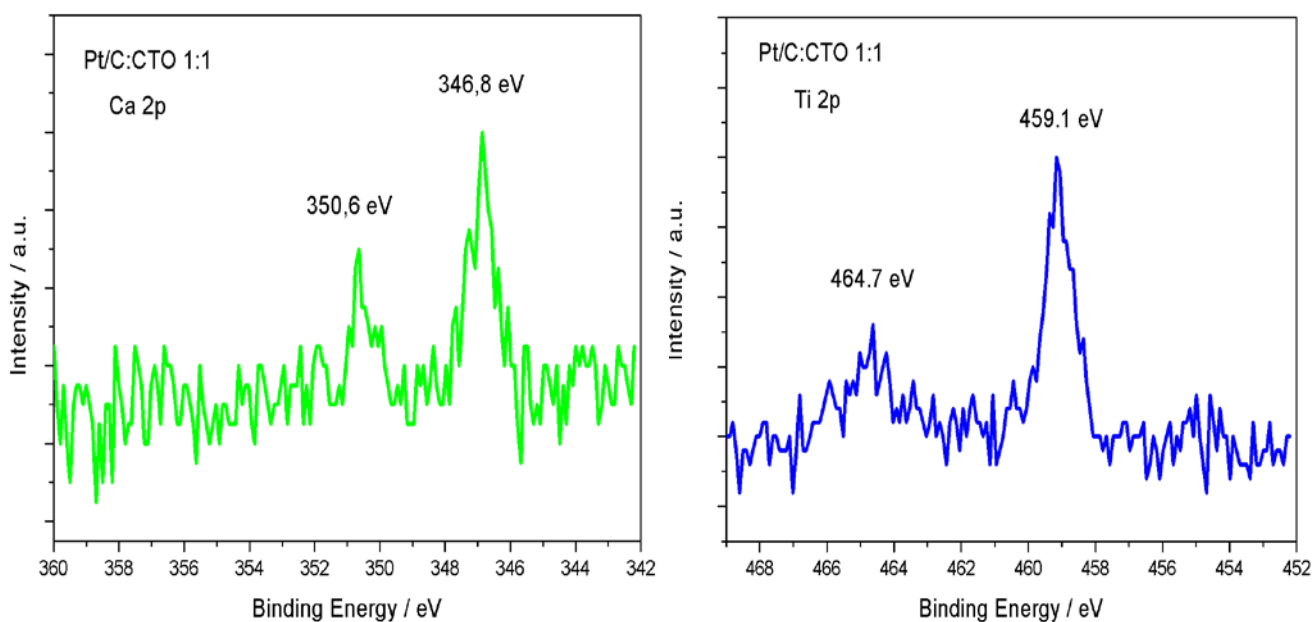


Figure 6: LSV curves at 1600 rpm recorded in O_2 -saturated solution before (BOT) and after (EOT) accelerated degradation tests. Scan rate: 5 mVs^{-1}

This could be explained, again, considering the perovskite as an active additive, with high corrosion resistance and stabilizing properties for the Pt catalysts, when it is in the same weight ratio with Pt.

The surface properties and oxidation states of the elements in the CTO compound have been investigated by XPS measurements performed on the most active catalyst composition Pt:CTO 1:1 and reported in figure 7.



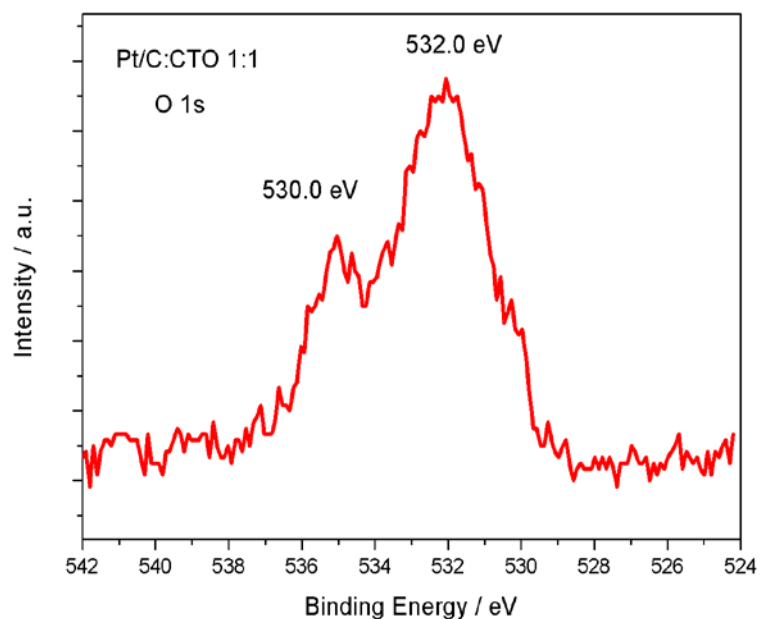


Figure 7: XPS spectra of Pt/C:CTO 1:1 sample for Ca 2p (a), Ti 2p (b) and O 1s (c). The large noise is due to very few amount of CTO in the analysed composite sample.

With respect to oxygen, both structural and chemisorbed oxygens are detected and the binding energy of O 1s is shifted from 529.8 in a Pt-free CTO sample (reported in chapter II) to 532.0 eV in our Pt/C/CTO sample, suggesting a stronger interaction/coordination of the perovskite metal oxide in the composite catalyst. The two main peaks observed for the transition metal are attributed to Ti 2p_{3/2} at 459.1 eV and to Ti 2p_{1/2} at 464.7 eV^[18] of the Ti⁴⁺ cationic structure.

Moreover, an additional small peak at 454.8 eV appears in the Pt/C:CTO spectrum, likely due to Ti²⁺, confirming the sub-stoichiometry of the perovskite here proposed.

A paper have been published on this work

Mazzapioda, L.; Lo Vecchio, C.; Paolone, A.; Aricò, A. S.; Baglio, V.; Navarra, M. A.; Enhancing Oxygen Reduction Reaction Catalytic Activity Using CaTiO_{3-δ} Additive, Chem.Electro.Chem, 6,5941, 2019

3.4 RESULTS AND DISCUSSION

IRON-DOPED CALCIUM TITANATE PEROVSKITE ($\text{CaTi}_{1-x}\text{Fe}_x\text{O}_{3-\delta}$)

Figure 8 shows the voltammogram after 50 cycles (scan rate 20 mV sec^{-1}) for all the catalysts. The electrochemically active surface area (ECSA) was evaluated by integrating the peak area of the H-adsorption process (from 0.4 to 0.05 V vs. RHE) in N_2 -saturated environment.

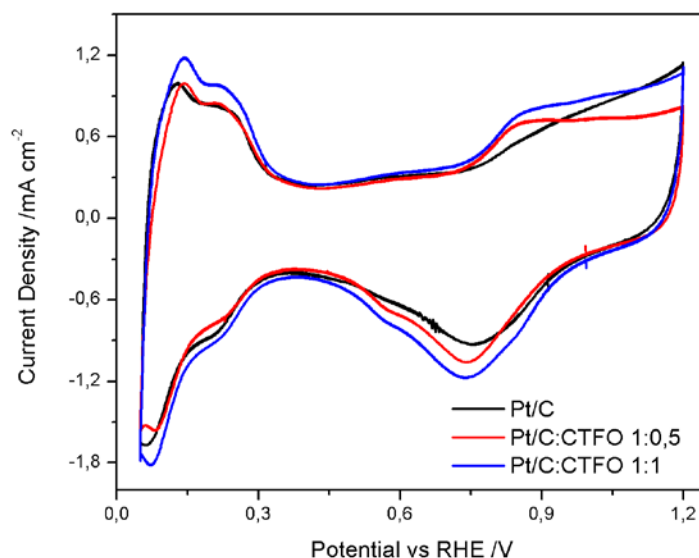


Figure 8: CVs profile of all catalysts under N_2

Among all the CTFO-added catalysts, Pt/C:CTFO 1:1 composition exhibits higher ECSA values ($80 \text{ m}^2 \text{ gr}^{-1}$) with respect to both Pt/C ($71 \text{ m}^2 \text{ gr}^{-1}$) and the other composite electrode Pt/C:CTO 1:0,5 ($65 \text{ m}^2 \text{ gr}^{-1}$).

This result could be justified considering both high electronic conductivity of CTFO support material and the presence of oxygen vacancies that can act as active site playing an important role in the electrochemical adsorption-desorption of oxygen species as explained in previous paragraph for CTO additive.

However, the Pt/C:CTFO 1:0,5 catalyst shows a lower ECSA value compared to the other composite electrode, revealing that a poor amount of additive could be not sufficient to optimize the Pt accessibility/utilization and consequently to improve the Pt/C catalytic activity.

The catalysts were electrochemically investigated for the evaluation of oxygen reduction reaction in O_2 -saturated 0.1M HClO_4 by RDE experiments at different rotations speed of the electrode. The comparison is shown at 1600 rpm (Figure 9a).

The current densities were normalized to the geometric surface area, 0.126 cm^2 , of the GC electrode.

As it can be visible in figure 9a, except for slight differences, the onset potential (E_{ons}) and the half wave potential ($E_{1/2}$) result of about 0,9 V and 0,82 V respectively for all samples.

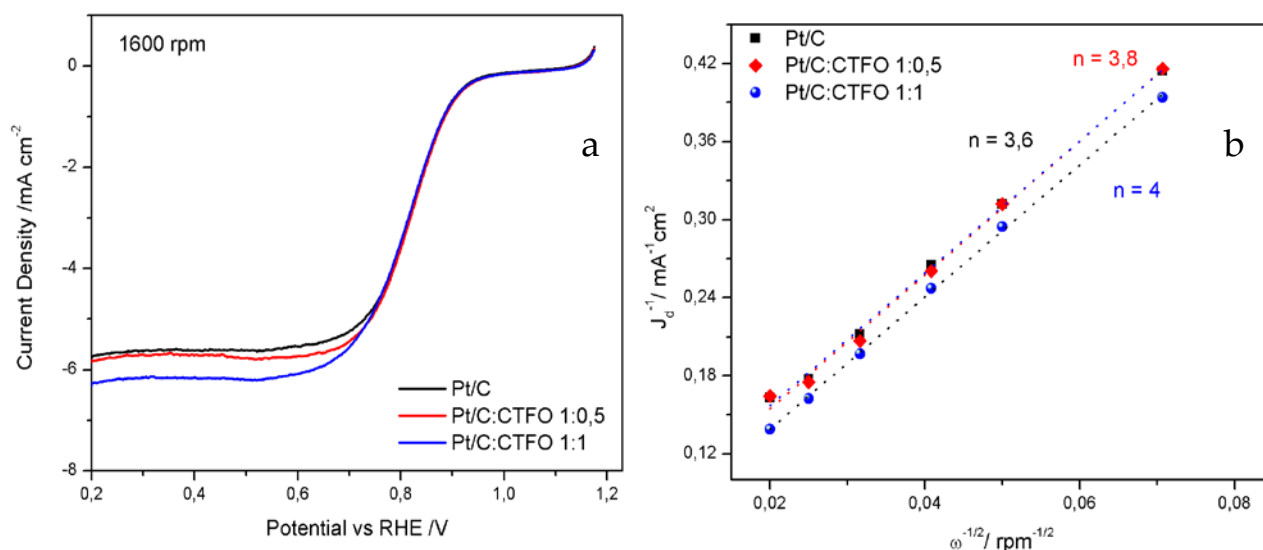


Figure 9: a) ORR polarization curves at 1600 rpm in O_2 -saturated 0.1 M $HClO_4$ at $5mVs^{-1}$
 b) Koutecky-Levich plots of the ORR for Pt/C, Pt/C:CTFO 1:0,5 and Pt/C:CTFO 1:1

However, the Pt/C:CTFO 1:1 catalyst displays the largest j_d value ($-6,3 \text{ mA cm}^{-2}$) associated to mass transport constraints with respect to the Pt/C sample. The other composite catalyst Pt/C:CTFO 1:0,5 exhibit a limiting current density comparable with Pt/C catalyst confirming that a lower amount of promoter could be not beneficial to obtain an improvement of Pt/C performance.

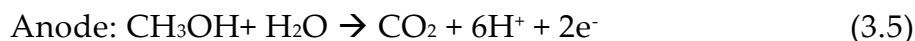
The number of electrons transferred in the ORR process, for all the electrodes was calculated by the Koutecky–Levich equation (reported in the paragraph 3.1) in the diffusion-controlled region, at $E = 0.3 \text{ V vs. RHE}$.

As shown in Figure 11 b, the number of electrons exchanged during the oxygen reduction is 3.6 for Pt/C, 3.8 for Pt/C:CTFO 1:0,5 and 4 for Pt/C:CTFO 1:1.

It is clear that Pt/C:CTFO 1:1 is the best catalyst for the ORR, whereas the other composite electrode present a close performance to Pt/C, as expected.

3.5 DIRECT METHANOL FUEL CELLS PERFORMANCES

A scheme of the overall reaction process occurring in a DMFC device with a proton conducting electrolyte is outlined below:



The most active catalyst for methanol electro-oxidation is a binary PtRu catalyst. The oxidation reaction of methanol on the Pt involves several adsorption steps giving rise to the formation of chemisorbed species including CO. CO_{ads} species can be catalyzed in the presence of oxygen-like or hydroxyl species adsorbed onto Ru sites acting as poisoning agent, consequently the anode electrocatalyst for DMFCs must to be CO tolerant^[19,20].

At the cathode side, as described in previous chapter and our reaction of interest, the oxygen reduction reaction, takes place.

In order to study the effective role of perovskite as additive of Pt for oxygen reduction reaction, a performance analysis of the most active composite electrode Pt/C:CTO 1:1 was carried out in a direct methanol fuel cell configuration and it was compared with a Pt/C cathode based MEA.

Both electrodes were manufactured using commercial gas-diffusion layer-coated carbon cloths HT-ELAT and LT-ELAT (from E-TEK) as backing layers at the anode and cathode, respectively. The catalytic ink was prepared according to the procedure described in a previous report^[21].

For the anode a commercial 60% PtRu/C was dispersed in water, sonicated with 33 wt% Nafion® ionomer (Ion Power, 5 wt% solution) and deposited by a doctor blade technique onto the backing layer. A Pt loading of $2 \pm 0.1 \text{ mg}\cdot\text{cm}^{-2}$ was used at the anode.

For the cathode, a commercial 20% Pt/C (from E-TEK) catalyst was prepared by the same technique used for the anode, mixing the powder with 33 wt% Nafion® ionomer (Ion Power, 5 wt% solution) under sonication and deposited by a doctor blade technique onto the backing layer. In the case of composite electrode, the perovskite CTO was added in the same ratio of Pt before the sonication procedure. A Pt loading of $0,6 \pm 0.2 \text{ mg}\cdot\text{cm}^{-2}$ was used at the cathode.

The MEAs were obtained by hot pressing the electrodes onto both sides of a Nafion® 115 membrane at 130 °C and $20 \text{ kgf}\cdot\text{cm}^{-2}$ for 1.5 min. The MEAs were tested in a 5 cm² single cell hardware connected to a Fuel Cell Technologies Inc. station. A methanol concentrations of 2M was fed to the anode with a flow rate of $2 \text{ mL}\cdot\text{min}^{-1}$, whereas fully humidified oxygen was fed to the cathode at a flow rate of $100 \text{ mL}\cdot\text{min}^{-1}$ under atmospheric pressure.

The performance of each MEA was measured at three different temperatures, 30, 60 and 90 °C.

3.5.1. RESULTS AND DISCUSSION

DMFC polarization and power density curves obtained at three different temperatures (30, 60 and 90°C) and at 2M methanol concentration are shown in Figure 8.

We can observe that the all cell performances, in term of current and power densities achieved, are better for all Pt/C:CTO 1:1 cathode based MEA with respect to a Pt/C MEA. Especially, the maximum power density increases with temperature reaching a maximum value of about 120 mWcm⁻² at 90°C.

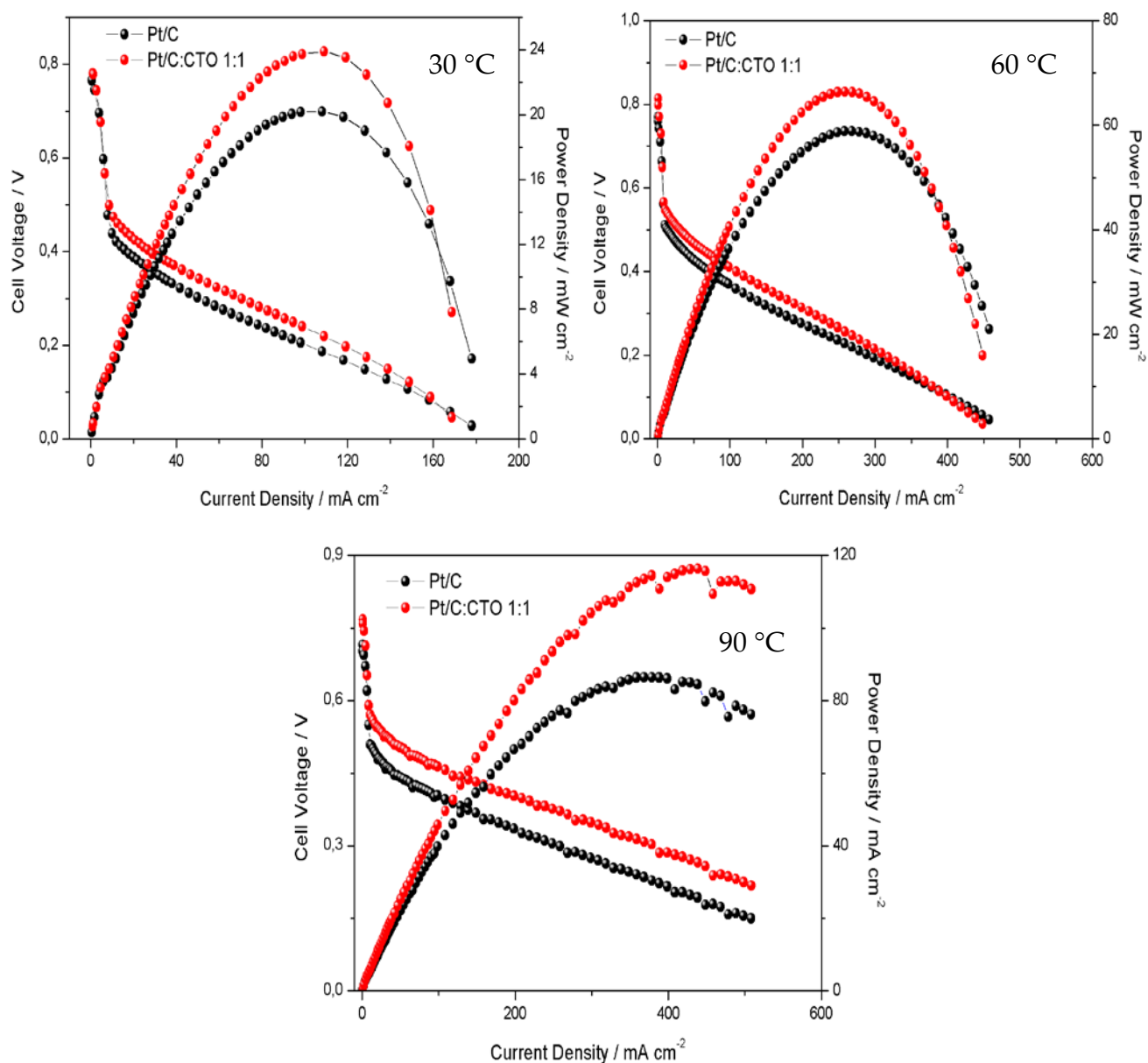


Figure 10: Polarization and power densities curves obtained at increasing temperature (30°, 60°,90°C) in a methanol/air single fuel cell.

As well known increasing operating temperature leads to increase both redox reaction rates explaining the best performances obtained at high temperatures. Furthermore, the 2M methanol concentration allows to have an improvement of methanol transfer at the anode side reducing the mass transport constraints with respect to lower concentrations^[22].

However, at these conditions also the methanol crossover rate is improved. Consequently, in the polarization curves, it is remarkable that the open circuit voltage (OCV) which is directly related to the methanol tolerance properties of the cathode, decrease by increasing temperature as reported in Figure 9.

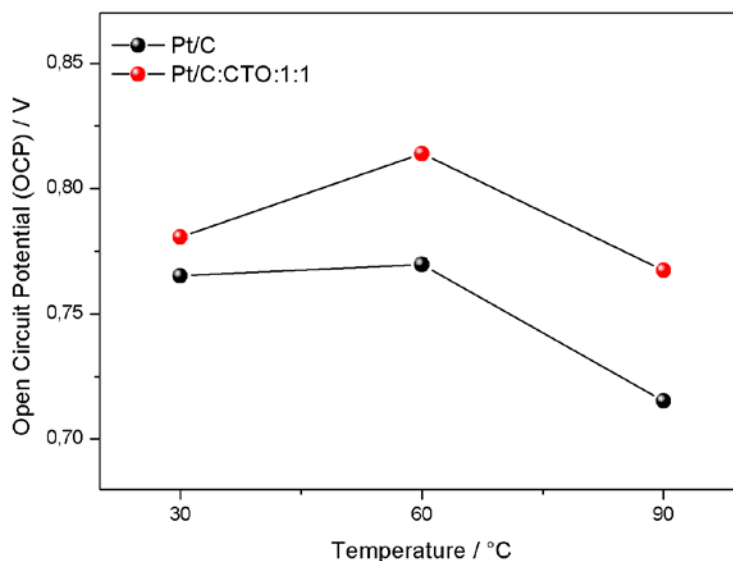


Figure 11: *Open circuit voltage obtained at increasing temperature (30°, 60°,90°C)*

The methanol adsorption on the cathode influences the region of activation control for oxygen reduction. In fact, at high cathode potentials, oxygen reduction is slow and the oxidation of methanol permeated through the membrane is enhanced by the elevated potential. The two opposite reactions compete with each other and no spontaneous current is registered above 0.9V.

Generally, Pt-cathode-based MEA shows a precisely decrease in performance when feeding with high methanol concentrations^[23], whereby the crossover effect at the cathode is not compensated by the better performance of the anode. It was deduced that this condition occurs because of the adsorption of the alcohol on the Pt active sites negatively affects the selectivity toward ORR.

It is evident that in the case of the composed MEA, the presence of $\text{CaTiO}_{3-\delta}$ perovskite seems to improve the selectivity of Pt towards to ORR improving the overall cell performance and confirming the positive results obtained by RDE measurements.

3.6 CONCLUSIONS

A non-stoichiometric Calcium Titanate ($\text{CaTiO}_{3-\delta}$) perovskite was used as an additive of Pt for oxygen reduction reaction in acidic media. Three composite catalysts were prepared, with different amount of perovskite, Pt/C:CTO 1:1, Pt/C: CTO 1:2 and Pt/C:CTO 1:2.5. A commercial Pt/C catalyst was used as reference.

RDE measurements, used to study oxygen reduction reaction, have revealed that the catalyst Pt/C:CTO 1:1 posses the best activity, presenting a 4 e-reduction pathway and delivering an higher limiting current density than the other samples.

This could be explained considering the perovskite as an active additive that thank to the presence of oxygen vacancies allows the interaction between the catalyst surface and water, providing additional protons and electrons with respect to platinum reaction products. Furthermore, from both electrochemical analysis and SEM images it is clear that too high dose of additive can be detrimental for Pt/C catalyst properties.

Consequently when Pt is in the same weight ratio with the perovskite we have obtained the best composition for the composite catalysts.

The stability of the Pt/C:CTO 1:1 composite catalyst was studied and compared to the bare Pt/C catalyst by accelerated degradation tests. The catalyst Pt/C:CTO 1:1 showed an excellent electrochemical stability, associated to high corrosion resistance compared to the benchmark Pt/C.

A performance analysis of the most active composite electrode Pt/C:CTO 1:1 was carried out in a direct methanol fuel cell configuration and it was compared with a Pt/C cathode based MEA. Fuel Cell performances were generally positively affected by the presence of the perovskite. In particular, the use of the $\text{CaTiO}_{3-\delta}$ allows to work in more drastic conditions, i.e. high methanol concentration and higher temperature with respect to Pt/C cathode based MEA.

Overall, the adoption of this very convenient material (i.e., a low cost perovskite $\text{CaTiO}_{3-\delta}$) seems to mitigate the major problems concerning Pt stability and, in turn, to enhance the catalyst activity.

A iron-doped calcium titanate perovskite ($\text{CaTi}_{1-x}\text{Fe}_x\text{O}_{3-\delta}$, CTFO) was synthesized by High Energy Ball Milling, using stoichiometric amounts of CaCO_3 , TiO_2 and $\text{FeO}(\text{OH})$ and used as an additive of Pt for oxygen reduction reaction in acidic media. Two composite catalysts were prepared, Pt/C:CTFO 1:0,5 and Pt/C:CTFO 1:1 and compared with a commercial Pt/C catalyst used as reference. RDE measurements, have shown that the catalyst Pt/C:CTFO 1:1 posses the best activity toward the ORR presenting a 4 e-reduction pathway and exhibiting the most high limiting current density than the other samples.

It is clear that the right amount of this perovskite can alter the ORR mechanism from 2e- pathway to a 4e- pathway, in fact a poor amount of additive seem to be not sufficient to improve the Pt/C catalytic activity.

By this preliminary studies in term of chemical-physical and electrochemical characterization about CTFO perovskite, we have demonstrated that this iron-doped perovskite has promising features to be used as cathode catalyst support for low temperature fuel cells.

REFERENCES

- [1] Alegre C, Modica E, Aricò A.S, Baglio V, J. Electroanal. Chem. 808 412, **2018**
- [2] Du C, Tana Q, Yina G, Zhang J, *Rotating Electrode Methods and Oxygen Reduction Electrocatalysts*, ISBN 978-0-444-63278-4, Elsevier, **2014**
- [3] Baglio V, Sebastian D, *Catalyst*,7,370, **2017**
- [4] Wang J, *Analytical Electrochemistry Third Edition* **2006**
- [5] Sebastian D, Stassi A, Siracusano S, Lo Vecchio C, Aricò A.S, Baglio V, J. Electrochem Soc., 162, 7, F713, **2015**
- [6] Renzi M, D'Angelo G, Marassi R, Nobili F, J. Power Sources, 327,11, **2016**
- [7] Renzi M, Mignini P, Giuli G, Marassi R, Nobili F, Int. J. Hydrog. Energy 41,11163, **2016**
- [8] Brocato S, Serov A, Atanassov P, *Electrochim. Acta*, 87, 361, **2013**
- [9] Baglio V, Zignani S.C, Siracusano S, Stassi A, D'Urso C, Aricò A. S, *Electrocatalysis*, 4 , 235, **2013**
- [10] L. Yu, J. Xi, *Electrochim. Acta*, 67, 166, **2012**
- [11] J. Tian, G. Sun, L. Jiang, S. Yan, Q. Mao, Q. Xin, *Electrochem. Commun.*, 9 , 563, **2007**
- [12] Linh N. H, Nguyen T. Q, Diño W. A, Kasai H, *Surf. Sci*, 633 , 38, **2015**
- [13] Fujii K, Sato Y, Takase S, Shimizu Y, J. Electrochem Soc., 162 , F129, **2015**
- [14] Imai H, Matsumoto M, Miyazaki T, Fujieda S, Ishihara A, Tamura M, Ota K.I, *Appl. Phys. Lett.*, 96 , 191905, **2010**
- [15] Ornelas R, Stassi A, Modica E, Aricò A. S, Antonucci V, *ECS Trans.*,3,633, **2006**
- [16] Wlodarczyk R et al. *J. Power Source*, 159,802, **2006**
- [17] Zacevic S.K et al. L. *Electrochem. Soc.*, 144, 2973, **1997**
- [18] Yan Y, Yang H, Yi Z, Li R, Wang X, *Micromachines*, 10, 254, **2019**
- [19] Gasteiger H.A, Markovic N, Ross P.N, Cairns E.J, *J. Phys.Chem.*, 97,12020, **1993**
- [20] Long J.W, Stroud R.M, Swider-Lyons K.E, Rolison D.R, *J. Phys.Chem.*, B 104, 9772, **2000**
- [21] Baglio V, Stassi A, Matera F.V, Di Blasi A, Antonucci V, Aricò A.S, *J. Power Sources* 180,797, **2008**
- [22] Sebastián D, Serov A, Artyushkova K, Gordon J, Atanassov P, Aricò A.S, Baglio V, *ChemSusChem*, 9, 1, **2016**
- [23] Lo Vecchio C, Sebastián D, Alegre C, Aricò A.S, Baglio V, J. Electroanal. Chem, 808, 464, **2018**

CHAPTER IV

CALCIUM TITANATE $\text{CaTiO}_{3-\delta}$ PEROVSKITE USED AS ADDITIVE FOR NAFION MEMBRANES

4.1 INTRODUCTION

As mentioned in chapter II, the presence of oxygen vacancies can play a key role as active sites for the dissociative absorption of water for which the protons conductivity is favored. This aspect could be also used to improve the hydrophilicity of the oxide by the protonation of the lattice oxygen ions.

Furthermore, a distortion of the crystal lattice can influence the energetic properties of the oxygen ions in term of different binding energies to protons^[1]. Consequently, local structural and chemical perturbations induce water trapping effects, lattice relaxations around oxygen ion vacancies etc. which can affect significantly the proton mobility and conductivity.

According to Kreuer^[2] water from the atmosphere dissociates into hydroxide ions and protons; the hydroxide ion fills the oxygen vacancy, and the proton forms a covalent bond with the lattice oxygen. This process can be written with the following equations in Kröger-Vink notation:



where $\text{V}_{\text{O}}^{\bullet\bullet}$ represent the oxygen vacancy, $\text{O}_{\text{O}}^{\times}$ is the oxygen in a regular crystal lattice site, OH^{\bullet} is the protonic defect, h^{\bullet} is an electronic hole. Considering the formation of protonic defects as an amphoteric reaction, the oxide material can simultaneously acts as an acid (absorption of hydroxide ion by oxygen ion vacancy) and as a base (protonation of lattice oxygen ions)^[3].

The protonation of the lattice oxygen ions seems to dominate in perovskite-type oxides due to the low formation enthalpies of oxygen ions as a result of low bond strengths and strong relaxation effects^[4]. The proton migration pathways are most characterized by lower activation barriers within solid oxides as compared to oxygen ions because of their smaller mass, lower radius and absence of electron cloud.

In a crystal lattice, protons are located close to their crystallographic position because of electrostatic attraction and can rotate and migrate between adjacent anions through the so-called Grotthuss mechanism^[5], which is the basis of proton conduction in Nafion membranes.

In this work, with the aim to obtain a synergetic effect between the capability of a nonstoichiometric perovskite to promote the proton migration and the well known Nafion membrane proton conductivity, we report the synthesis and chemical-physical characterization of two composite Nafion membranes considered, as a valid alternative to the existing electrolyte system.

4.2 MEMBRANE SYNTHESIS

A solvent casting procedure has been used to prepare both doped- and undoped-Nafion membranes, according to an internal established procedure^[6,7,8].

Solvents of a commercial Nafion 5 wt.% dispersion (E.W. 1100, Ion Power Inc, München Germany) were gradually replaced with N,N-dimethylacetamide (> 99.5%, Sigma Aldrich, St. Louis, MO, USA) at 80 °C. For the composite membranes, two filler concentrations of 5 wt% and 10 wt % of the CaTiO_{3-δ} additive, with respect to the dry Nafion content, were chosen and added to the final Nafion solution. The mixture obtained was casted on a Petri dish and dried at 80°C. In order to improve the thermal stability and robustness of the membranes, dry membranes were extracted and hot-pressed at 50 atm, 175 °C for 15 min. The membranes were activated and purified in boiling 3 wt.% hydrogen peroxide (H₂O₂, 34.5%-36.5%, Sigma Aldrich, St. Louis, MO, USA), H₂SO₄ (0.5 M) and distilled water. Composite membranes were compared to plain Nafion systems prepared with the same procedure. All samples were stored in bi-distilled water. Membranes containing 5 and 10 wt.% of the inorganic filler will be labeled in the text as M5 and M10, respectively, while the un-doped membrane will be referred as N.

Membrane's thickness was measured in dry state, after hot pressing procedure, resulting in the range of 90-110 μm as reported in table 1. All samples were stored in bi-distilled water.

Samples	CaTiO _{3-δ} (w/w %)	Thickness (μm)
M0	-	90±5
M5	5	98±6
M10	10	110±5

Table 1: *Composition and thickness of the investigated membranes*

4.2.1 PHYSICAL-CHEMICAL CHARACTERIZATIONS

The mechanical properties of the membranes were measured by means of a Perkin Elmer DMA 8000 in the so-called "tension configuration" on small membrane pieces 4-6 mm wide, 10-12 mm long and 0.10-0.15 mm thick^[9].

The samples were cut from the various membranes dried in oven at 70°C (dry samples) or immersed in bi-distilled water at room temperature (wet samples). In this latter case, to prevent the release of water, the samples were very quickly mounted onto the DMA apparatus and measured. The storage modulus, M , and the elastic energy dissipation, $\tan\delta$, were measured at 1 and 10 Hz, as a function of temperature between 20 and 190 °C, with a scan rate of 4° C/min.

Thermal analysis were conducted by means of differential scanning calorimetry (DSC) using DSC821 Mettler-Toledo instrument and by thermal gravimetric (TG) analysis performed with a TGA/SDTA851 Mettler-Toledo instrument. For both the techniques, membrane samples were kept at 100 % relative humidity (RH) for two weeks prior measurements.

DSC measurements were obtained under N₂ flux at 20 °C/min scan rate while TG analysis were carried out in air at 20 °C/min. Thermal gravimetric (TG) analysis was performed under air (80 ml/min) in a temperature range between 25 °C and 550 °C. Prior to measurements, the samples were dried at 80°C under vacuum overnight.

The ion-exchange capacity (IEC), which expresses the number of milli-equivalents of exchangeable protons, was evaluated by a titration method either for the powder that for all the membranes. Dry samples were immersed in NaCl aqueous solution and the exchanged protons were neutralized with a standard solution of NaOH (0.1 M)^[10].

For all the membranes the total water uptake (WU) was evaluated at room temperature by a gravimetric method in according to the following equation:

$$W.U. = \frac{W_{\text{wet}} - W_{\text{dry}}}{W_{\text{dry}}} * 100$$

Where W_{wet} was the weight of fully hydrated membranes and W_{dry} was the weight of dried membranes measured after a night at 80 °C under vacuum. Humidified membranes were obtained by equilibrating the samples in a close container in presence of water for two weeks. For both W.U. and IEC values, errors were evaluated with standard deviation of three different measurements.

Hydration number known as λ , is a parameter that allows to define the number of water molecules for each sulfuric acid group. It was calculated, respect to W.U. obtained at 100% RH, by the following equation^[11]:

$$\lambda = \frac{\text{mol H}_2\text{O}}{\text{mol acid groups}} = \frac{W.U.}{IEC} * \frac{10}{18}$$

Vibrational spectroscopy studies are carried out by Attenuated Total Reflectance - Fourier Transform Infrared spectroscopy (ATR-FTIR) and Raman spectroscopy, to examine the structure of all membranes.

Raman spectra were collected with an InVia Reflex spectrometer from Renishaw. Depending on the sample, 5 or 10% of the nominal power (i.e., 300 mW) of a 785 nm diode laser was used. The spectrometer was calibrated using the 520.6 cm⁻¹ line of a silicon wafer. The analysis of the spectra was performed using the WIRE 5.0 software.

Attenuated Total Reflectance-Fourier Transform Infrared spectroscopy (ATR-FTIR), spectra were collected with a PerkinElmer 2000 FT-IR spectrometer in the attenuated total

reflection mode using a ZnSe crystal. The spectral resolution was 1 cm^{-1} , and 64 scans were recorded for each sample at ambient temperature.

Small-angle X-ray scattering combined with Wide-angle X-ray scattering (SAXS-MAXS) measurement have been used to understand the interactions between the filler and the Nafion matrix after hydration. Also in this case, the humidified membranes were obtained by equilibrating the samples in a close container in presence of water for 8 days.

These measurements were carried out using a Mat:Nordic fully automated instrument from SAXSLAB/Xenocs. The X-ray beam produced by Cu-irradiation impinged into a sample with the help of a microfocused sealed tube X-ray generator, that is, a MicroMax 003 from Rigaku. A Pilatus 300 K detector from Dectris was used to collect the spectra. By changing the sample-to-detector distance, the scattering vector (q) was varied in the range $0.003\text{--}0.4\text{ \AA}^{-1}$. The membranes were inserted into a sandwich-type holder between two mica windows. The correlation distance (d) related to the scattering objects was calculated from the Bragg's equation $d = 2\pi/q$, where q is the center of a scattering peak.

Dielectric measurements were performed with a NovocontrolGmbH broadband dielectric spectrometer, equipped with a Quatro Cryosystem temperature control unit. The membranes were placed between two carbon electrodes and then between two gold plated electrodes (diameter of 10 mm) under humidity condition (i.e. we kept a water reservoir under the bottom electrode). The spectra were measured in the frequency range from (10^{-1} to 10^7 Hz) and at different temperature ($20\text{ }^\circ\text{C}\rightarrow 80\text{ }^\circ\text{C}\rightarrow 110\text{ }^\circ\text{C}\rightarrow 80\text{ }^\circ\text{C}\rightarrow 20\text{ }^\circ\text{C}$).

Through a high resolution field emission scanning electron microscopy (HR-FESEM) analysis, performed by an Auriga Zeiss instrument at the CNIS research centre of Sapienza University of Rome, the morphology of the Nafion membranes were evaluated.

Methanol crossover measurements were carried out electrochemically by linear sweep voltammetry (LSV) mode in the voltage range from 0 to 0.9 V, with a scan rate of 2 mV s^{-1} . 2 M MeOH solution (3 ml min^{-1}) was fed to one side of the cell used as Counter/Reference Electrode, and N_2 (100 ml min^{-1}) was supplied to the other compartment (Working Electrode). Methanol crossing the membrane is oxidized at the working electrode generating a positive current, which reaches a plateau when all methanol is converted to CO_2 under steady state conditions^[12,13].

For the DMFC investigation, the electrodes were manufactured using commercial gas-diffusion layer-coated carbon cloths HT-ELAT and LTELAT (from E-TEK) as backing layers at the anode and cathode, respectively. The catalytic ink was prepared according to the procedure described in a previous report^[14]. For the cathode, 20% Pt/C (from E-TEK), were dispersed in water, sonicated with 33 wt% Nafion® ionomer (Ion Power, 5 wt% solution) and deposited by a doctor blade technique onto the backing layer. A Pt loading of $0.6 \pm 0.1\text{ mg}\cdot\text{cm}^{-2}$ was used at the cathode of both electrodes. For the anode, 60% Pt-Ru/C (from Alfa Aesar) catalyst was mixed with 33 wt% Nafion® ionomer (Ion Power, 5 wt% solution) under sonication and deposited by a doctor blade technique onto the

backing layer. A Pt loading of $1.2 \pm 0.1 \text{ mg}\cdot\text{cm}^{-2}$ was used at the anode in the two membrane-electrode assemblies (MEAs). The MEAs were obtained by hot pressing the electrodes onto both sides of all Nafion membranes (N, M5, M10) at $130 \text{ }^\circ\text{C}$ and $20 \text{ kgf}\cdot\text{cm}^{-2}$ for 1.5 min.

The MEAs were tested in a 5 cm^2 single cell hardware connected to a Fuel Cell Technologies Inc. station. Different methanol concentrations (2 M) were fed to the anode with a flow rate of $2 \text{ mL}\cdot\text{min}^{-1}$, whereas fully humidified oxygen was fed to the cathode at a flow rate of $100 \text{ mL}\cdot\text{min}^{-1}$ under atmospheric pressure. The performance of each MEA was measured under steady state conditions in the temperature range $30\text{--}110 \text{ }^\circ\text{C}$.

4.3 RESULTS AND DISCUSSION

Composite membranes were evaluated in term of Water Uptake (W.U.) and Ion Exchange Capacity (IEC). These are important parameters because they provide a direct measure of the hydration level and of the number of available protons. Based on these parameters it is possible to derive the value of λ .

Nafion polymer, used for this project, has an equivalent weight of 1100 geq^{-1} and, thus, its theoretical IEC value is $9 \times 10^{-4} \text{ eqg}^{-1}$. The ion exchange capacity obtained experimentally for the Nafion sample approaches this theoretical value.

Generally, when the inorganic particles are added to Nafion, there is a significant decrease of the IEC related to an increase of density in the membrane because of the interaction of the additive with the polymer. This leads to have a lower availability of exchangeable protons. In this case for both composite membranes the IEC values doesn't decrease dramatically compared to Nafion value obtained.

With respect to λ and W.U., all the composite membranes have presented comparable values. (table 1)

Acronimo	IEC meq gr^{-1}	W.U. %	$\lambda (\text{H}_2\text{O}/\text{SO}_4^{2-})$
N	$0,83 \pm 0,1$	18,9	12,7
M5	$0,80 \pm 0,03$	18,1	12,6
M10	$0,79 \pm 0,04$	17,4	12,2

Table 2: WU, IEC and λ of the membranes at 100 % RH

Figure 1 shows the scattering intensity $I(q)$ obtained by SAXS-WAXS measurements, for the all membranes under investigation at both dry and humidified conditions.

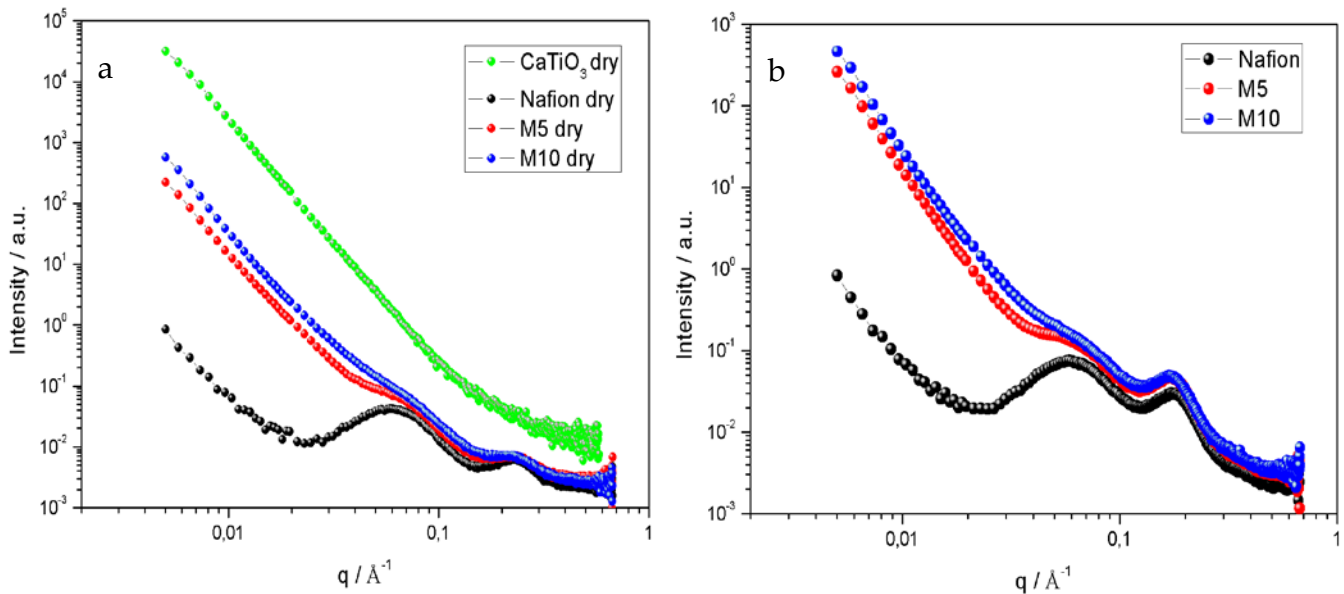


Figure 1: SAXS and WAXS patterns of all Nafion membranes under investigation under dry state (a) and under humidified conditions (b)

In picture 1a, the perovskite calcium titanate profile in dry condition is shown for comparative purpose and to justify the biggest slope obtained at higher q values for the composite Nafion membranes with respect to undoped Nafion due to the presence of the additive. Anyway, from these plots, two main peaks are visible which give information on the shape and size of the scattering components in Nafion membranes.

In particular, the first peak, the so-called Matrix Knee peak, correspond to the fluorocarbon polymer crystallites randomly distributed in the amorphous polymer matrix; it is observed in the higher q range and its intensity depends on the degree of crystallinity of the polymer^[15].

The second peak, the so-called ionomer peak, typically observed in the q range $0.1\text{--}0.3\text{\AA}^{-1}$ is due to the local ordering of the ionic domains within the Nafion polymer^[16].

From the position and intensity of the ionomer peak, it is possible obtain informations about the hydration degree of the Nafion sample because it is related to water channel periodicity within the membrane clusters.

As a note, the Nafion membrane structure is described as rodlike ionic domains that expand radially after hydration, this model is considered more appropriate for its description than the Gierke's clustering model, where spherical ionic hydrated clusters are connected by channels with a diameter of 1 nm (see chapter I).

In order to evaluate the hydration state of all Nafion membranes, the correlation distance (d), related to the scattering objects, was calculated from the Bragg's equation

$$d = 2\pi/q, \text{ where } q \text{ is the center of the ionomer scattering peak.}$$

In table 3 the d and q values for all samples at both investigated conditions are reported.

Samples	$q / \text{\AA}^{-1}$	$d / \text{\AA}$	Samples	$q / \text{\AA}^{-1}$	$d / \text{\AA}$
Nafion	0,232	27,07	N	0,197	35,28
M5	0,233	26,95	M5	0,175	35,88
M10	0,232	27,07	M10	0,166	37,83

Table 3: q and d values of all Nafion membranes at dry state (on the left) and at humidified conditions (on the right)

As it can be clearly seen from table 2, all Nafion undoped and doped membranes have the peak at the same position and the d values are comparable for each samples at dry condition. However, when the membranes are subjected at hydration, the position of q ionomer peak shifts to lower q values especially for the two composite membranes with respect to Nafion.

This gives an estimation of the increased size of the ionic domain as result of the water content. Among all, M10 membrane shows the highest d value compared to the others samples indicating a better hydration leve confuting the W.U. values obtained.

Figure 2 shows the FTIR spectra of a Nafion membrane in dry state and of the CTO perovskite.

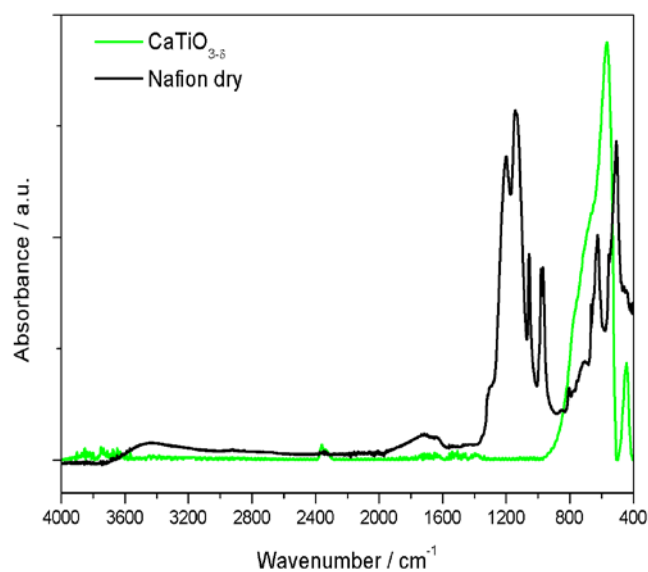


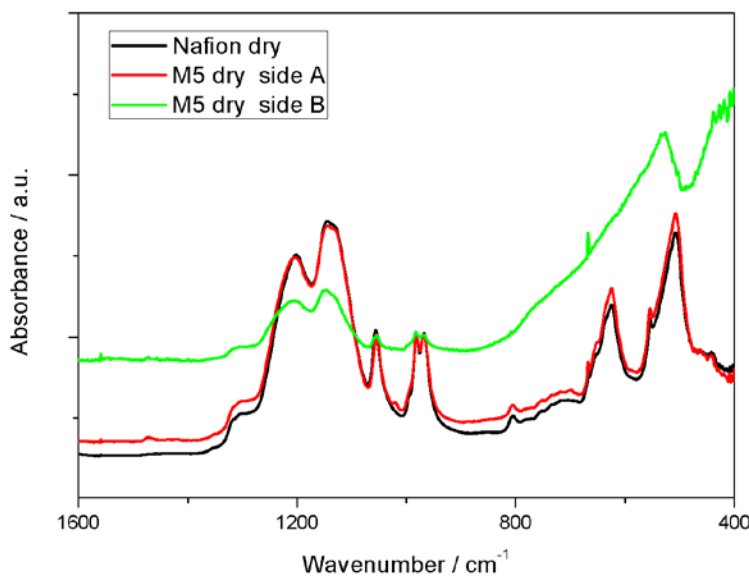
Figure 2: Infrared spectra of both Nafion membrane and CTO powder

The FTIR spectra reveals the vibrational modes associated to: i) the hydrophobic fluorocarbon chains of Nafion (1300–1000 cm^{-1}); ii) the perfluoroetheral side chains of Nafion (1000–940 cm^{-1}) and iii) the stretching vibration Ti-O and bridging stretching modes of Ti-O-Ti of the inorganic component (430–560 cm^{-1}). In detail the all assignament for Nafion bands are reported in table 4^[17].

However, the peaks related to the additive are overlapping with Nafion peaks at low wavenumber.

The spectra of Nafion membrane exhibit a broad band at ca. 1500 cm^{-1} and ca. 3600 cm^{-1} related to the bending modes of water still presents in the membrane even though the drying treatment at 80°C prior to measurement.

It is worth noticing that, for the composite membrane, the IR spectra can change in relation to the side of the membrane analyzed. As shown in the picture 3 about M5 spectra (the other M10 composite membrane has shown the same behavior), the peaks related to the perovskite result more visible if the side A, is analyzed with respect to the other one (side B) where the Nafion peaks are more clear.



Frequency / cm^{-1}	Assignment ^[17]
1300 cm^{-1}	ν_s (C-C)
1206 cm^{-1}	ν_{as} (CF ₂)
1142 cm^{-1}	ν_s (CF ₂)
1059 cm^{-1}	ν_s (SO ₃ ⁻)
982 cm^{-1}	ν_s (C-O-C)
969 cm^{-1}	ν_s (C-O-C)

Figure 3: FTIR Spectra of Nafion membrane and M5 membrane at dry state (on the left)

Table 4: Assignement of major IR bands of Nafion (on the right)

The ν_s (SO₃⁻) band at 1059 cm^{-1} was chosen for the intensity normalization of all IR spectra.

In according with the literature, the filler, during the solvent casting process, developpe an concentration profile^[18] making the Nafion membrane not uniform in term of additive dispersion especially in the surface region. The presence of two different sides in Nafion membrane was particarly stressed by a mapping Raman spectroscopy, used to analyze the cross section of M5 sample.

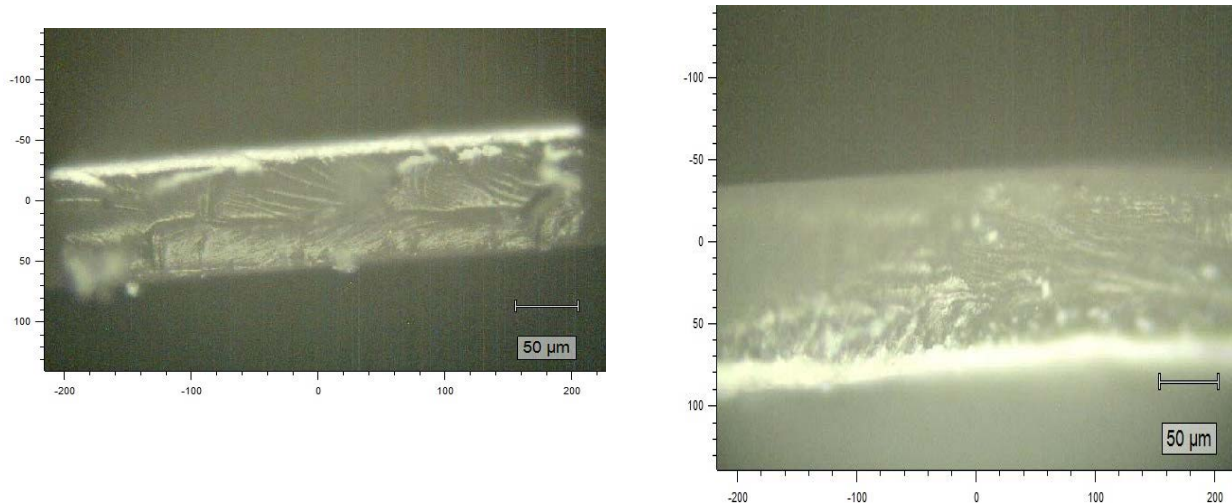


Figure 4: Raman images of a M5 membrane sample recorded from two different directions: top-view (on the left) and side-view (on the right)

It is observed, from the figure 4, both two different sides of the membrane, one rich in perovskite which for a white band is visible and the other one poor in calcium titanate additive. However inside the composite Nafion membrane, the additive seems to be uniform distributed.

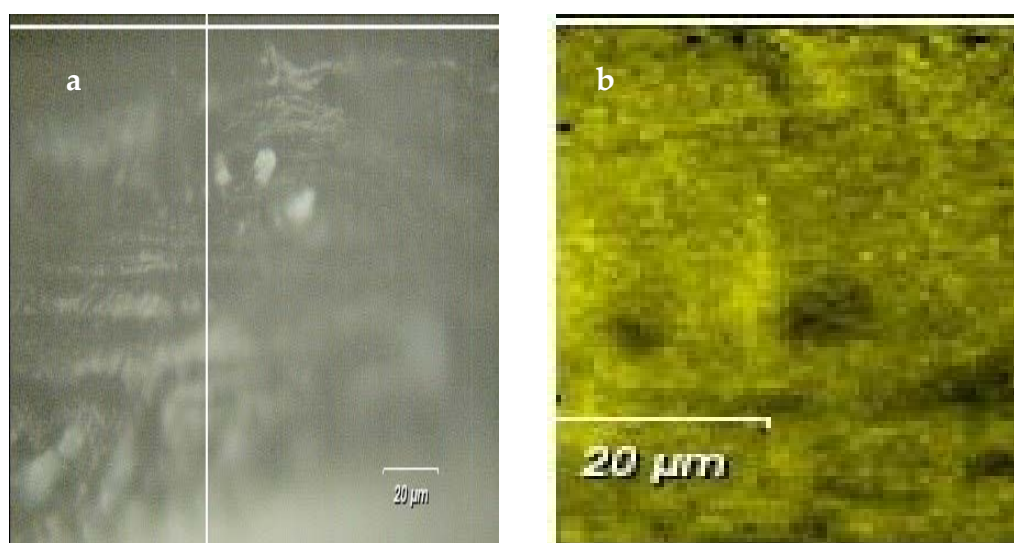


Figure 5: Raman mapping of M5 membrane: full area selected for mapping analysis (a) and Nafion (black zone) and CTO (yellow zone) distribution (b)

Considering an area of the M5 section where the perovskite particles are evident (Figure 5), a Raman mapping study of the membrane was performed. The yellow zone represent the perovskite distribution within the black zone which is the Nafion membrane.

Raman spectra was taken step-by-step, moving along a rectangular zone on the surface of the composite sample.

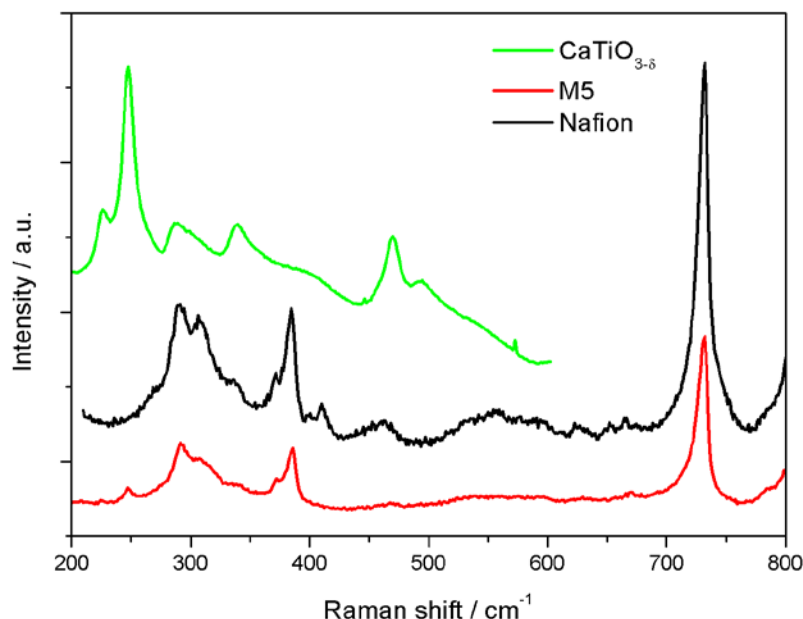


Figure 6: Raman spectra of a M5 membrane compare to Nafion membrane and CTO perovskite. In order to emphasize the major characteristic bands of the perovskite, its spectra ends to 600 cm^{-1} .

As discussed for the IR spectra, also for the Raman spectra the all peaks due to the Calcium Titanate perovskite are overlapping to the Nafion peaks except for a small one at ca 250 cm^{-1} due to the O-Ti-O bending mode. The major characteristic vibrational bands of the polymer are assigned in according to table 5^[19].

Raman shift / cm^{-1}	Assignment ^[19]
292, 310	ν (CF_2)
307, 385, 390, 574	
731, 741	ν (CF_2)

Table 5: Assignement of major Raman bands of Nafion

However, some important differences have been noticed: i) the absence in the composite membrane of bands at about 409 cm^{-1} and ii) two broad peaks at ca 460 cm^{-1} and 570 cm^{-1} related to CF_2 stretching vibration which is the signature of an important phase rearrangement of the calcium titanate component incorporated into the Nafion membrane.

Figure 7 reports the storage modulus and the elastic energy dissipation of the dry membranes measured at two fixed frequencies (1 and 10 Hz), during heating between room temperature and 180°C, with a rate of 4°C/min. The Nafion membrane shows a relaxation around 110°C, indicated by the occurrence of an intense peak in $\tan\delta$ and a two-order magnitude drop in the modulus. This relaxation, usually indicated as α -relaxation, was already largely reported^[20,21] and corresponds to the glass transition of the hydrophilic domains (polar regions) of Nafion.

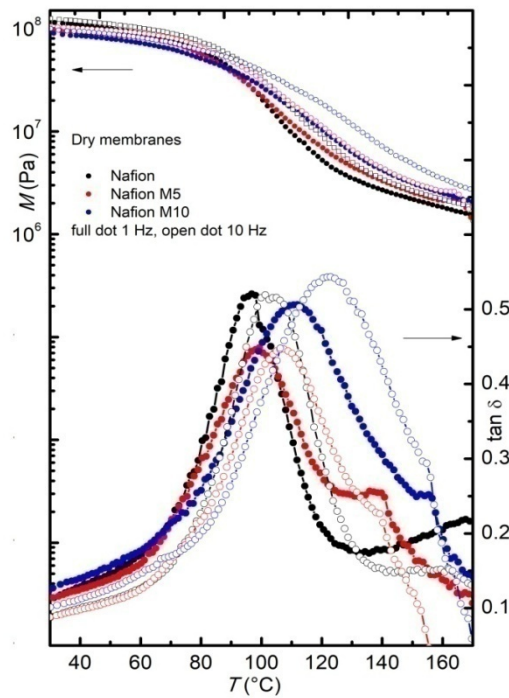


Figure 7: Storage modulus and elastic energy dissipation of pure and dry Nafion (black) and composite membranes M5 (red) and M10 (blue), measured on heating at two frequencies, i.e. $f = 1$ Hz (full dots) and $f = 10$ Hz (open dots).

In the composite membrane M5, the α -relaxation is slightly shifted to higher temperatures compared to the pure Nafion sample, and this shift is even more clear when increasing the amount of filler, since, for the M10 samples, the relaxation is observed at around 130°C. At room temperature, the modulus values of the three samples are close, while at higher temperature, the composite membranes present slightly higher modulus values, thus confirming the reinforcing action of the filler. In particular, above 90°C the modulus of the M10 membrane is the highest. Indeed, at room temperature, the modulus values could be affected by some undesired water contamination occurring during sample loading, while on heating above 100°C, these effects should be suppressed.

An increase of the modulus in a Nafion membrane, with an addition of a filler like SnO_2 nanoparticles^[22] and sulphated SnO_2 ceramic nano-powders^[23] was already observed.

The modulus and the elastic-energy dissipation of the wet membranes measured at a fixed frequency of 1 Hz during heating between room temperature and 180°C, with a rate of 4°C/min, are reported in Figure 8. The α -relaxation is shifted to slightly higher temperatures compared to the dry membranes, and the highest temperature for the maximum of the energy dissipation is observed for the wet M10 membranes, confirming that the faded filler increases the relaxation temperature.

On cooling (Figure 8), the peak associated to the α -relaxation presents its maximum at about 90°C for the pure Nafion and the M5 membranes. In both membranes the α -relaxation displays a clear thermal hysteresis between heating and subsequent cooling, as already reported for similar systems above mentioned.

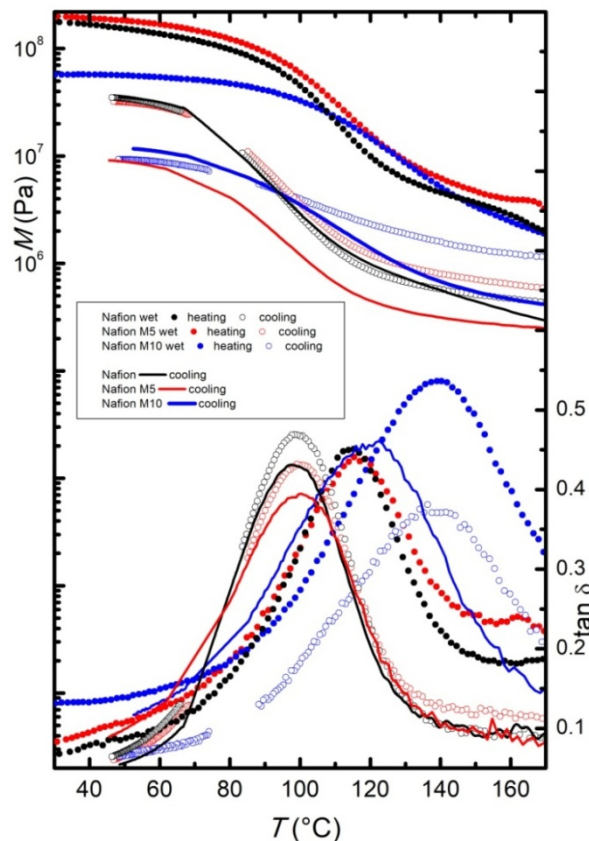


Figure 8: Storage modulus and elastic energy dissipation of pure Nafion (black) and composite membranes M5 (red) and M10 (blue) in the wet state measured at $f = 1$ Hz on heating (full dots) and subsequent cooling (open dots). Dry membranes measured at $f = 1$ Hz on cooling (lines) are also reported for comparison.

Contrarily, the peak displayed by the M10 membrane does not present a significant temperature shift when measured on cooling. For comparison, the curves (both storage modulus and $\tan \delta$) measured on cooling for the dry samples are also reported in Figure 8. The curves measured in the cooling run for the Nafion and the M5 membranes, starting from their wet state, are close to the curves measured on cooling for the corresponding dry samples. Conversely, the $\tan \delta$ measured on cooling for the M10 membranes, starting from

the wet state, displays the α -relaxation at the same temperature at which it is detected in the heating run, and well above the temperature at which it appears in the spectrum measured on cooling, starting from the dry state. Indeed, it seems that, for this latter sample, the α -relaxation shows a very small thermal hysteresis between heating and cooling, regardless of the water content, maybe due to some interactions between the higher amount of filler and the Nafion matrix.

Moreover, with a higher amount of filler, the presence of water (i.e., at wet conditions) seems to increase, more remarkably, the temperature at which this relaxation occurs.

The modulus values of the wet Nafion and M5 samples measured at room temperature before heating are close to that displayed by the corresponding membranes in the dry state, while the modulus displayed by the wet M10 membrane is slightly lower than the one measured on the dry M10 membrane, suggesting that, in this latter case, water acts more remarkably as a plasticizer that decreases the stiffness of the membranes. However, when comparing the modulus value in the cooling run, where most of the water may have evaporated, the curves are close for the same kind of samples, independent of the initial state (wet or dry). This confirms that the thermal treatment completely eliminates the hydration history of the samples. A small difference can be noticed only for the M5 membranes, where the modulus measured in the cooling run, starting from the wet state, is slightly higher than those obtained when cooling the dry sample.

The DSC curves of all membranes are displayed in Figure 9. In the investigated temperature range, a main peak is observed around 100°C, assigned to an order–disorder transition of the ionic clusters in Nafion^[24].

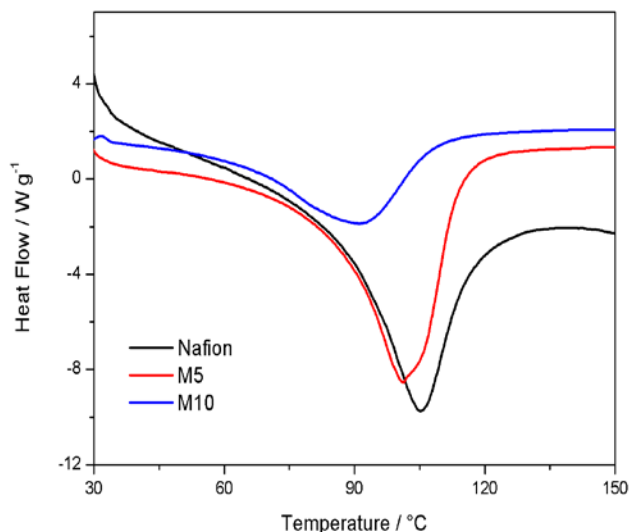


Figure 9: DSC response of the hydrated membrane samples.

The enthalpy value, calculated by integrating the DSC peak, associated to this endothermic phenomenon, was evaluated and is reported in Table 6.

Samples	T_{onset} (°C)	ΔH (Jg ⁻¹)
N	105	737,83
M5	106	746,89
M10	95	380,32

Table 6: Value of ΔH and T_{onset} associated to the thermal transition observed by DSC

In accordance to the literature^[25], only water associated with Nafion hydrophilic groups contributed to this thermal transition. In particular, the enthalpy value increased with an increasing degree of hydration of the polymer, leading to a major organization of ionic clusters and more cohesive interactions. At the same time, the change in temperature of the transition peak is attributed to a plasticizing effect of water, for which a shift toward lower temperatures may correspond to higher hydration levels. However, in our case, the change in the enthalpy values is much more significant than that in T_{onset} .

Among all samples, the composite membrane M5 (containing 5 wt.% of the $\text{CaTiO}_{3-\delta}$ additive) shows a higher ΔH value than both M10 (10 wt.% of $\text{CaTiO}_{3-\delta}$) and, to a lower extent, N (plain Nafion) samples. The addition of $\text{CaTiO}_{3-\delta}$ particles caused an increase in the water content, even though the M10 sample, having the highest concentration of additive, displayed the lowest water affinity, possibly due to phase segregation and a non-optimized distribution of the inorganic additive, which can prevent the motions of the segments among the fluorocarbon backbone to restrict the water release^[26,27].

The TGA curves obtained for the three membranes are shown in Figure 10. The thermal decomposition of the Nafion membrane occurs in three main steps. The first decomposition is associated with desulfonation of the side-chain of the polymer; the second and the third transitions, occurring in the range 350–450°C, are related to side-chains and perfluorinated backbone decompositions^[28].

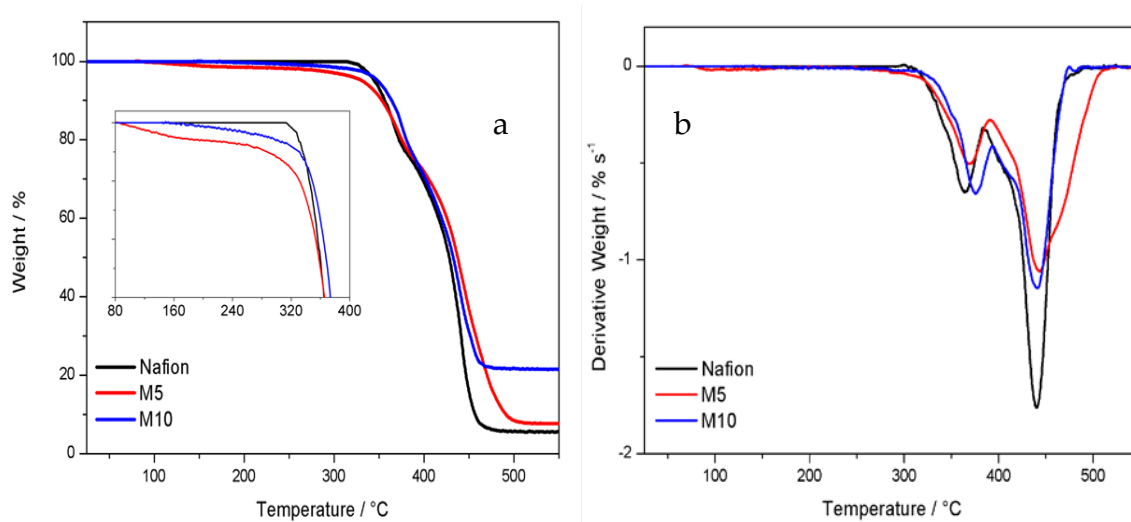


Figure 10: TGA (a) and DTG curves (b) recorded for the dry membranes

The TGA profiles show that all the membranes are thermally stable up to 300 °C, even though, compared to plain Nafion, the two composite samples exhibit slightly higher decomposition temperatures, as better shown by the derivative curves (see DTG curves in Figure 10 b).

In particular, the last thermal process looks broader and shifted to higher temperatures for the M5 sample, suggesting a stabilizing interaction between the filler and the Nafion matrix. Moreover, as shown in the inset of TGA profiles (see Figure 10 a), the composite membranes exhibit a smooth mass loss in a lower temperature range (below 300°C), most likely due to traces of surface water still present in the membrane after the drying treatment carried out at 80°C prior to the measurement. This can be explained in terms of extra hygroscopicity induced by the inorganic fillers.

The presence of surface water looks to be more evident in M5. This could be explained by considering an optimal concentration/dispersion of the perovskite additive, able to hold water during the drying step and to release it gradually at higher temperature. The greater slope observed in M5, as compared to M10 (see inset of Figure 10 a), suggests a higher content of surface water. Considering the final weights after TGA analysis, it is clear that the M10 membrane leaves a higher amount of residual weight, in respect to the other samples. This evidence could be interpreted by assuming a strong interaction between the Nafion polymer and the perovskite particles, for which the removal of the decomposed Nafion products at a high temperature is more difficult.

Figure 11 shows the frequency dependence of the imaginary part of the permittivity (ϵ'') as a function of frequency for plain Nafion, M5, and M10, at a given temperature of 20°C, during cooling.

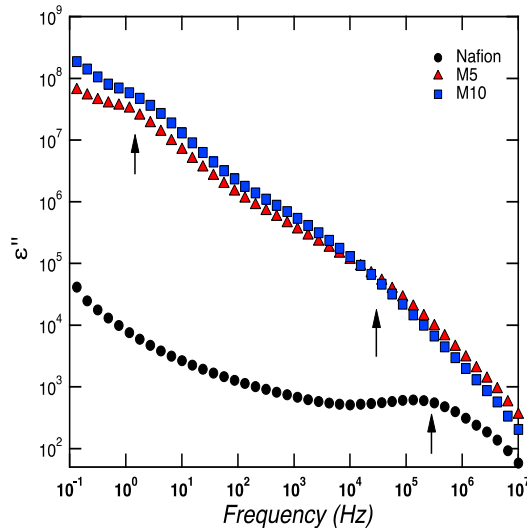


Figure 11: Frequency dependence of the imaginary part of the permittivity for Nafion, M5 and M10 at a given temperature of 20 °C during cooling.

For samples M5 and M10, two clear dielectric relaxation processes are observed at high and low frequencies. These relaxation processes, called β -relaxations (i.e., β_1 , β_2) and generally observed at a low temperature (i.e., lower than T_g), were attributed to conformational changes of the ether group bound to the backbone end of the side-chain or the ether group bound to the sulfonate end of the side-chain^[29].

These β -relaxations are completely different from the main structural α -relaxation, which occurs at higher temperatures, around 110°C, as revealed by DMA measurements, and is associated to the long-range movement of the fluorocarbon domains (i.e., to T_g). In the case of Nafion, one major β -relaxation process is observed at high frequencies, while, at the limit of the lowest frequency investigated, the shape of the curve is reminiscent of the tail of a β -relaxation (peaked at low frequencies outside the frequency window investigated). A similar behavior was found in Nafion membranes investigated by Di Noto et al^[30]. Both β -relaxations (i.e., β_1 , β_2) become faster with increasing temperature and move to higher frequencies, which implies that, at 80°C, both are outside the experimental frequency window investigated (see Figure 12).

This figure shows that the main structural α -relaxation is not observed within the studied frequency window, but two conductivities are detected instead. These are recognized by the typical slope of -1 .

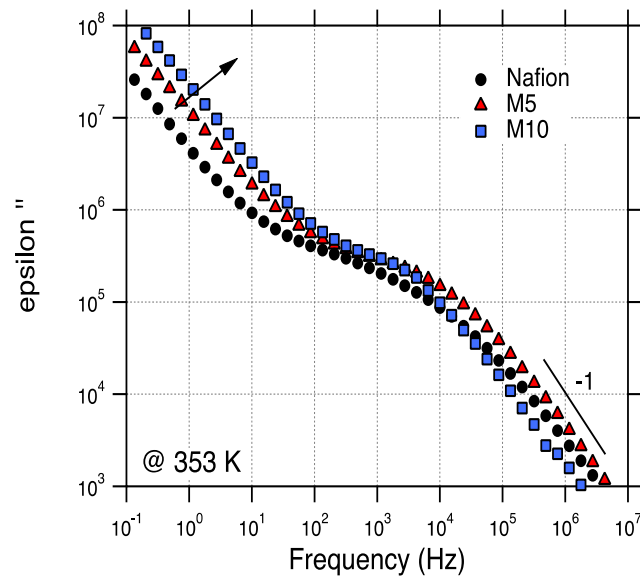
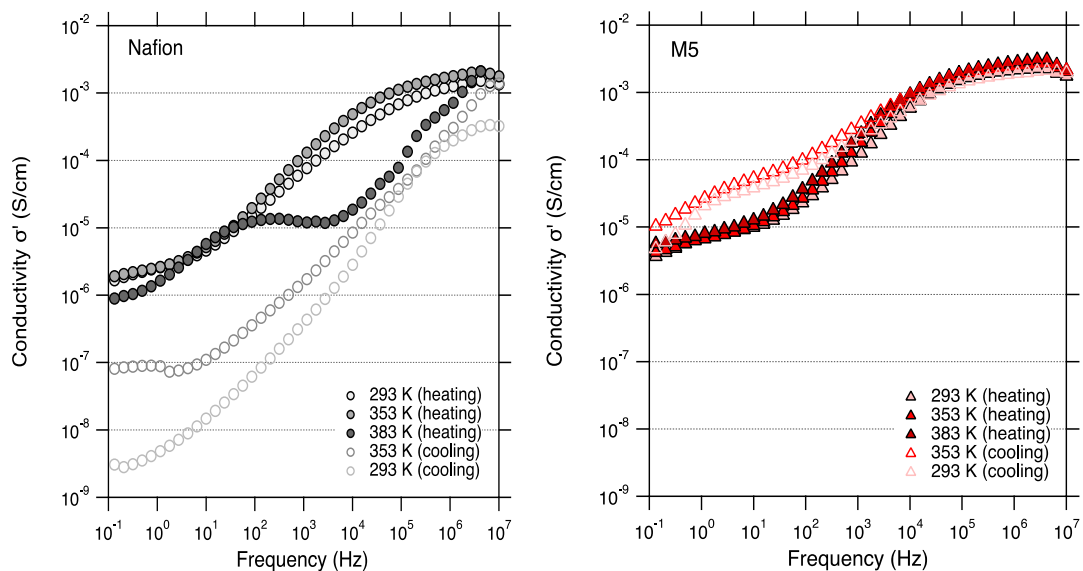


Figure 12: Frequency dependence of the imaginary part of the permittivity for Nafion, M5 and M10 at a given temperature of 80 °C during heating.

We propose to assign the conductivity observed at low frequencies (i.e. in the range 10⁻¹–10 Hz) to localized and slow phenomena whereas the conductivity at higher frequencies (i.e. in the range 10⁴–10⁶ Hz) is attributed to long range bulk or dc conductivity. Both these two conductivities are associated to ϵ'' with a slope of -1 and become faster with an increasing concentration of CaTiO_{3- δ} (see arrow in Figure 12).

The conductivity curves recorded for all three membranes (Nafion, M5 and M10) and over the whole frequency window as well as for all temperatures (i.e. 20 °C, 80 °C and 110 °C) are shown in Figure 13, both for the heating and cooling scans.



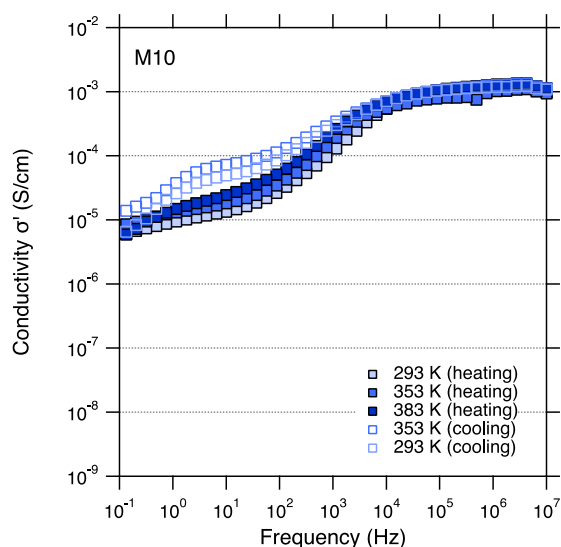


Figure 13: Conductivity (σ') spectra as a function of frequency for Nafion, M5 and M10 during heating and cooling.

Two characteristic ranges can be observed, at low (10^{-1} – 10 Hz) and high (10^4 – 10^6 Hz) frequencies, a behavior similar to that described by Di Noto et al., in the investigation of dry and wet Nafion^[31].

The conductivity at low frequencies (10^{-1} – 10 Hz) shows a similar general trend for the three samples, increasing with increasing temperatures during heating and decreasing, with decreasing temperature during cooling. However, the conductivity at high frequencies (10^4 – 10^6 Hz) shows different behaviors in the three samples. For Nafion, the conductivity values are lowered by one order of magnitude after heating to 110°C , which most likely reflects the dehydration of the membrane.

For M5, the conductivity values during heating and cooling shows a small but detectable change, with the conductivity increasing upon increased temperature. M5 also shows the highest conductivity, reaching a value at 110°C of $3.1 \times 10^{-3} \text{ S}\cdot\text{cm}^{-1}$.

For M10, there is no significant change in conductivity during heating and cooling and a value about $1.2 \times 10^{-3} \text{ S}\cdot\text{cm}^{-1}$ is measured. These trends are better visualized in Figure 14.

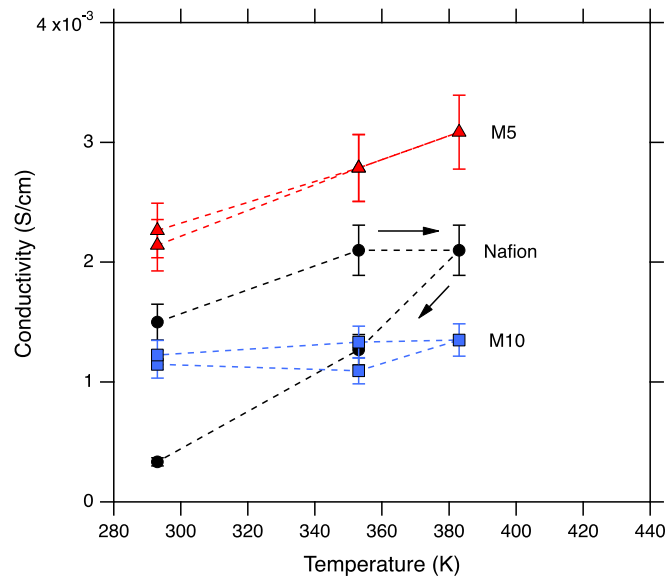


Figure 14: The dc conductivity as a function of temperature for Nafion, M5 and M10 during heating and cooling.

Figure 15 shows the dependence of the dc conductivity on composition, for the representative temperature of 80 °C. The three samples all exhibit a reasonably high conductivity ($\sim 10^{-3} \text{ S}\cdot\text{cm}^{-1}$) although M5 displays the highest value, indicating that a too high concentration of $\text{CaTiO}_{3-\delta}$ can be detrimental for this particular property. This can be justified by considering the morphology of the composite membranes studied by SEM analysis and explained in the next paragraph.

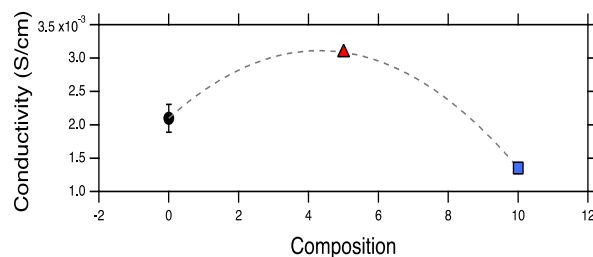


Figure 15: Concentration dependences of the conductivity as a function of different perovskite contents at 80 °C

Mazzapioda L, Navarra M.A., Trequattrini F, Paolone A, Elamin K, Martinelli A, Palumbo O; "Composite Nafion membranes with $\text{CaTiO}_{3-\delta}$ additive for possible applications in electrochemical devices" *Membranes*, 9,143, 2019

4.4 DIRECT METHANOL FUEL CELLS TESTS

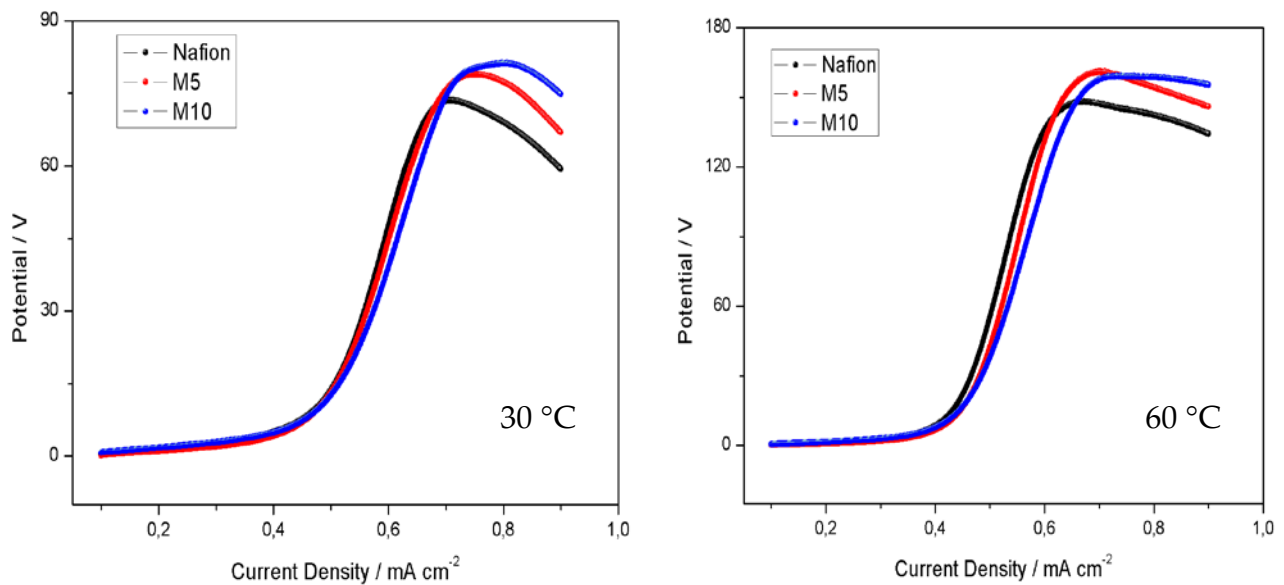
4.4.1 METHANOL CROSSOVER MEASUREMENTS

In Direct Methanol Fuel Cells (DMFCs), methanol crossover is a critical issue which is responsible of cathode catalyst poisoning causing about a 30% performance reduction in term of fuel cell efficiency^[32].

Nafion possesses high methanol permeability because of its hydrophilic channels, and partially blocking these channels will significantly reduce the crossover.

In according with literature, in the composite approach, the extent of methanol crossover largely depends on the distribution of fillers and their effective interaction with the polymer matrix^[33]. The uniform distribution of fillers in Nafion membranes reduces the size of channels that are available for methanol passage, whereas particles agglomeration has a negative impact on methanol crossover.

Unfortunately, in our case the methanol crossover increases after modification of the Nafion membrane with $\text{CaTiO}_{3-\delta}$ particles, increasing with increasing temperature (Figure 16).



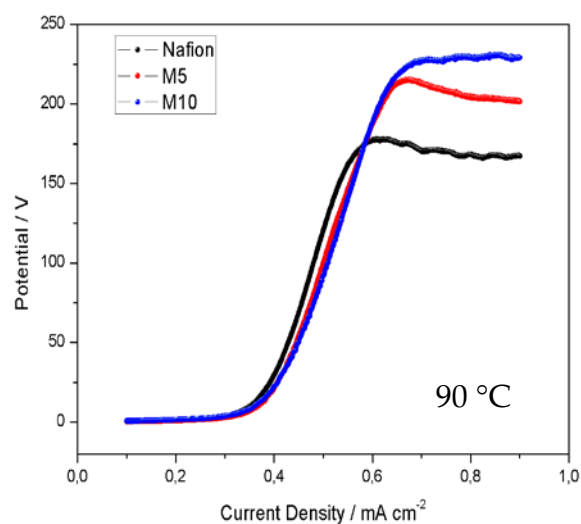


Figure 16: Crossover effect at 30°C, 60°C and 90 °C

This detrimental effect is more evident for M10 sample confirming that an excessive amount of the perovskite can hinder the Nafion utilization. This could be understood better from the SEM images (Figure 17 and 18), revealing a surface morphology of Nafion membranes where the additive particles are not uniformly distributed giving rise to two different sides as demonstrate by vibrational spectroscopy.

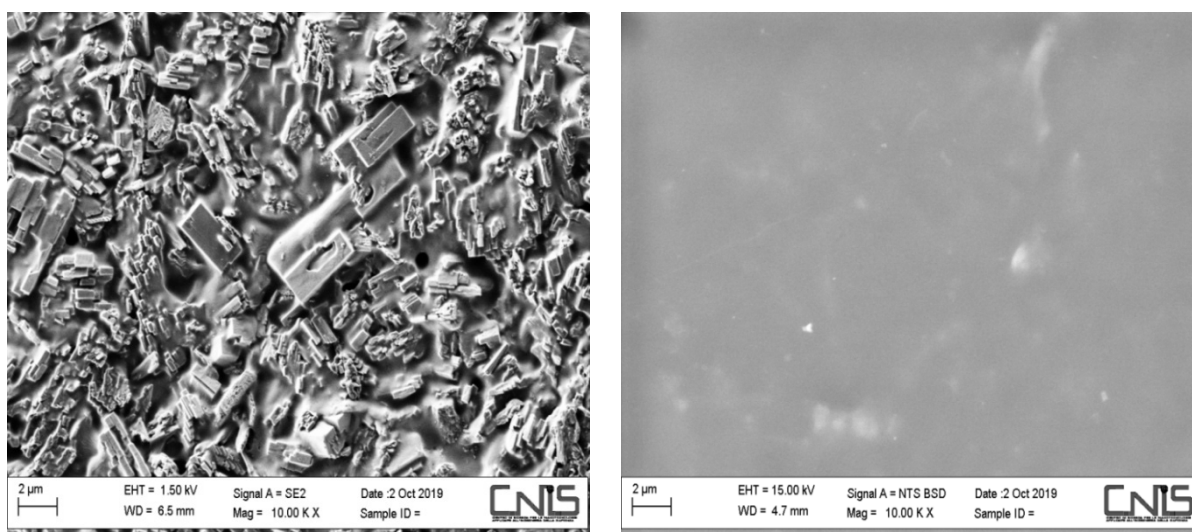


Figure 17: SEM images of both M5 sides, one rich in perovskite (left) the other poor (right).

In particular, comparing two composite membranes on the side rich in perovskite, it is remarkable that in M5, the mixing of the perovskite with Nafion is uniformly distributed on the surface of the membrane whereas in M10 sample the presence of the perovskite is so excessive to hide completely the Nafion component.

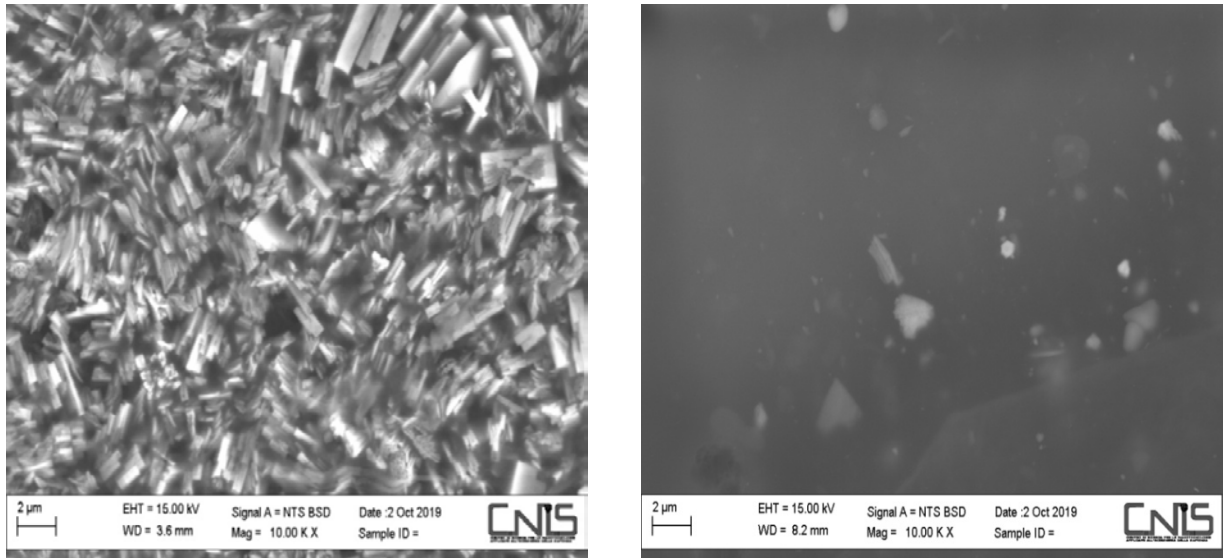


Figure 18: SEM images of both M10 sides, one rich in perovskite (left) the other poor (right).

At this point it is clear the existence of a critical filler concentration that influences the morphology of the composite membrane. Furthermore, as reported in previous studies an excessive additive begins to form agglomerates in the composite membrane, the hydrophobic polymer backbones will occur around the hydrophilic ion-cluster for methanol permeation, increasing the whole permeability^[34].

In our case, the bad performance in terms of methanol crossover can be still explained consider another aspect characteristic of the calcium titanate additive, the presence of oxygen vacancies in the lattice of the perovskite.

The oxygen defects has been considered as a strategy to improve the number of active sites able to adsorb oxygen-containing ligands, such as methanol molecules.

Yang et al^[35] reported a study about an ultrathin nickel oxide rich in oxygen vacancies demonstrating that the presence of these oxygen defects can enhance the methanol oxidation reaction (MOR) performance.

Consequently the capability of oxygen vacancies to interact with methanol molecules can promote the methanol permeability through to the Nafion membranes justifying the results obtained.

4.4.2 DIRECT METHANOL FUEL CELL PERFORMANCES

The application of composite membranes developed in this study was evaluated in a DMFC single cell at four different temperature under ambient pressure.

Comparative polarization curves and power densities of pristine Nafion and Nafion composite membranes are shown in Figure 19. The composite Nafion membranes show a high polarization loss and low peak power density due to the high methanol crossover and low proton conductivity as expected. In contrast, MEAs fabricated with the Nafion membrane exhibits higher peak power densities compared to composite samples.

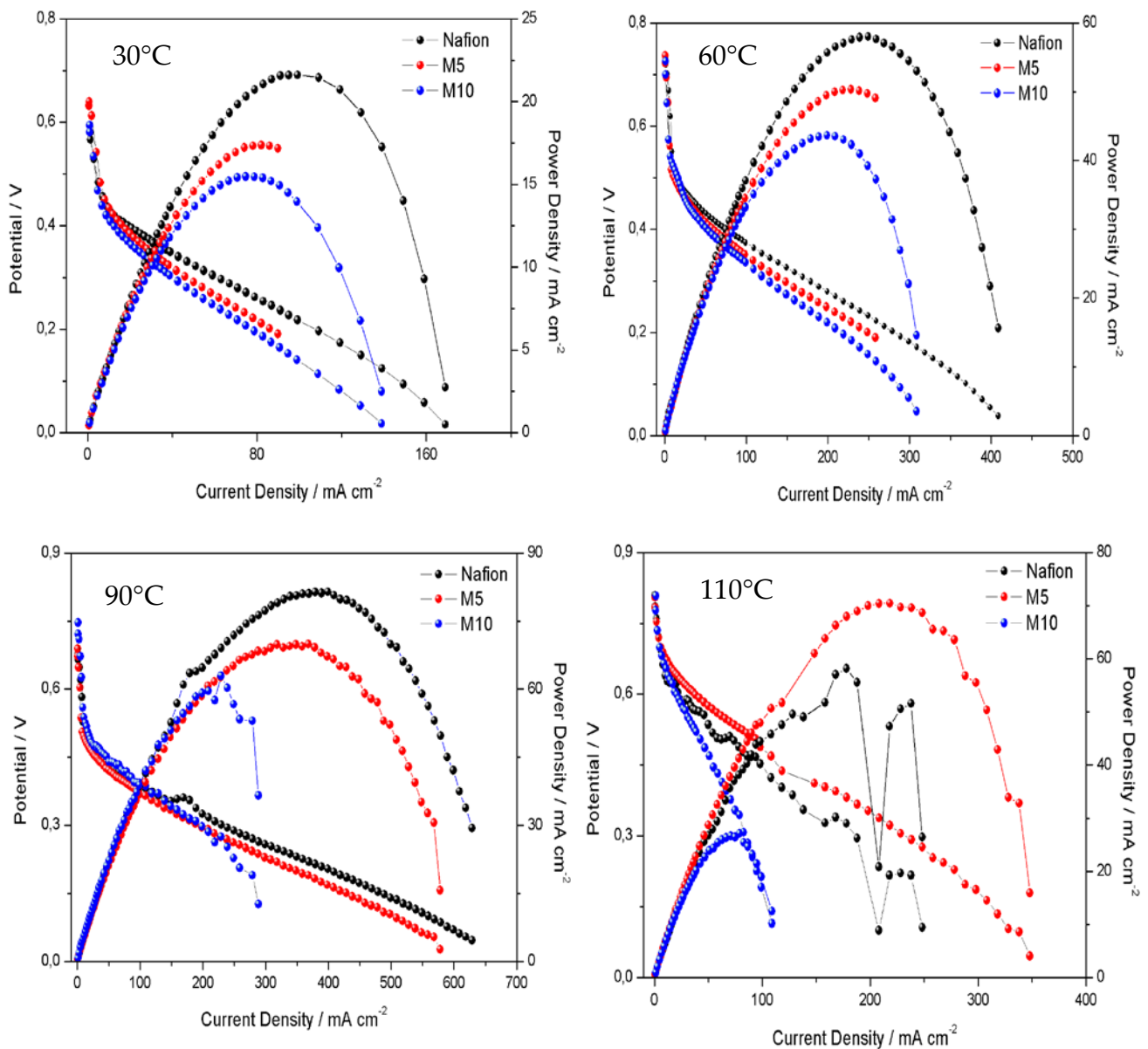


Figure 19: Direct Methanol fuel cell performances at 30°C, 60°C and 90 °C

However, among the composite membranes, M5 membrane with 5 wt. % filler content shows the best performance in terms of power density than the other composite membrane.

The correlation between the cell performance and methanol crossover confirms the existence of a limit in terms of filler concentration and a limit in the applicability of this type of composite matrix for the direct methanol fuel cells.

Indeed, the improvement of the methanol crossover with increasing the temperature lead to decrease the fuel cell performance and contemporary to increase the cell resistance. This last aspect is visible in the middle region of the polarization curve where all composite membranes exhibit important losses in the ohmic region with respect to plain Nafion sample, causing the lack of proton transfer carrier and leading to poor proton conductivity. However, if the operation temperature is 110°C, the MEA using M5 composite membrane show the best performance, as a result of a better thermal stability of Nafion membrane due to the presence of the additive.

Samples	30°C	60°C	90°C	110 °C
N	0,581	0,733	0,677	0,809
M5	0,632	0,737	0,689	0,806
M10	0,594	0,726	0,747	0,808

Table 7: *Open circuit voltage obtained at increasing temperature (30°, 60°,90°C)*

It is interesting to note that the open circuit voltage (OCV) of the MEA using the composite membrane were higher than the MEA using Nafion membrane.

This means that the methanol permeability of composite membrane performances is lower with respect to Nafion membrane at lower current density. Consequently, the mixed potential formed by methanol crossover at the cathode side is reduced and the cell's open circuit voltage is improved. Apparently, the most important contribution of the inorganic additive is seen in terms of reduced activation losses.

This aspect is in contradicton with the methanol crossover results. Among all the composite membranes, M10 sample seem to show the highest OCV value passing from 60°C to 110°C even though it shows larger mass diffusion over-potentials, as evident from the slope changes at the highest current values, resulting in fuel cell performances worse than others samples.

This strange behavior could be justified considering the double faces of composite membranes that can influence both electrode/electrolyte interface in the cell.

Overall, the presence of the perovskite affects different features of the composite membrane, that are i) the proton conductivity, ii) the methanol crossover and iii) the resistivity at the membrane/electrode interface.

With respect to this latter point, a beneficial effect of the inorganic additive on the relaxation process of Nafion with temperature ensuring a better interface contact with the electrodes, was already observed.

4.5 CONCLUSIONS

In the present chapter a composite membrane based on a Nafion polymer matrix incorporating a $\text{CaTiO}_{3-\delta}$ additive have been proposed and characterized. In particular two different filler contents, namely two concentrations of 5 wt% and 10 wt % of the $\text{CaTiO}_{3-\delta}$ additive, with respect to the dry Nafion content were considered.

A detailed analysis in term of structure, proton conductivity, methanol crossover and operating direct methanol fuel cells performances were tried.

By comparing the results obtained an improved water affinity and enhanced proton conductivity is observed for a low concentration of the filler (around 5 wt%), whereas higher filler contents (about 10 wt%) are not beneficial for the thermal and conducting performance of the membrane.

We suggest that a too high dose of additive can be detrimental for these particular properties.

A general drawback related to the improvement methanol crossover was observed during the methanol crossover analysis and in a working direct methanol fuel cells.

This apparent enhanced seem to be due to both the non-uniform distribution of the filler within the polymer and the presence of oxygen vacancies in the lattice of the perovskite that can promote the methanol permeability through the Nafion membrane.

Consequently, future several efforts are needed to optimize the interfacial and contact resistance of composite Nafion membrane by determining a proper synthesis procedure involving suitable dispersion of the additive within Nafion matrix.

In anycase, our results confirm the role of the functionalized calcium titanate perovskite in improving the properties of the sample when added in a proper concentration.

REFERENCE

- [1] Li Q., Yin Q., Zheng Y.S., Sui Z.J., Zhou X.G., Chen D., Zhu Y. A., *Langmuir*, 35, 9962, **2019**
- [2] Krüner K. D., *Annu. Rev. Mater. Res.* 33, 333, **2003**
- [3] Kreuer K.D., Adams S., Münch W., Fuchs A., Klock U., Maier J. *Solid State Ion.*, 145, 295, **2001**
- [4] Stølen S., Bakken E., Mohn C.E. *Chem. Chem. Phys.*, 8, 429, **2006**
- [5] Pionke M., Mono T., Schweika W., Springer T., Schober H. *Solid State Ionics*, 97, 497, **1997**
- [6] Siracusano S., Baglio V., Nicotera I., Mazzapioda L., Aricò A.S., Panero S., Navarra M.A., *Int. J. Hydrogen Energy*, 42, 27851, **2017**
- [7] Branchi M., Sgambetterra M., Pettiti I., Panero S., Navarra M.A., *Int. J. Hydrogen Energy*, 40, 14757, **2015**
- [8] Nicotera, I., Kosma V., Simari C., Ranieri G.A., Sgambetterra M., Panero S., Navarra M.A., *Int. J. Hydrogen Energy*, 40, 14651, **2015**
- [9] Teocoli F., Paolone A., Palumbo O., Navarra M.A., Casciola M., Donnadio A., *J. Polym. Sci. Pol. Phys.* 50, 1421, **2012**
- [10] Slade S.M., Ralph T.R., De Ponce León C., Campbell S.A., Walsh F.C., *Fuel Cells*, 10, 567, **2010**
- [11] Neelakandan S., Kanagaraj P., Nagendran A., Rana D., Matsuura T., Muthumeenal A., *Renew. Energy*, 78, 306, **2015**
- [12] Qi Z., Kaufman A., *J. Power Sources*. 110, 177, **2002**
- [13] Lufrano F., Baglio V., Di Blasi O., Staiti P., Antonucci V., Aricò A.S., *Phys. Chem. Chem. Phys.* 14, 2718, **2012**
- [14] Baglio V, Stassi A, Matera F.V, Di Blasi A, Antonucci V, Aricò A.S, *J. Power Sources* 180,797, **2008**
- [15] Fernandez Bordina S.P., Andrada H.E., Carrerasa A.C., Castellano G.E., Oliveira R.G., Galván Josa V.M. *Polymer* 155, 58, **2018**
- [16] Deabate S., Gebel G., Huguet P., Morin A., Pourcelly G., *Energy Environ. Sci.* 5, 8824, **2012**
- [17] Singh R.K., Kunitatsu K., Miyatake K., Tsuneda T., *Macromolecules*, 49, 6621, **2016**
- [18] Suna C., Zlotorowicz A., Nawna G., Negro E., Bertasia F., Pagota G., Vezzù K., Pace G., Guarnierie M., Di Noto V., *Solid State Ionics*, 319, 110, **2018**
- [19] Gruger A., Régis A., Schmatko T., Colomban P., *Vibrational Spectroscopy*, 26, 215, **2001**
- [20] Teocoli F., Paolone A., Palumbo O., Navarra M.A., Casciola M., Donnadio A., *J. Polym. Sci. Pol. Phys.*, 50, 1421, **2012**
- [21] Scipioni R., Gazzoli D., Teocoli F., Palumbo O., Paolone A., Ibris N., Brutti S., Navarra M.A., *Membranes*, 4, 123, **2014**

- [22]Trequattrini F., Palumbo O., Vitucci F. M., Miriametro A., Croce F., Paolone A., *Materials Research*,21, **2018**
- [23]Paolone A., Palumbo O., Teocoli F., Cantelli R., Hassoun J, *Solid State Phenomena*, 184, 351, **2012**
- [24]Lage L.G., Delgado P.G., Kawano Y., *J. Therm. Anal. Calorim.*, 75, 521, **2004**
- [25]Sgambetterra M., Brutti S., Allodi V.,Mariotto G., Panero S., Navarra M.A., *Energies*, 9, 272, **2016**
- [26]Mazzapioda L., Panero S., Navarra M.A., *Polymers*, 11, 914, **2019**
- [27]Navarra M.A., F. Croce F., Scrosati B., *J. Mater. Chem.*, 17, 3210, **2007**
- [28]Di Noto V., Boaretto N., Negro E., Giffin G.A., Lavina S., Polizzi S., *Int. J. Hydrogen. Energy*, 37, 6199, **2012**
- [29] Di Noto V., Piga M., Pace G., Negro E., Lavina S. *ECS Transactions*, 1183, **2008**
- [30] Giffin A. G., Piga M., Lavina S., Navarra M.A., D'Epifanio A., Scrosati B., Di Noto V., *J. Pow. Sour.* 198, 66, **2012**
- [31]Di Noto V., Gliubizzi R., Negro E., Pace G., *J. Phys. Chem. B.*, 110, 24986, **2006**
- [32]Chen, F., Mecheri B., D'Epifanio A., Traversa E., Licocchia S. *Fuel Cells*, 10, 790, **2010**
- [33] Yituo Wang Y., Guimei Han G., Zhe Tian Z., Wang M., Liab J., Wang X., *RSC Adv.*, 4, 47129, **2014**
- [34] Parthiban Velayutham P., Akhila K. Sahu A., Parthasarathy S., *Energies*, 10, 259, **2017**
- [35] Yang W., Yang X., Jia J., Hou C., Gao H., Mao Y., Wang C., Lin J., Luo X., *Applied Catalysis B: Environmental* 244, 1096, **2019**

GENERAL CONCLUSIONS

The aim of this PhD thesis has been the development of advanced materials to be used as both electrocatalysts and electrolyte additives, in order to reduce cost and improve performance and durability of low temperature fuel cells.

In particular our interest was focused on non-stoichiometric Calcium Titanate Perovskites, $\text{CaTiO}_{3-\delta}$ (CTO) and $\text{CaTi}_{0.8}\text{Fe}_{0.2}\text{O}_{3-\delta}$ (CTFO), both used as co-catalyst for the oxygen reduction reaction (ORR), which is the main rate-decreasing step in the fuel cell devices. The specific goals were to improve the stability and durability of Pt catalysts and to support Pt catalytic activity in order to reduce its loading.

The $\text{CaTiO}_{3-\delta}$ perovskite was also used as additive in Nafion membrane in order to enhance the water retention, the mechanical properties of the membrane and reduce the gas/methanol crossover.

Appropriate and powerful techniques were used for the characterization of the materials here proposed.

A suitable and novel synthesis procedure was carried out to obtain a non-stoichiometric Calcium Titanate perovskite (CTO), using the Pluronic F127 template both as structure directing agent and as reducing agent, in order to promote the formation of oxygen vacancies.

On the basis of physical chemical characterizations, such as TGA analysis and pressure-controlled measurements, we have demonstrated the presence of oxygen vacancies on the lattice of the perovskite enabling oxygen sorption. The presence of holes or imperfections on the perovskite particles is visible from SEM images, supporting the hypothesis of possible surface adsorption ability. Overall, the amount of the oxygen defective sites is not so high ($\delta \approx 0.025$), this could be explained considering the low amount of the reducing template agent adopted in the synthesis with respect to the amount of the inorganic precursors.

This perovskite was investigated as an additive of Pt for oxygen reduction reaction in acidic media. Three composite catalysts were prepared, with different amount of perovskite, Pt/C:CTO 1:1, Pt/C: CTO 1:2 and Pt/C:CTO 1:2.5. A commercial Pt/C catalyst was used as reference.

RDE measurements, used to study oxygen reduction reaction, have revealed that the catalyst Pt/C:CTO 1:1 posses the best activity, presenting a 4e- reduction pathway and delivering an higher limiting current density with respect to the other samples.

This has been explained considering the perovskite as an active additive that, thank to the presence of oxygen vacancies, allows the interaction between the catalyst surface and water, providing additional protons and electrons with respect to platinum reaction products. Furthermore, from both electrochemical analysis and SEM images, it was clear that, when Pt was in the same weight ratio with the perovskite, we have obtained the best composition to achieve better results; this mean that the amount of additive used to prepare composite electrodes can play a key role to achieve better performances.

The stability of the Pt/C:CTO 1:1 composite catalyst was studied and compared to the bare Pt/C catalyst by accelerated degradation tests. The catalyst Pt/C:CTO 1:1 showed an

excellent electrochemical stability, associated to high corrosion resistance compared to the benchmark Pt/C.

A performance analysis of the most active Pt/C:CTO 1:1 catalysts as composite cathode was carried out in a direct methanol fuel cell and it was compared with bare Pt/C. Fuel Cell performances were generally positively affected by the presence of the perovskite. In particular, the use of the $\text{CaTiO}_{3-\delta}$ allows to work in more drastic conditions, i.e. high methanol concentration and higher temperature with respect to Pt/C cathode based MEA.

A second additive, a iron-doped calcium titanate perovskite ($\text{CaTi}_{1-x}\text{Fe}_x\text{O}_{3-\delta}$, CTFO) was synthesized, with the aim of improving bulk electron conductivity. CTFO was originally prepared by High Energy Ball Milling, starting from stoichiometric amounts of CaCO_3 , TiO_2 and $\text{FeO}(\text{OH})$ and used as an additive of Pt for ORR in acidic media.

Two composite catalysts were prepared, Pt/C:CTFO 1:0,5 and Pt/C:CTFO 1:1, and compared with a commercial Pt/C. RDE measurements have shown that the catalyst Pt/C:CTFO 1:1 posses the best activity toward the ORR, presenting a 4e⁻ reduction pathway and exhibiting the highest limiting current density among all the other samples. Also in this case, the right amount of the perovskite can alter the ORR mechanism from 2e⁻ pathway to a 4e⁻ pathway, in fact a poor amount of additive was not sufficient to improve the Pt/C catalytic activity. By this preliminary studies in term of chemical-physical and electrochemical characterization about CTFO perovskite, we have demonstrated that this iron-doped perovskite has promising features to be used as cathode catalyst support for low temperature fuel cells.

Composite membrane based on a Nafion polymer matrix incorporating a $\text{CaTiO}_{3-\delta}$ additive have been proposed and characterized. In particular two different filler contents, namely two concentrations of 5 wt% and 10 wt % of the $\text{CaTiO}_{3-\delta}$ additive, with respect to the dry Nafion content, were considered.

A detailed study has been developed to elucidate mechanical properties, structure, proton conductivity, methanol crossover and operating Direct Methanol Fuel Cells (DMFCs) performances of all the Nafion membranes (Nafion, M5 and M10).

The mechanical properties of the membranes were measured by DMA in the so-called "tension configuration" in order to evaluate the interplay of the transition/relaxation phenomena in Nafion membranes at high temperature and under humidified conditions.

In the composite membrane M5 the α -relaxation is slightly shifted to higher temperatures compared to the pure Nafion sample, and this shift is even more clear when increasing the amount of filler, since for the M10 samples the relaxation was observed around 130 °C. At room temperature the modulus values of the three samples are close, while at higher temperature the composite membranes present slightly higher modulus values, thus confirming the reinforcing action of the filler. In particular above 90°C the modulus of the M10 membranes is the highest. Moreover, at higher amount of filler, the presence of water (i.e., wet conditions) seems to increase more remarkably the temperature at which this relaxation occurs.

The thermal analysis, based on TGA and DSC analysis have been used to investigate both the thermal behavior and the water content of the membranes in order to define their stability range and their hydration state.

During my traineeship in Sweden, the SAXS-MAXS measurements were performed to understand the interactions between the filler and the Nafion matrix whereas the dielectric measurements has been used to evaluate the ionic conductivity of membranes. Both studies were carried out at fully humidified conditions.

By comparing all the results obtained, the membrane with the lower amount of additive (M5) displays the better performances both in terms of water affinity and conductivity. We suggest that a too high dose of additive can be detrimental for these particular properties.

A general drawback related to the improvement methanol crossover was observed during the methanol crossover analysis and in a working direct methanol fuel cells.

This apparent enhanced seem to be due to both the non-uniform distribution of the filler within the polymer, and the presence of oxygen vacancies in the lattice of the perovskite that can promote the methanol permeability through the Nafion membrane.

From both ATR and Raman vibrational spectroscopy and SEM images two different sides of composite Nafion membranes have been observed. It was proved that the filler during the solvent casting procedure develop a concentration profile giving rise a two different Nafion surface, one rich in additive and the other one poor in perovskite.

The issues of inhomogeneous dispersion and non-optimized filler-to-polymer interactions appear particularly critical in this work due to the micrometric size of the calcium titanate particles, exceeding the dimension of the hydrophilic domains and, possibly, occluding them to some extent.

Moreover, a too high filler concentration could block the ionic channels and impede ionic motion and this aspect can influence the performance of the composite membranes in a working fuel cell.

Consequently, future several efforts are needed to optimize the interfacial and contact resistance of composite Nafion membrane by determining an appropriate synthesis procedure involving suitable dispersion of the additive within Nafion matrix.

In anycase, the reported results indicate that composite membranes obtained by adding calcium titanate as filler in a Nafion matrix display interesting properties that ought to be considered for electrochemical applications, such as in PEMFCs.

Ongoing and future studies will address the use of the perovskite as co-catalyst in a H₂/air PEM fuel cell and as additive in composite membranes tested in the same fuel cell, paying attention on which side of the sample is exposed to the anode or cathode compartment, in order to evaluate the possible effect due to the different interfaces.

Publications

- I. Siracusano S., Baglio V., Nicotera I., Mazzapioda L., Aricò A.S., Panero S., Navarra M.A. "Sulfated titania as additive in Nafion membranes for water electrolysis applications", *International Journal of Hydrogen Energy*, **2017**, 42, 27851
- II. Siracusano S., Oldani C., Navarra M.A, Tonella S., Mazzapioda L., Briguglio N., Aricò A.S. "Chemically stabilised extruded and recast short side chain Aquivion® proton exchange membranes for high current density operation in water electrolysis" *Journal of Membrane Science*, **2019**, 578, 136
- III. Mazzapioda L., Panero S., Navarra M.A "Polymer Electrolyte Membranes based on Nafion and a Super acidic Inorganic Additive for Fuel Cell applications" *Polymers* **2019**, 11, 914
- IV. Mazzapioda, L.; Lo Vecchio, C.; Paolone, A.; Aricò, A. S.; Baglio, V.; Navarra, M. A.; "Enhancing Oxygen Reduction Reaction Catalytic Activity Using $\text{CaTiO}_{3-\delta}$ Additive", *Chem. Electro. Chem*, **2019**,6, 65951. Invited for the journal Cover Picture and the Cover Profile.
- V. Mazzapioda L, Navarra M.A., Trequatrini F, Paolone A, Elamin K, Martinelli A, Palumbo O;
"Composite Nafion membranes with $\text{CaTiO}_{3-\delta}$ additive for possible applications in electrochemical devices" *Membranes*, **2019**, 9, 143
- VI. Mazzapioda L, Lo Vecchio, C.; Aricò, A. S Navarra, M. A., Baglio, V.;
"Performance Improvement in Direct Methanol Fuel Cells by Using $\text{CaTiO}_{3-\delta}$ Additive at the Cathode" *Catalysts*, **2019**, 9, 1017

Attended Conferences

European Congress and Exhibition on Advanced Materials and Processes (EUROMAT 2019), Stockholm, 1-5 September 2019

“Perovskite Titanate as Electrode and Electrolyte Additive for Direct Methanol Fuel Cells” (Oral presentation)

Lucia Mazzapioda, Carmelo Lo Vecchio, Antonino Salvatore Aricò, Vincenzo Baglio, Maria Assunta Navarra

XLVII Congresso Nazionale di Chimica Fisica, Roma, 1-7 Luglio 2019

“Perovskite Titanate as Electrode Additive for Direct Methanol Fuel Cells” (DMFCs) (Poster)

Lucia Mazzapioda, Maria Assunta Navarra, Stefania Panero

Ionic Liquids for Electrochemical Devices (ILED 2018), Roma, 9-11 Settembre 2018

“Different approaches to the realization of new gel polymer electrolytes containing an ionic liquid”, (Poster)

Lucia Lombardo, Ruggero Poiana, Lucia Mazzapioda, Maria Assunta Navarra, Stefania Panero

69th Annual Meeting of the International Society of Electrochemistry (ISE 2018), Bologna, 1-7 Settembre 2018.

“Bifunctional Perovskite Titanate as Electrode and Electrolyte Component for Fuel Cells and Electrolyzers”, (Poster)

Lucia Mazzapioda, Maria Assunta Navarra, Stefania Panero

Energy Conversion, Management, Recovery, Saving, Storage and Renewable System (AIGE/IIETA 2018), Reggio Calabria, 13-16 Giugno 2018.

“Titanium-based Oxide Nanoparticles as Electrode and Electrolyte Components in PEM Fuel Cells and Electrolyzers”, (Poster)

Lucia Mazzapioda, Maria Assunta Navarra, Stefania Panero

Giornate dell'elettrochimica italiana (GEI 2018), Sestriere, Torino, 21-25 Gennaio 2018, “Titanium-Based Oxide Nanoparticles as Electrode and Electrolyte components in PEM Fuel Cells and Electrolyzers”, (Poster)

Lucia Mazzapioda, Maria Assunta Navarra, Stefania Panero

Workshop: Materials for Energy Applications through Neutron and X-ray. Eyes. Goteborg, 22-23 Maggio 2017.

“Titanium-Based Metal Oxide Nanoparticles as Electrode and Electrolyte components in PEM Fuel Cells and Electrolyzers”, (Poster)

Lucia Mazzapioda, Maria Assunta Navarra, Stefania Panero